

**EVALUATION OF CORROSIVE ENVIRONMENT IMPACT ON
LOW COST Fe/Al ADDED SAC105 SOLDER ALLOYS**

NOR ILYANA BINTI MUHD NORDIN

**FACULTY OF ENGINEERING
UNIVERSITY OF MALAYA
KUALA LUMPUR**

2017

EVALUATION OF CORROSIVE ENVIRONMENT IMPACT
ON LOW COST Fe/Al ADDED SAC105 SOLDER ALLOYS

NOR ILYANA BINTI MUHD NORDIN

THESIS SUBMITTED IN FULFILMENT OF THE
REQUIREMENTS FOR THE DEGREE OF DOCTOR OF
PHILOSOPHY

FACULTY OF ENGINEERING
UNIVERSITY OF MALAYA
KUALA LUMPUR

2017

**UNIVERSITI MALAYA
ORIGINAL LITERARY WORK DECLARATION**

Name of Candidate: NOR ILYANA MUHD NORDIN

Registration/Matric No: KHA130078

Name of Degree: DOCTOR OF PHILOSOPHY

Title of Project Paper/Research Report/Dissertation/Thesis ("this Work"):
EVALUATION OF CORROSIVE ENVIRONMENT IMPACT ON LOW COST
FE/AL ADDED SAC105 SOLDER ALLOYS

Field of Study: MATERIALS ENGINEERING

I do solemnly and sincerely declare that:

- (1) I am the sole author / write of this Work;
- (2) This Work is original;
- (3) Any use of any work in which copyright exist was done by way of fair dealing and for permitted purposes and any excerpt or extract from, or reference to or reproduction of any copyright work has been disclosed expressly and sufficiently and the title of the Work and its authorship have been acknowledged in this Work;
- (4) I do not have any actual knowledge nor do I ought reasonably to know that the making of this work constitutes an infringement of any copyright work;
- (5) I hereby assign all and every rights in the copyright to this Work to the University of Malaya ("UM"), who henceforth shall be owner of all the copyright in this Work and that any reproduction or use in any form or by any means whatsoever is prohibited without the written consent of UM having been first had and obtained;
- (6) I am fully aware that if in the course of making this Work I have infringed any copyright whether intentionally or otherwise, I may be subject to legal action or any other action as may be determined by UM.

Candidate's Signature

Date

Subscribed and solemnly declared before,

Witness's signature

Date

Name: Ir.Dr. Suhana Mohd. Said

Designation: Assoc.Prof.

ABSTRACT

The current trend for multi-functioning miniaturised devices has driven research and development of higher density electronics. This has a significant impact on electronics packaging, especially in solder joints with reduction in solder contact area. This current trend has placed a challenge in ensuring the reliability of the soldered joint. Concerns on solder joint reliability in terms of its mechanical, electrical, and corrosion behaviour is critical to the operation of the overall electronic device. This work studies the lead-free solder formulation, Fe/Al added Sn-1.0Ag-0.5Cu (SAC105) solder alloy, in terms of solder joint integrity exposed to the corrosive environment. Test specimens of printed circuit board (PCB) solder board mounted with solder balls of the mentioned formulations were fabricated. Simulation of corrosive environment using salt mist. A solder ball shear test was performed to observe joint strength (solder/substrate interface). Potentiodynamic polarization was conducted to provide an electrochemical understanding of the corrosion mechanism for these solder alloys in a salt solution. With addition of Al, material experience better passivation that increase the corrosion resistance. The corrosion resistance of Al-added was found better than SAC105, whilst the Fe added solder was comparable to SAC105. It is interesting to note that for Fe-added SAC 105, formation of passivation layer provides resistance towards aqueous environment, which is beneficial as Fe was initially thought to be susceptible to corrosion. Microstructural study and element mapping were carried out to complement the analysis of the potentiodynamic and shear stress studies, especially in correlating the role of intermetallic compounds (IMCs) to mechanical performance. The minor alloying addition of Fe or Al in SAC105 solder formed intermetallic compounds (IMC) FeSn_2 for Fe-addition, and Al-Cu and Al-Ag for Al addition. The presence of these IMCs have significant impact on mechanical properties after exposure to an aqueous environment. These IMCs, although chemically inert, impose a potential difference between the

elements within the alloy and encourage dissolution which results in modification of the mechanical and surface properties. The ball shear test performed has indicated that the addition of Fe/Al to the SAC105 alloy results in preservation of the joint strength despite excessive exposure to the corrosive environment. Specimens containing solder balls of Fe/Al added SAC105 have shown to perform similar to SAC105. The addition of Al has altered the material surface with a more densely-packed corrosion product which hinders the creation of crevices on the surface that may encourage further corrosion. On the other hand, for the case of Fe-added SAC solder, the presence of FeSn_2 IMC through Fe addition created a more noble microstructure within the SAC105 alloy. Finite element analysis (FEA) simulates the impact of solder ball size on the shear strength of the solder/substrate joint. Conclusively, the evaluation of solder joints of Fe or Al added SAC 105 have shown good mechanical improvement and enhanced corrosion resistance over SAC 105. This demonstrates an improvement of the SAC105 solder formulation by using cost-effective and commonly available additions such as Fe and Al.

ABSTRAK

Teknik terkini peranti pelbagai fungsi yang bersaiz kecil yang telah memacu penyelidikan dan pembangunan di dalam elektronik berkepadatan tinggi. Ini memberi kesan yang signifikan terhadap pembungkusan elektronik, khasnya pada kekuatan pateri di mana kawasan pematerian dikurangkan secara drastik. Ini memberi suatu cabaran pada kebolehtahanan pateri disebabkan oleh pengurangan yang drastik pada kawasan sentuhan pematerian. Ketahanan pateri adalah penting di mana kebolehpercayaan sendi-sendi dalam aspek mekanikal, elektrikal, dan kelakuan kakisan adalah kritikal terhadap operasi keseluruhan peranti elektronik. Kajian mengenai formulasi pematerian bebas plumbum, dengan penambahan Fe/Al ke dalam aloi Sn-1.0Ag-0.5Cu (SAC105), dari sudut integriti kekuatan pateri. Spesimen ujian daripada papan litar bercetak (PCB) yang dipasangkan dengan bebola pateri dengan formulasi seperti yang telah dibincangkan telah difabrikasikan. Simulasi persekitaran menghakis dengan kebuk dalam wap garam. Ujian ricih bebola pateri dilakukan / dijalankan untuk mencari kekuatan ricih sendi pateri (pateri /antara-muka substrat) selepas terdedah pada kakisan. Ujian polarisasi potentiodynamik telah dijalankan untuk memberi kefahaman elektrokimia bagi mekanisma kakisan menggunakan aloi pateri SAC105 dengan penambahan Fe/Al dalam larutan garam. Dengan penambahan Al, daya pasif bahan pateri adalah lebih baik dan menjadi tegar kakisan. Rintangan kakisan dengan penambahan Al didapati lebih baik daripada SAC105, manakala bagi penambahan Fe pada SAC105 memaparkan prestasi setanding dengan bahan asal iaitu SAC105. Sesuatu yang menarik boleh dilihat pada kes di mana bahan SAC 105 dengan tambahan Fe di mana lapisan pasif di permukaan selepas terdedah kepada larutan garam masih terbentuk. Ini menunjukkan formulasi ini menyediakan rintangan terhadap persekitaran berair, walau pada dasarnya Fe adalah sangat mudah terdedah kepada kakisan. Kajian mikrostruktur dan pemetaan elemen telah dijalankan untuk melengkapkan analisis

kajian potentiodynamik dan tegasan ricih, khasnya dalam menghubungkan peranan sebatian intermetalik (IMCs) terhadap prestasi mekanikal. Penambahan pengaloiian kecil Fe atau Al kepada struktur ternari SAC105 menghasilkan pembentukan sebatian intermetalik (IMC) FeSn_2 bagi penambahan Fe dan Al-Cu dan Al-Ag bagi penambahan Al. Kehadiran IMCs ini telah terbukti mempunyai kesan yang besar ke atas sifat-sifat mekanikal selepas terdedah kepada persekitaran yang berair. Sebatian antara muka ini, walaupun lengai secara kimia, mengenakan beza keupayaan antara unsur-unsur dalam aloi dan menggalakkan pelarutan atau penguraian yang menyebabkan pengubahsuaian sifat-sifat permukaan mekanikal dan bahan. Ujian bola ricih yang dilakukan telah menunjukkan bahawa penambahan Fe/Al ke dalam SAC105 masih mampu mempertahankan kekuatan sendi pateri walaupun pendedahan berlebihan kepada persekitaran yang menghakis. Spesimen bahan SAC105 dengan penambahan elemen Fe/Al menunjukkan prestasi hampir serupa dengan SAC105 tetapi menunjukkan kekuatan ricih yang lebih rendah sedikit daripada bahan SAC305. Penambahan Al telah mengubah permukaan bahan dengan produk kakisan yang lebih padat yang menghalang penciptaan rekahan di permukaan yang boleh menggalakkan kakisan selanjutnya. Sebaliknya, bagi penambahan Fe, kehadiran FeSn_2 mencipta mikrostruktur yang lebih canggi dalam aloi SAC105 itu. Data ujikaji pada tegasan ricih dilengkapi dengan analisis elemen terhingga, yang melibatkan simulasi terhadap kesan saiz pateri bebola pada kekuatan ricih dengan substrat. Kesimpulannya, penilaian sendi pateri bagi bahan SAC105 yang ditambah dengan Fe/Al telah menunjukkan peningkatan mekanikal yang baik dan mempunyai peningkatan rintangan kakisan daripada SAC105 tulen. Ini membuktikan penambahbaikan bagi pateri yang ditambah Fe dan Al.

ACKNOWLEDGEMENTS

First and foremost, my gratitude goes to my institution, University of Malaya, for providing the facilities and support which have led to the completion of the research project. It is worth mentioning that this project is supported by Postgraduate Research Fund (PPP Grant, Project number PG140-2014A) and UM Research Grant (UMRG RP003D-13AET).

I sincerely thank my supervisors, Associate Professor Dr Suhana Binti Mohd Said from Electrical Engineering Department, University of Malaya, Associate Professor Dr Rahizar bin Ramli from Mechanical Engineering Department, University of Malaya and Dr Kirsten Weide-Zaage from University of Hannover for their guidance and supervision throughout my PhD candidature. I extend thanks to Associate Professor Dr Mohd Faizul bin Mohd Sabri from Mechanical Engineering Department, University of Malaya, Associate Professor Dr Nurulakmal Shariff from School of Materials and Mineral Resources, University Science Malaysia, Dr Aizuddin from Mechanical Engineering Department, University of Malaya, Dr Azizah binti Mainal from Chemistry Department, University of Malaya and Mr Wan Mohd Fadzil from Reliability Lab MIMOS for their valuable input, time spent and also facilities provided to ensure the smoothness and success of this research.

In addition, I would like to further extend my gratitude to my fellow researchers from both Mechanical Engineering and Electrical Engineering Department, University Malaya. I deeply appreciate the advice given and other various help especially in the experimental work related to the project.

Finally, I thank my family members for their endless support and tolerance during the period of my study, especially during difficult times.

TABLE OF CONTENTS

ORIGINAL LITERARY WORK DECLARATION	ii
ABSTRACT	iii
ABSTRAK	v
ACKNOWLEDGEMENTS	vii
TABLE OF CONTENTS	viii
LIST OF TABLES	xii
LIST OF FIGURES	xiv
LIST OF SYMBOLS AND ABBREVIATIONS	xix
CHAPTER 1 : INTRODUCTION	1
1.1 Background	1
1.2 Problem Statement	4
1.3 Objectives of the Study	5
1.4 Thesis Outline	6
CHAPTER 2 : LITERATURE REVIEW	8
2.1 Current status of solder alloy development	8
2.2 Solder joint formation	11
2.2.1 Intermetallic compound (IMC) formation	11
2.2.2 Solder joint strength of Sn-based solder joints	13
2.3 Effect of fourth element addition on SAC105 solder in terms of IMC layer, surface fracture and mechanical impact	19
2.3.1 Effects of addition of Ni and Ge	20
2.3.2 Effects of addition of Al, B and SiC	23
2.3.3 Effects of addition of Mn and Ti	26
2.3.4 Effects of addition of Fe and Bi	27
2.4 Electronics products assembly and packaging process	30

2.5	The impact of dissimilar metals of Sn-based solder alloy in humidity	31
2.5.1	Potential risk assessments of material exposed in humid environment	32
2.5.2	Potentiodynamic polarization analysis of Sn-based solder alloys in sodium chloride: basic principles	32
2.5.3	Sn-based solders under Salt Spray Test	37
2.6	Numerical modelling of solder joint failure	40
2.6.1	Types of solder joint fatigue models	41
2.6.1.1	Plastic Strain Approach	41
2.6.1.2	Creep Strain Approach	42
2.6.1.3	Energy-based Approach	42
2.6.2	Viscoplastic constitutive model	43
2.7	Summary	47
CHAPTER 3 : METHODOLOGY		49
3.1	Material preparation	51
3.1.1	Solder/substrate assembly and salt spray test	52
3.1.2	Test cells for potentiodynamic polarization test	54
3.2	Assessments and characterization	55
3.2.1	Solder ball shear test	55
3.2.2	Potentiodynamic Polarization Analysis	56
3.2.3	Salt Spray Test	58
3.2.4	Microstructural, elemental and structural characterization of solders	59
3.3	Simulation	60
3.3.1	Element type	61
3.3.2	Material type and meshing	62
3.3.3	Load and boundary condition	64
3.3.4	Solver	65

3.3.5	Post processor	65
CHAPTER 4 : SOLDER BALL FABRICATION AND BALL SHEAR		
BENCHMARK TEST		67
4.1	Solder ball fabrication	67
4.1.1	The Apparatus	68
4.2	Ball shear benchmark test	72
4.2.1	Shear strength of Ni-doped SAC305	72
CHAPTER 5 : RESULTS AND DISCUSSION		74
5.1	Sn-1Ag-0.5Cu	75
5.1.1	Surface morphology and microstructure	75
5.1.1.1	Surface morphology after Salt Spray test	76
5.1.1.2	Interfacial reaction as reflow	81
5.1.1.3	Interfacial reaction after aging	83
5.1.2	Corrosion behaviour through potentiodynamic polarization	84
5.1.3	Shear Strength of Solder Joint	88
5.2	Sn-1Ag-0.5Cu solder alloy bearing 0.1 wt. %, 0.3 wt. % or 0.5 wt. % Fe	89
5.2.1	Surface morphology and microstructures	90
5.2.1.1	Interfacial reaction as reflow	92
5.2.1.2	Interfacial reaction after ageing	94
5.2.2	Material corrosion behaviour in potentiodynamic polarization	95
5.2.3	Shear Strength of Solder Ball/Cu Joint Interface	104
5.2.4	Fracture behaviour	106
5.3	Sn-1Ag-0.5Cu solder alloy bearing 0.2 wt. %, 0.5 wt. % or 1.0 wt. % Al	109
5.3.1	Surface morphology and microstructural properties	109

5.3.1.1	Interfacial reaction as reflow	113
5.3.1.2	Interfacial reaction after aging	116
5.3.2	Materials corrosion behaviour in potentiodynamic polarization	120
5.3.3	Shear Strength of Solder Ball/Cu Joint Interface	125
5.3.4	Fracture behaviour	128
5.4	Finite element analysis	130
5.4.1	Model validation	130
5.4.2	Size impact of solder joint strength	131
5.5	Summary	137
CHAPTER 6 : CONCLUSION		139
6.1	Conclusion	139
6.2	Limitation and Recommendations for future work	144
REFERENCES		147
LIST OF PUBLICATIONS AND BOOK CHAPTER		156

LIST OF TABLES

Table 2.1 Tabulation of findings for investigation of solder strength of a variety of SAC105 lead-free solder alloys with fourth element additions.	18
Table 2.2: (a) Corrosion properties in 3.5 wt% NaCl solution for Sn, Cu and the intermetallics (b) Corrosion products and its morphology (Tsao & Chen, 2012)	34
Table 2.3: Corrosion potential and current density for S-1 and S-2 solders (Wierzbicka-Miernik, Guspiel, & Zabdyr, 2015)	36
Table 2.4: The summary of some setting for the potentiodynamic polarization.....	37
Table 2.5 Corrosion products associated with to Sn-based solder alloy in NaCl solution.....	39
Table 3.1 Chemical composition of solder materials	51
Table 3.2 List of material weight and corresponding density for each composition used in the test	57
Table 3.3 Material Properties	63
Table 4.1 Approximation of solder balls produced in the experiment.....	71
Table 5.1 EDX analysis of solder ball surface after salt spray test	79
Table 5.2: Galvanic series of commercial metals in seawater.....	79

Table 5.3 Intermetallic thickness at solder/substrate joint for as-reflow a) SAC105 b)SAC105-0.1Fe c) SAC105-0.3Fe and d) SAC105- 0.5Fe	94
Table 5.4 Corrosion properties of SAC105 and SAC105-xFe	96
Table 5.5 Intermetallic thickness at solder/substrate joint for as-reflow a)SAC105 b)SAC105-0.2Al c) SAC105-0.5Al and d) SAC105- 1.0Al	114
Table 5.6: Results for corrosion potential, current density and corrosion rate.....	122
Table 5.7: Surface area, reaction force and Shear Strength of 1mm, 760µm and 450µm solder SAC105/Cu solder joint	133
Table 6.1 Corrosion potential and current with the corrosion rates of SAC solder alloy	140
Table 6.2: Solder ball joint strength for SAC solder alloy	143

LIST OF FIGURES

Figure 1.1 Solder joint technology levels	1
Figure 2.1: Effect of Ag content in SAC solder alloys	10
Figure 2.2 Cu-Sn binary phase diagram.....	13
Figure 2.3: Impact shear test methods. (a) Pendulum tester (Date, Shoji, Fujiyoshi, Sato, & Tu, 2004) (b) Miniature Charpy impact tester (Shengquan, Yuhuan, Tu, Alam, & Chan, 2005) (c) Ball Impact Tester (Chang-Lin, Yi-Shao, Hsiao-Chuan, & Tsan-Hsien, 2005).....	16
Figure 2.4: SAC105-Ni/Ge/Cu substrate interfacial reaction (Lai et al., 2007).....	20
Figure 2.5: SEM of Sn _{94.78} Ag _{4.0} Cu _{0.58} Al _{0.6} Ni _{0.04} (5000X) (Benlih et al. 2007).....	21
Figure 2.6: Graph of shear force as a function of shear speed for different pad finishes. (a) rosin flux. (Kumar et al., 2013)	22
Figure 2.7: SEM images of the different fracture modes on Cu-OSP substrate (DT: ductile mode. MX: mix mode). (Kumar et al., 2013).....	22
Figure 2.8: EPMA analysis on the distribution and composition of boron in the Cu ₆ Sn ₅ and Cu ₃ Sn IMC interface layers of the solder joint doped with 0.1 wt.% B (a) before and (b) after aging at 150°C for 100 h. (Choi et al., 2012)	24
Figure 2.9; Changes in the IMC thickness and fracture force under the high-speed ball pull test at 400 mm/s after aging at 150°C for various aging times (hr). (Choi et al., 2012)	25

Figure 2.10: SEM fractrograph for (a) SAC105 and (b) SAC105–0.75SiC solders.(El-Daly, Fawzy, Mansour, & Younis, 2013).....	26
Figure 2.11: Nanoindentation results of the intermetallic phases. (Lin et al., 2009).....	27
Figure 2.12: SEM images of fracture surface of SAC105, SAC105–Fe–1Bi, SAC105–Fe–2Bi. (Mahdavifard et al., 2015)	28
Figure 2.13 Microstructure of SAC105 and SAC105-xFe (Shnawah, Said, Sabri, Badruddin, & Che, 2012).....	29
Figure 2.14: Electrochemical Potentiodynamic curve for lead-free solder (Wu, Chan, & Alam, 2006)	33
Figure 2.15: Corrosion products of the surface of (a) Sn (b) Cu (c) Cu ₃ Sn (d) Cu ₆ Sn ₅ (Tsao & Chen, 2012).....	35
Figure 2.16: SAC405 after 96hr in salt spray test (Fubin & Lee, 2006).....	38
Figure 2.17: Solder/cu 2-dimensional model in ANSYS (Kim and Jung (2006)	45
Figure 2.18: A half symmetric FE model of BGA solder joint (Qin et al., 2015).....	46
Figure 3.1 Overall flow chart of the material preparation, experimental procedures and post-processing of results.....	50
Figure 3.2 Forms of solder alloys used throughout the study	52
Figure 3.3 Solder ball fabrication using a metal syringe.....	53

Figure 3.4 Test boards for salt spray test	54
Figure 3.5 Sample preparation for potentiodynamic polarization.....	55
Figure 3.6 Solder ball shear test setup.....	56
Figure 3.7 Schematic diagram of the cell used in the potentiodynamic polarization.....	57
Figure 3.8 Standard of procedure in mixing the 5% NaCl saline solution.....	58
Figure 3.9 The salt spray test chamber in Reliability Laboratory, MIMOS.	59
Figure 3.10 Process flow of problem solving by finite element simulation	61
Figure 3.11: 20-nodes SOLID186 Structural Solid Geometry.....	62
Figure 3.12 Meshing for continuous element divisions of solder ball, copper pad and FR4 board.	64
Figure 3.13: Shear load on the solder ball surface	64
Figure 3.14 Stress vs. Total Strain for Multilinear Isotropic Hardening.....	65
Figure 4.1: (a) Solder ball droplet method using a heated metal syringe (b) The fabricated droplets.....	69
Figure 4.2: (a) Metal syringe after optimization of the design (b) Multi- dimensional solder balls.	70
Figure 4.3: Comparison of shear strength of a 450 μm solder ball on Cu/OSP using a DAGE DT 4000 tester or an Instron Universal tester.....	73
Figure 5.1 Surface microstructure of as-reflow SAC105.....	76

Figure 5.2: FESEM micrographs of (a) as-reflow SAC105 solder alloy and after salt spray b) for 24 hr (b) for 96 hr (c) for 96 hr with 24 hr of ageing at 180 °C.....	77
Figure 5.3: Corrosion mechanism caused by Cl^- and the formation of corrosion products on the material's surface.....	78
Figure 5.4: EDX analysis of SAC105 solder alloy after salt spray test	80
Figure 5.5: FESEM micrographs of SAC105 (a) as reflow (b) 96hour aged, 180°C.....	81
Figure 5.6: Potentiodynamic curve for SAC105	85
Figure 5.7: (a) Stress-strain curve (b) shear strength of SAC105 solder ball interconnect, before and after salt spray test and after ageing	88
Figure 5.8: FESEM micrographs of SAC105 and Fe-added SAC105 solder balls after salt spray test and 24 hr of ageing at 180 °C	90
Figure 5.9: Phase diagram of (a) Sn-Ag-Cu (b) Fe-Sn (ASM International).....	91
Figure 5.10: Cross sectional FESEM micrographs (a-d) SAC105-0.1Fe (e-h) SAC105-0.3Fe (i-l) SAC105-0.5Fe after 1x reflow, 96-hour salt spray test and ageing, respectively.	93
Figure 5.12: Variation of IMC thickness with Fe addition after ageing at 180 °C for 24 h.	95
Figure 5.13: Potentiodynamic Curve for SAC105 and Fe-added SAC105.....	97
Figure 5.14: Surface morphology of polarized a) SAC105-0.1Fe b) SAC105-0.3Fe and c) SAC105-0.5Fe at 10 μm magnification	98

Figure 5.15: Material integration from the impact of dissimilar adjacent elements.....	101
Figure 5.16: Solder joint of a) SAC105 b) SAC105-0.1Fe c) SAC105-0.3Fe and d) SAC105-0.5Fe after a 96-hour salt spray test	104
Figure 5.17: Shear strength of SAC105-xFe solder ball interconnect before and after salt spray test and after ageing	105
Figure 5.18: FESEM fractographs of the solder alloys after solder ball shear tests (a) SAC105-0.1Fe (b) SAC105-0.3Fe (c) SAC105-0.5Fe at 10 μ m magnification	108
Figure 5.19: FESEM micrographs of a)SAC105, b) SAC105-0.2Al c) SAC105-0.5Al d) SAC105-1Al solder balls as-reflow and after salt spray testing for 24 h, 96 h or 96 h + ageing in 180 °C.....	110
Figure 5.20: Phase diagram of (a) Al-Cu-Sn (b) Sn-Ag-Cu (ASM International)	112
Figure 5.21: OM images of SAC105 and Al-added SAC105 solder alloys.....	113
Figure 5.22: Cross sectional FESEM micrographs Al-added SAC105 (a-c) as-reflow 96hour salt spray test and 24 hour ageing at 180°C (g) element map for SAC105-Al solder alloy	117
Figure 5.23: Variation of IMC thickness with Al addition after aging at 180°C for 24 h.	118
Figure 5.24: Corrosion behaviour of Al-added SAC105	121

Figure 5.25: FESEM micrograph (10 μm magnification), XRD and EDX analysis of the corrosion behaviour of Al-added SAC105.....	125
Figure 5.26: Shear strength of SAC105-xAl solder ball interconnect before and after salt spray testing and after ageing	126
Figure 5.27: Shear fracture of h of SAC105-xAl solder ball interconnect, a) before and b) after salt spray	129
Figure 5.28: Correlation of the Model Predictions with Experimental Stress-Strain Curves for SAC105.....	131
Figure 5.29 Contour plot of an average equivalent stress analysis and the cross-sectional view	133
Figure 5.30: Equivalent stress distribution for different solder ball sizes of SAC105 with solder ball diameter of (a)1.2mm (b)760um (c)450um	135
Figure 5.31: Interfacial layer initiation mechanism in soldering	136

LIST OF SYMBOLS AND ABBREVIATIONS

σ	engineering stress
ϵ	engineering strain
wt. %	Weight percent
E	Young's modulus
E_{corr}	corrosion potential
i_{cc}	critical current density
I_{corr}	corrosion current
AES	atomic emission spectrometry
ASTM	American Society for Testing and Materials
BGA	Ball Grid Array
CTE	Coefficient of Thermal Expansion
EDX	Energy dispersive x-ray spectroscopy
FEA	finite element analysis
ICDD	International Committee of Diffraction Data
IMC	Intermetallic Compound
IMCs	Intermetallic Compounds
OPM	Optical Polarized Microscope
RoHS	Restriction of Hazardous Substances
OSP	Organic solderable preservative (surface finish)
ENIG	Electroless nickel immersion gold (surface finish)
PBGA	Plastic ball grid array
SiC	Silicone carbide
SEM	scanning electron microscopy
CR	corrosion rate
DOF	degree of freedom
JEDEC	Joint Electron Device Engineering Council

IEC	International Electrotechnical Commission
IPC	Association Connecting Electronic Industries
LME	London metal exchange
MSL	moisture sensitivity level
TH	temperature-humidity
UTS	ultimate tensile strength
RH	relative humidity
SAC	Sn-Ag-Cu (tin-silver-copper)
SAC105	Sn-1wt. % Ag-0.5wt.% Cu
SAC205	Sn-2wt. % Ag-0.5wt.% Cu
SAC305	Sn-3wt. % Ag-0.5wt.% Cu
SAC405	Sn-4wt. % Ag-0.5wt.% Cu
SAC105-0.05B	Sn-1wt. % Ag-0.5wt.% Cu- 0.05wt.% B
SAC105-0.1Fe	Sn-1wt. % Ag-0.5wt.% Cu- 0.1wt.% Fe
SAC105-0.3Fe	Sn-1wt. % Ag-0.5wt.% Cu- 0.3wt.% Fe
SAC105-0.5Fe	Sn-1wt. % Ag-0.5wt.% Cu- 0.5wt.% Fe
SAC105-0.2Al	Sn-1wt. % Ag-0.5wt.% Cu- 0.2wt.% Al
SAC105-0.5Al	Sn-1wt. % Ag-0.5wt.% Cu- 0.5wt.% Al
SAC105-1.0Al	Sn-1wt. % Ag-0.5wt.% Cu- 1.0wt.% Al
SIMS	Secondary Ion Mass Spectrometry
SJR	solder joint reliability
SCE	standard calomel electrode
XPS	X-ray photoelectron spectroscopy
XRD	x-ray diffractometer

CHAPTER 1 : INTRODUCTION

1.1 Background

Soldering is a metallurgical bond metal joining method that is conducted by melting a filler metal in between the terminals to join at temperatures below 450 °C. The technology for soldering is essential for the electronics industry, specifically in level 1 (packaging of the integrated circuits) and level 2 (assembly of components on printed circuit boards) (Frear, 2001), as shown in Figure 1.1. Solders are the adhesive that are used to provide not only electrical connectivity but also mechanical strength to hold the joint and provide heat dissipation in electronic assemblies.

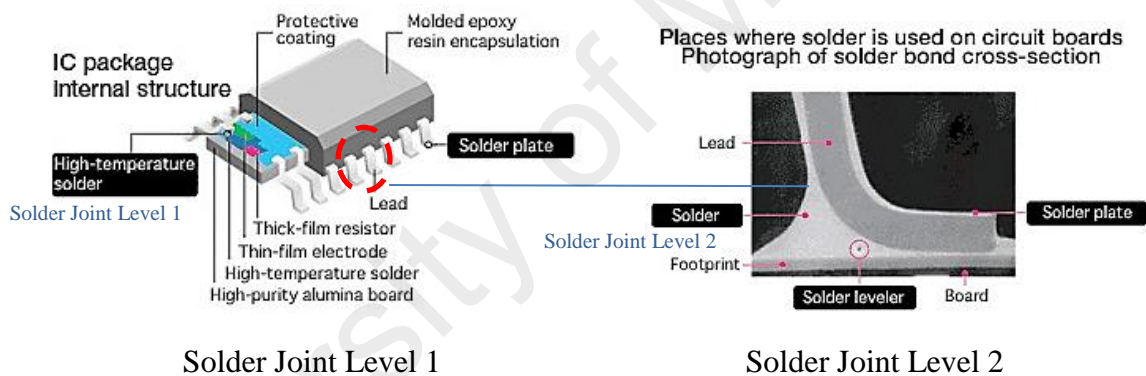


Figure 1.1 Solder joint technology levels

Initially, the most consumed solders are tin/lead alloys, particularly eutectic (Sn/37Pb) and near-eutectic (Sn/40Pb) compositions. Soldering technology that involves leaded (Sn/Pb) alloys has been developed and improved over the years. This material is cheap and possess a few other advantages such as high ductility and wettability, easy to handle and melt at low temperatures (Abtew & Selvaduray, 2000).

Over the years, consistent demand for electronics appliances has led to continuous supply of products from the global electronics industry. Consequently, because of its hi

utilization in all devices, soldering technology remain the essential in interconnection of the electronic packaging. The established reliability of soldering is due to the optimization done on the processing, equipment setup and conditions for Sn/Pb solders (Suganuma, 2001).

However, Pb has been found to have a very high level of toxicity that this issue had raised concerns as its presence in the environment. This prompted legislative efforts to prohibit the use of lead containing solders in applications. The United States started the banning of all solders containing Pb in 1990. Following this, bans were also instituted in Europe, Japan and other Asian countries. These developments led to Sn/Pb material replacement researches (Abtey & Selvaduray, 2000; Frear, 2001; Suganuma, 2001) .

Handheld and portable electronics products are not only becoming smaller but also cheaper and lighter. This shows a trend towards customization in terms of the design and the appearance (Karppinen, Li, Pakarinen, Mattila, & Paulasto-Kröckel, 2012; Mattila & Kivilahti, 2006; Sumikawa, Sato, Yoshioka, & Nukii, 2001). This transition is achieved through the increase of complexity in the circuitry, the integrated functions and the overall miniaturization of the electronic devices. The inclination of functional complexity of the devices introduces reliability concerns (Wang et. al., 2014).

Sn–Ag–Cu (SAC) alloys with high-Ag-content are considered promising replacements for Sn–Pb solder alloy. Among the popular compositions are the SAC405 and SAC305. These alloys is near-eutectic compositions and has good thermal and mechanical fatigue properties (Chong et al., 2006; Terashima, Kariya, Hosoi, & Tanaka, 2003). However, the high Ag SAC alloys are more rigid as compared to the Sn/Pb solder alloys. Thus, higher failure incidents due to drop and handling in portable products (Chong et al., 2006; B. Zhang, Ding, & Sheng, 2009). Moreover, the high-Ag SAC alloys causes the cost of these solder alloys to be expensive and the challenge for the global market for Ag to sustain on

supplying Ag for the solder industry (A. M. Yu, Jae-Won, Jun-Ki, Jong-Hyun, & Mok-Soon, 2010).

Low-Ag-content SAC alloys, SAC105 is considered as a solution to both of these concerns. By lack of Ag contained in the solder alloy, the elasticity and dissipation of plastic energy increase. Both are among the key factors that reduce the damage from drop impact (Dongwook et al., 2007; Suh et al., 2007). However, this improvement seen from drop is accompanied by the degradation in the thermal and mechanical fatigue properties and ageing resistance. Accordingly, studies have been initiated to investigate the minor element alloying of SAC105 alloys.

By optimizing the low-Ag content SAC alloys with the addition of a fourth alloying element, it is possible to refine the microstructure and improve the mechanical strength. Accordingly, these alloys have created a stronger interest in investigation of their additional potential applications (G.-y. Li & Shi, 2006; D. Q. Yu, Zhao, & Wang, 2004; Q. K. Zhang, Long, Yu, Pei, & Qiao, 2015).

However, the addition of the fourth element in ternary solders system increase the type of different IMCs within the solder matrix. This eventually alters the mechanical and electrical properties and also introduces different electron potential stresses between the elements. On the electron potential concerns, soldering of electronics packaging and assembly expose the PCB boards towards various liquids and vapors. This scenario created a spontaneous natural reaction which is commonly addressed as corrosion. Corrosion depends on the existence of oxygen, metals and a medium. The internal humidity build-up on corrosion reliability due to the significant change of internal water vapor concentration with temperature cycling in small spaced enclosure. This eventually promoted leakage current (Conseil et. al., 2016). The corrosion potential is also related to the types of fluxes used in different type of surface finishes where fluxes are proven for its propensity to cause

creep corrosion. Creep corrosion could occur at either low or high relative humidity. For OSP (organic surface preservative) and ImAg (immersion silver) finished PCBs, the creep corrosion occurred only in the low relative humidity range; whereas, in ENIG (gold on electroless nickel) finished PCBs, it could occur both in low and high relative humidity environments. (Singh et. al., 2017). Among recent studies evolved around stability of SAC solders in corrosive solution and the roles of Ag_3Sn and other IMCs within the solder matrix. The addition of fourth elements such as Ni, Fe, Bi and Al altered the formation of Ag_3Sn and hence modified the overall performance of the solder alloy. Nevertheless, importance was also highlighted on the protective corrosion products layers on top of the material that hindered the corrosion process. (Alvarez et. al. , 2014); Nordin et. al. , 2014; Mohanty et. al., 2013; Wisley Riuper et. al., 2012; Wierzbicka-Miernik et. al., 2015)

1.2 Problem Statement

It has been 10 years since the start of the transition to lead-free solder. The ternary solder system has since established as the most popular formulation with SAC305 as the dominant choice. In the effort to reduce production costs, the high content of Ag in SAC305 has rendered it as a less favorable option. This scenario drove research efforts to reducing Ag content. However, lead-free solders with less Ag possessed inferior quality. A common approach to improve the quality of lower Ag content SAC solders is by a fourth element addition. A modification in mechanical and electrical properties is anticipated by increasing the element content in a solder matrix. The nature of soldering process involved various vapors and liquids. This environment provokes the metals within the PCB space to respond through a corrosion mechanism to reach their stable state. The material of solder alloy alone was produced by dissimilar metals casted in a single form. With fluctuation of heat and entrapment of moisture, reliability of joint and leaded frames of IC chips is open to be questioned. Failure at the solder ball-substrate interface is critical to the overall

performance of the PCB (Printed Circuit Board). This research will assess the reliability of SAC105 lead-free solder with minor alloying of Fe or Al. The assessments are performed in terms of the impact on interfacial reaction between the solder and Cu pad, the shear fracture mode, the mechanical joint strength, the corrosion resistance and the impact of reducing the solder ball diameter used in soldering.

1.3 Objectives of the Study

The SAC105 with minor addition of Fe/Al has good mechanical strength, aged resistant and high electrical resistivity. However, it is yet an unknown knowledge if the material is robust in long term. This is because, the material consist of very aggressive and highly reactive metals, namely the Al and Fe. The major aim of this research is to utilize the accelerated assessment to extract the long term intrinsic performance of the material, within a corrosive environment. The work will assess the joint strength in the impact of altered interfacial layer in a function of environment and Fe/Al content.

The objectives of this work are as follows:

- i. To assess the solder/substrate joint strength of the SAC105-Fe/Al solder alloy;
- ii. To determine the corrosion behaviour of the SAC105 with minor addition of Fe/Al;
- iii. To characterize the surface morphology and microstructure of Fe/Al-added SAC105 after a salt-spray test;
- iv. To investigate the interfacial reaction at the substrate of SAC105 with minor alloying of Fe/Al; and

- v. To simulate the impact of contact joint downsizing in electronics through numerical simulation of low Ag content lead-free solder alloys.

1.4 Thesis Outline

The thesis reports a study on the impact of a corrosive environment on the SAC105 solder alloy with minor alloying of Fe/Al in an effort to obtain more scientifically proven data on the performance of a newly proposed solder alloy composition. Specifically, this thesis is composed of 5 chapters, descriptions of which are presented here.

Chapters 1 and 2 introduce this research. Chapter 1 provides a general introduction to the use of lead-free solders in electronics assembly and the packaging industry and highlights the present limitations of several established solder alloys that are currently in use. This becomes the motivation of the research. In addition, the problem statement, the objectives and the scope of the research are identified for an overview of the study.

Chapter 2 reviews the key areas of research, for instance, the impact of fourth element addition on the mechanical and corrosion behaviour of the core solder alloy and the related assessment methods. More specifically, the research investigates the formation of the IMC layer at the substrate, the fracture mode formed, the general failure mechanism of the interconnects, the impact of dissimilar metals on Sn-based solder in humidity and the type of models used in computer simulation to predict solder joint strength. This is to provide a glance of current developments and trends in the research.

Chapters 3 and 4 describe the work carried out in the research and the pre-experiment procedures. Chapter 3 describes the details of the experimental setup, including the fabrication of the solder ball, the preparation of test boards for a salt spray test and the cold mounting of potentiodynamic polarization test cells. The chapter also describes the procedure, parameters and equipment used for each method. Four main methods are used

throughout the research. A salt spray test and a potentiodynamic polarization analysis was employed to investigate the corrosion behaviour, a solder ball shear test to assess the solder/substrate joint strength, FEA numerical analysis to predict impact of miniaturization and SEM and XRD for microstructural and cross-sectional inspection. While Chapter 4 contains the details of solder ball fabrication procedures and outcome and also the solder ball shear benchmark test. This pre-experiment process is vital in ensuring the method chosen is reliable to produce usable solder balls and can achieve the goal to measure joint strength.

Chapter 5 presents the results and discussion of the novel findings of experiments conducted on SAC105-xFe, SAC105-xAl and in simulations. The results for each element added solder alloy are compared to the core SAC105 to determine the beneficial effects of Fe or Al on the IMC layer thickness and mechanical, fracture and corrosion behaviour of the solder alloy.

Finally, Chapter 6 concludes this research by summarizing the outcomes of the work described in the previous chapters, stating its contributions and providing recommendations for future work.

CHAPTER 2 : LITERATURE REVIEW

This chapter reviews several research areas or topics that are related to this research. Based on the scope of research described in Chapter 1, three key topics can be identified, namely, the low silver ternary lead-free solder alloy material, the impact of adding a fourth element to the ternary solder alloy on its mechanical strength, and its corrosion behaviour and related mechanical assessments. These topics are relevant to various studies associated with this research. Chapter 2 is structured as follows: in Sections 2.1 and 2.2, a comprehensive review of the Sn-based lead free solder is presented, followed by an introduction, in Section 2.3, to the impact of fourth element addition in ternary solder alloy. Then, because part of the research investigates corrosion from a corrosive environment in electronics assembly and packaging, Sections 2.4 and 2.5 provide a brief review of recent studies showing the development of the process involved in industry and the impact of dissimilar metals within the bulk of Sn-based ternary solder alloys in humidity. Finally, Section 2.6 presents the general concept of the numerical method employed in most analyses of the present work related to evaluating the shear strength of the assembled solder ball on a copper substrate.

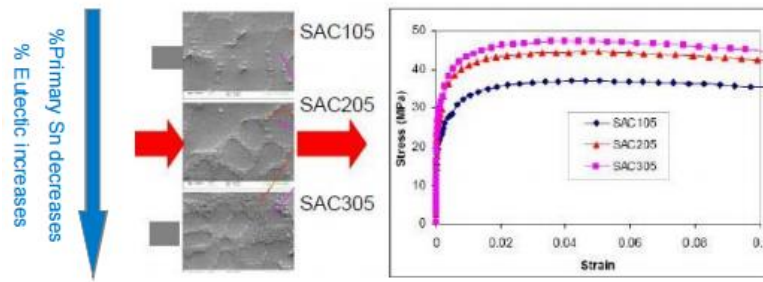
2.1 Current status of solder alloy development

Several tin base Pb-free alloys have been proposed. Microalloying with elements such as Indium (In), Bismuth (Bi), Silver (Ag), Copper (Cu), Aluminium (Al), Zinc (Zn), Gallium (Ga), Nickel (Ni) and rare-earth elements for instance Antimony (Sb) are added to the Sn-based material to produce Pb-free alloys (Abtew & Selvaduray, 2000). The ternary SAC solders is popular because of its good mechanical and wetting properties over other Sn-based lead-free solders (Anderson, Cook, Harringa, & Terpstra, 2002; Suh et al., 2007). Thus, SAC solders are highly promising Sn/Pb substitute candidates. Initially, SAC405 and

SAC305 that have near-eutectic compositions and good thermal mechanical fatigue properties are considered as a better replacements for Sn–Pb solder alloy (Chong et al., 2006; Terashima et al., 2003). However, despite these advantages, the production cost is higher because of the Ag content, and these materials were proven to fail in drop and handling of the handheld devices (Chong, 2006 ; Wong et al., 2009; B. Zhang et al., 2009). Reducing the Ag-content not only reduces cost but also increases material elasticity and dissipation of plastic energy, both of which are among the main factors to enhance performance at drop. Therefore, the shift towards lower Ag in SAC such as SAC105 was considered a solution to both of these issues.

The ternary and near-eutectic SAC105 composition, have strong development and marketing potential because of it is cost effective and has good mechanical properties (Anderson et al., 2002; Dongwook et al., 2007; Frear, 2001. Nonetheless, its comparable corrosion resistance as Sn/Pb has made it a promising soldering material to use in extreme conditions, such as marine and industrial environments (Abtew & Selvaduray, 2000). Meanwhile, there is a drive towards products miniaturization due to the continuous demand for smaller and faster electronic devices. This continuously increase the density of interconnected input/output components on electronic circuits with limited space. The low concentrations presence of corrosive agents such as chlorine, ammonia and sulphur dioxide in various working environments may increase the corrosion threat to the densely packed electrical circuit. Currently, there is increased research into addition of a fourth element in the SAC105 ternary alloy. The elements of interest include Ni (Coyle et al., 2014; Mohanty & Lin, 2013; Toh, Liu, Tu, Chen, & Yeo, 2007), Bi (Mahdavifard et al., 2015), Mn, Sb (Mukherjee, Dasgupta, Zhou, & Bieler, 2014), Fe (Shnawah, Said, Sabri, Badruddin, & Che, 2012) and Al (D.-A. Shnawah et al., 2012).

Effect of Ag on SAC Microstructure & Strength



SAC microstructure: Sn dendrites (softer) with interdendritic eutectic Sn+Ag₃Sn+Cu₆Sn₅ (harder)

Figure 2.1: Effect of Ag content in SAC solder alloys

Figure 2.1 shows the impact on microstructure of 1, 2 and 3 wt.% of Ag content in the commonly used SAC lead-free solder. Reducing the Ag content remarkably reduces the cost of mass production. Low-Ag content SAC solder was proven to have lower mechanical performance despite the fact that it is more economical. Thus the recent trends towards researching fourth element alloying to improve its performance. However, the selection of the alloying element must be within a cost-effective range. Following are the raw metal costs per kg (excluding fabrication costs) as of September 2015 (Source: London Metal Exchange (LME) website):

Sn: US\$20.23/kg

Ag: US\$556.56/kg

Cu: US\$4.7/kg

By calculating the ratio needed to produce the eutectic alloy, the raw metal cost is approximately US\$25.51/kg for SAC105 alloy and approximately US\$31.08/kg for SAC205 and US\$36.08/kg for SAC305. Roughly, if low-cost elements such as Fe or Al

were added, a reduction of approximately 0.23% to 0.74% per kg production could be achieved for the SAC105 solder alloy.

2.2 Solder joint formation

The electronic packaging industry widely utilizes Sn-based alloys as interconnection materials. Therefore, the interfacial reaction between Sn and the metallization layer is an essential process for metallurgical bond formation. The metallization typically used for solder interconnects is Cu and is readily wet by Sn when the surface is oxide-free. Intermetallic compounds (IMC) of Cu-Sn are generally formed by liquid-solid reactions and/or solid-state diffusion either during the soldering operation or during service. Excessive formation of Cu-Sn IMCs is undesirable because their brittle nature may have adverse effects on the mechanical reliability of joints. This section discusses both IMC formation and the effects of IMC on the shear strength of the solder joints.

2.2.1 Intermetallic compound (IMC) formation

When molten Sn-based solders come into contact with Cu surfaces, the joint is achieved through the interfacial reaction between Cu and Sn that form the IMC (K. N. Tu & Thompson, 1982). According to thermodynamics (Figure 2.2), the first IMC phase to form at the interface is Cu_6Sn_5 , and the second IMC phase (Cu_3Sn) is formed between Cu and Cu_6Sn_5 . Because the Cu_6Sn_5 phase is formed preferentially when in contact with molten solder, the morphology is irregular due to the liquid-solid reaction. The Cu_3Sn layer is rather planar, uniform and thinner, which reflects the solid-state diffusion of Cu and/or Sn through the Cu_6Sn_5 layer. The morphology of the IMC may differ for different Sn-based alloys because of different reaction kinetics.

The amount and rate of IMC formations at the interface relies both on the solubility of elements in the base material and on the reflow profile. Intermetallics are spontaneously formed within the bulk of the solder as the effect of melting and solidification and also as the precipitation of substrate as the metal dissolves in the molten solder. The progress is enhanced by the solid-state diffusion process of intermetallics during storage and operational service. The operational temperature seen by the solder joint is a relatively high compared to the low melting temperature (T_o to T_m). This scenario creates a relatively rapid solid-state reaction of Sn and Cu for IMC formation and hence results in low resistance of mechanical strength and creep.

The formation and growth of the IMC is an important factor that dictates the strength and lifespan of solder interconnections. Should the interconnections fail mechanically, the functionality of the electronic device can also be adversely affected. The relationship between IMC formation and the solder joint strength is the key issue to be identified to understand the deformation behaviour of solder joints. The strengths of Sn-based solder joints are discussed in the next section.

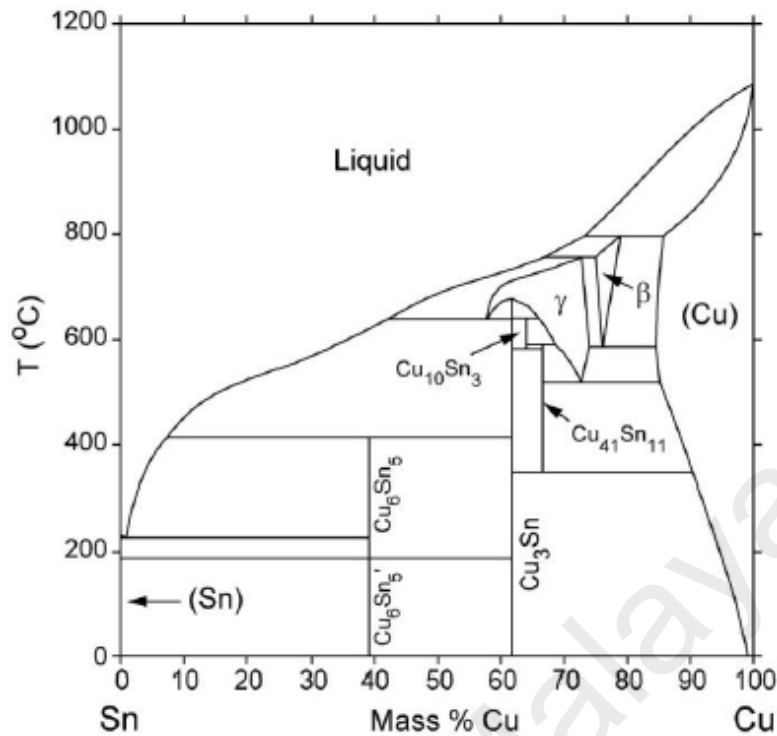


Figure 2.2 Cu-Sn binary phase diagram

2.2.2 Solder joint strength of Sn-based solder joints

Interconnections in electronic devices experience loads when in service or under impact. Under most circumstances, solder connections are prone to shear loading rather than tensile loading. Thus, the shear properties of solder materials determine the material's suitability for use in electronic packages. The mechanical properties of the solder joints are highly dependent on the solder composition, substrate material, flux, soldering conditions, joint geometry, and testing conditions (Miao, Duh, & Chiou, 2000; Tomlinson & Fullylove, 1992). Researchers have identified a few methods to simulate the loading conditions when the interconnections either are in service or experience external impact.

Investigation of thermal fatigue behaviour is one method to evaluate the strain induced when interconnections are in service. Solder joints are subjected to thermal shock, and the resultant shear strain is the sum of the linear thermal expansion of the carrier substrate and the differential thermal expansion between the solder and carrier substrate

(Sidhu & Chawla, 2008). Tu et al. (1997) have conducted a thermal fatigue test on Sn-37Pb/ Cu solder joints. The reflowed specimens were subjected to thermal cycling between -35 °C and 125 °C at a frequency of two cycles per hour until failure. It is reported that the thermal shock resulted in growth of the IMC layer, and the lifetime of solder joints monotonically decrease with increasing IMC thickness. The authors claimed that the thickening and flattening of the IMC layers are less resistant to crack formation compared to prism-like IMC structures (P. L. Tu, Chan, & Lai, 1997). In another work, Sn-6Bi-2Ag-0.5Cu/Cu solder joints prepared by mechanical alloying were exposed to a thermal shock environment of -25 °C to 125 °C for up to 1000 cycles (Huang, Wu, Lai, & Chan, 2000). These solder joints exhibited higher shear strength than Sn-37Pb and Sn-3.5Ag tested under the same conditions, probably because of the dispersion strengthening of small Bi particles and fine Ag₃Sn phase present in the solder alloy. The shear strength of Sn-6Bi-2Ag-0.5Cu/Cu solder joints decreased with increasing thermal shock cycles because of the increasing number of voids, which lead to crack initiation. The solder joints fail within the bulk solder and at the IMC/solder interface under all conditions (Huang, Wu, Lai, & Chan, 2000).

Another widely utilized test method that simulates real-life loading of the solder joints would be the ball shear test. Testing at different loading can simulate impact loading. Tomlinson and Fullylove (1992) have measured the shear strengths of copper joints soldered with six commercial Sn-based solders at 20 °C and 100 °C, each with a strain rate of 0.05 and 50 mm/min. The solders studied were pure Sn, Sn-1Cu, Sn-3.5Ag, Sn-5Sb, Sn-57Bi and Sn-2Ag-36Pb. Generally, Ag containing solders gave the highest strength values, whereas Sn-57Bi solder showed good ductility but did not follow the general pattern of shear behaviour under different test conditions. The shear strength and deformation behaviour of Sn-3.5Ag/Cu lap joints have also been studied by Deng et al. (2005). From both experimental and finite element analysis, those authors have concluded that the shear

strength of solder joints is controlled primarily by the solder strength rather than the IMC thickness. However, IMC thickness determined the fracture mode of the joints (Schlesinger & Paunovic, 2010).

Recent interests in the SAC-Fe/Al alloy as potential solder material has prompted investigations of the soldered joints. Kantarcioğlu et al. (2014) have investigated the effects of intermetallic compound (IMC) growth on the shear strength the solder joints. The minor additional effects of Al and Fe on the eutectic SAC alloy were investigated in detail under as-solidified conditions using combined techniques of electron microscopy, thermal and mechanical analyses. Keeping the cooling rate constant at 10°C/min, 0.05 wt% Fe-added specimens resulted in the smallest under-cooling. This is a desirable effect and resulted in an improvement of microstructure for Fe-microalloyed specimens. The formation of unwanted Ag₃Sn blades was found to be suppressed in Fe-modified specimens. Considerable amounts of Ag₃Sn were detected in the eutectic SAC and SAC-0.05Al specimens. The addition of microalloying elements led to the formation of new IMCs, i.e., FeSn₂ and Al–Sn–Cu for Fe- and Al-modified specimens, respectively. FeSn₂ formed in the vicinity of the solder/copper interface, and Al–Sn–Cu was distributed around the matrix. EDS results and Darken–Gurry predictions indicated a high volume of Fe substituted in Cu₆Sn₅ in place of Cu atoms. This causes a slowdown in the growing solid/liquid Cu₆Sn₅ interface, resulting in a lower under-cooling and formation of β-Sn dendrites before proeutectic Ag₃Sn blades. The enhancement of the microstructure after the addition of Fe was also confirmed by mechanical testing. Shear strength values of 0.01–0.1 wt% Fe-added specimens are considerably higher than the eutectic SAC and SAC-0.05 wt% Al solders. Decreasing the Fe content appears to enhance the mechanical properties. The new Al–Sn–Cu IMC developed in Al-added specimens was found to have an undesirable effect on the mechanical properties, based on fracture surface analyses of shear test specimens.

Date, Shoji, Fujiyoshi, Sato, and Tu (2004) are the first to report on component-level tests for evaluating the impact shear strengths of solder ball joints. They used a miniature pendulum tester, shown in Figure 2.3(a), to determine the fracture energy of solder joints. This early study was soon followed by several similar studies that also focused on assessing the shear strength of solder balls subjected to high loading rates. Ou, Xu, Tu, Alam & Chan (2005) have developed a miniature Charpy tester, shown in Figure 2.3(b), that they used to test a variety of lead-free solder joints under various thermal ageing conditions. From their observations of the failure modes, they noted a ductile-to-brittle transition point as ageing time increases.

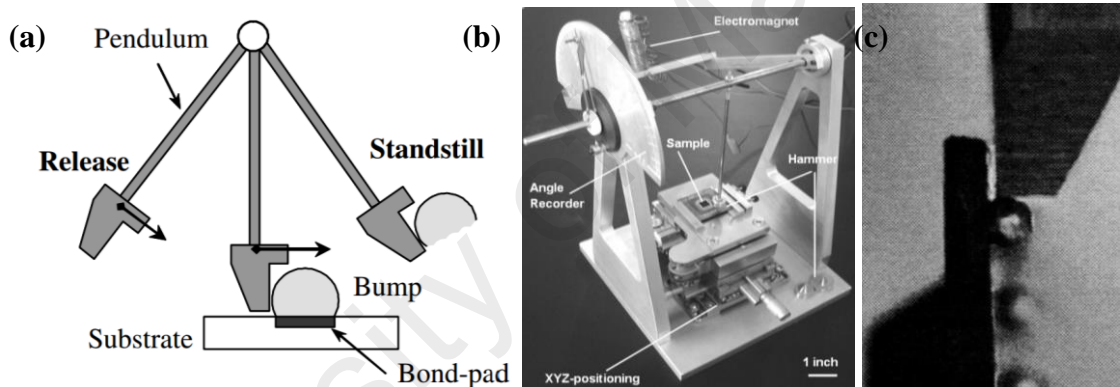


Figure 2.3: Impact shear test methods. (a) Pendulum tester (Date, Shoji, Fujiyoshi, Sato, & Tu, 2004) (b) Miniature Charpy impact tester (Shengquan, Yuhuan, Tu, Alam, & Chan, 2005) (c) Ball Impact Tester (Chang-Lin, Yi-Shao, Hsiao-Chuan, & Tsan-Hsien, 2005)

It was found that the shear force increased in parallel with the shear speed but decreased as shear height incline (Huang et al., 2001; Ricky Lee & Huang, 2002). This work used ball shear test to study the effects of shear speed and height on strength of Sn–37Pb solder in the experiment and the FEA with an NSMD (Non-Soldermask Define) pad opening substrate. Huang et al. (2002) reported the failure mechanisms was due to 3 types of failure modes. Kim et al. (2003) and Kim & Jung (2004) reported that the shear speed has an effect on the strength of In–48Sn solder alloy. The material has a low melting

temperature. Similarly on Sn–Ag and SAC Pb-free solder balls, which have high melting temperatures. The work also used experiments and simulation approach as conducted by Huang et al. (2001). This work revealed on the effect of shear speed that caused the shear force at the solder joints increased rapidly as the melting temperature of solder balls is lower. This indicated that lower melting temperature alloys possess higher mechanical strength as it requires more force to shear it. However, that study had excluded the shear height effects.

One interesting observation is that impact toughness increases with ageing time despite the increasingly brittle failure modes. Yeh, Lai, Chang and Chen (2005) have developed an impact shear device, shown in Figure 2.3(c), whereby the shearing blade is dropped from a height onto the solder ball sample. Using this “Ball Impact Test” method, they performed a correlation study between the impact shear tests and JEDEC board-level drop tests for five solder alloys and two pad finishes. They noted a correlation between impact energy/force in component-level tests and board-level drop impact performance for some of the materials tested. Song, Lee, Newman, Sykes and Clark (2007) have performed a comprehensive study of both high-speed shear tests and high-speed pull tests on solder bumps using a motorized ball shear tester (Dage high-speed shear tester). The results from these component-level tests were also compared to results from board-level drop tests. They noted that high-speed pull tests produced a higher percentage of brittle failure modes than high-speed shear tests. A correlation was observed between the proportion of ductile (or brittle) failures of joints in the component-level tests and the number of drops-to-failure in the board-level tests. However, there was a poor correlation between quantitative measures (energy and force from the component level tests) and the number of drops to failure. Zhao, Caers, de Vries, Wong and Rajoo (2007) have performed similar impact shear and correlation studies using a spring-loaded impact shear tool (Instron Micro Impactor). They also conclude that a qualitative brittle failure index, obtained from

observations of failure modes in component level tests, can be correlated to drops-to-failure in board-level tests. Since that study, motorized ball shear testers often been chosen by researchers to investigate the fracture modes (Y. Liu, Sun, & Yang, 2013) and solder joint strength affected by solder alloy composition (Kumar, Dohyun, & Jaepil, 2013; J.-M. Song, Liu, Lai, Chiu, & Lee, 2012; Sujan, Haseeb, Chong Hoe, & Afifi, 2014), reflow profile, substrate coatings (Kumar, Jung, & Jung, 2013) and shearing speed (Bui & Jung, 2014; Zheming, Jingshen, Zbrzezny, & McLellan, 2008). Table 2.1 summarizes the findings by other researchers using ball shear testers to investigate and draw their conclusions.

Table 2.1 Tabulation of findings for investigation of solder strength of a variety of SAC105 lead-free solder alloys with fourth element additions.

Solder Alloy	Variable	Tester	Summary of Finding	Source
SAC105	Coating	DAGE 4000	The average shear strength and fracture energy of SAC 105 is lower than SAC 305 and SAC 405.	Kumar et. al. (2013)
SAC105+Ni	Reflow profile	DAGE 4000	Drastic increase in the IMC layer thickness after 11 times of reflow and corresponded to a significant increase in IMC fracture mode.	(Toh, Liu, Tu, Chen, & Yeo, 2007)
SAC105+Zn	Tensile	Instron	Decrease in elongation and increase in UTS and 0.2% proof stress.	Song et. al. (2010)
SAC105+SiC	Tensile	Instron	drop impact improvement but a slight decrease of UTS, 0.2%YS and elastic modulus.	El-Daly et. al. (2013)

2.3 Effect of fourth element addition on SAC105 solder in terms of IMC layer, surface fracture and mechanical impact

The most common undesired attribute of a ternary SAC solder alloys is the formation of Ag_3Sn IMCs (Kim, Huh, & Sukanuma, 2003). These IMCs caused unfavourable effects on the mechanical properties, commonly on the strength of the solder joints. This issue is significant due to the electronic industry trend towards high density and miniaturization (Abtew & Selvaduray, 2000). SAC with low Ag content was predicted to solve this issue as lower Ag content form lesser Ag_3Sn IMCs. Thus in turn increase the mechanical reliability of the solder alloys. However, decreasing Ag content was found to lower the bulk strength and hence the mechanical performance (Lu, Balkan, & Ng, 2006; Luo, Chen, Hu, & Li, 2012). Therefore the recent effort on microalloying the SAC solder alloys with a fourth element (K. S. Kim, Huh, & Sukanuma, 2003). A wide range of elements including transition metals and post-transition metals such as Ni, Ge, Mn, Zn, Al, Fe, Bi (Benlih, Hong-Sik, & Ning-Cheng, 2007; Coyle et al., 2014; Mahdaviard et al., 2015; Mohanty & Lin, 2013; Mukherjee, Dasgupta, Zhou, & Bieler, 2014; D.-A. Shnawah et al., 2012; H. Y. Song, Zhu, Wang, Shang, & Lu, 2010; J.-M. Song et al., 2012; H. Zhang et al., 2014; Zhao et al., 2007) and rare-earth elements (J.-M. Song et al., 2012; D. Q. Yu et al., 2004) were proposed and investigated.

Minor alloying elements which could affect the growth of Cu-Sn compound are divided into two categories: (i) elements that show marked solubility in either one or both of the Cu-Sn IMCs; and (ii) elements that do not significantly dissolve in either of the Cu-Sn IMCs (Laurila et. al., 2009). The effect of elements in category 1 on IMC growth could be explained thermodynamically. These elements stabilize Cu_6Sn_5 and decrease the growth of Cu_3Sn . The elements in category 2 do not have a prominent effect on IMC as they only affect the growth of IMC layers indirectly. The addition of Fe has reduced the growth of Cu_6Sn_5 at the expense of forming FeSn_2 . Though Laurila et.al. (2009) have suggested Fe

insoluble in Cu_6Sn_5 and possibly will not alter the interfacial thickness. Whilst for Al addition, the growth of Cu_6Sn_5 has reduced. Anderson et al. have suggested that Al has some solubility in Cu_6Sn_5 . Hence a possibility of observing significantly altered interfacial layer Cu_6Sn_5 and Cu_3Sn .

2.3.1 Effects of addition of Ni and Ge

Ball impact tests were performed on SAC105 with minor alloying of a Ni/Ge solder ball soldered on Cu substrate (Lai et al., (2007)). The characteristics measured at an impact velocity of 500 mm/s for Ni/Ge added SAC105, which was compared to SAC405 performance at package-level solder joints on copper pad. Bulk solder fracturing was present in the as-mounted Ni- or Ge-doped samples. This indicated that the responses of Ni- or Ge-doped SAC solder alloys are more ductile than the conventional Sn-Ag-Cu. The addition of Ni or Ge to the solder alloy yields a substantial enhancement in which Ni alters the interfacial IMC structure (Figure 2.4), whereas Ge enhances the mechanical behaviour of the bulk solder. Among the five solder compositions examined in this study, Sn-1Ag-0.5Cu-0.05Ni was the most ductile, and Sn-4Ag-0.5Cu was the most brittle.

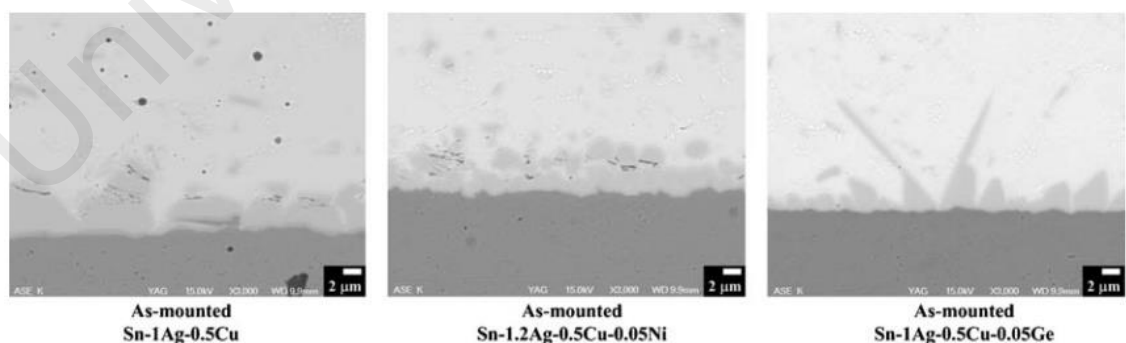


Figure 2.4: SAC105-Ni/Ge/Cu substrate interfacial reaction (Lai et al., 2007)

Benlih et al. (2007) studies the creep-resistant SAC-Al(Ni) solder alloy. Tensile and creep tests were performed to investigate the microstructure impact of the minor alloying.

It was concluded through microstructure observation that the non-stoichiometric IMC particle and large particle, although less effective in increasing yield strength, are still considered harder than Sn: therefore, they are expected to provide creep resistance. Addition of Al to SAC alloys reduces the number of hard Ag_3Sn and Cu_6Sn_5 IMC particles, forming larger, softer, non-stoichiometric AlAg and AlCu particles, as shown in Figure 2.5. This results in a moderate increase in the creep rate due to the reduction in yield strength. The addition of 0.1-0.6% Al in high-Ag SAC alloys is the most effective in softening and decrease the yield strength to SAC105 and SAC1505 level. Meanwhile, the creep rate sustained similar as the performance of SAC305.

The addition of Ni is found to form large $(\text{Ni,Cu})_3\text{Sn}_4$ IMC particles and consequently caused the loss of Cu_3Sn_4 particles. Similar to the addition of Al, it also causes softening of SAC alloys. As the addition of Al altered the microstructure to shift from near-ternary SAC eutectic towards a combination of eutectic SnAg and eutectic SnCu , the addition of Ni is found to cause a shift towards eutectic SnAg . The combination of SAC, Al and Ni in a single alloy possesses a pasty range and liquidus temperature which is approximately 4°C lower than SAC105 or SAC1505. Provided that the element addition is less than 0.6%. Unfortunately it was also found that the addition of Al and Ni produced a lower modulus and elongation at break, however tensile strength is unaffected (Huang et al. 2007).

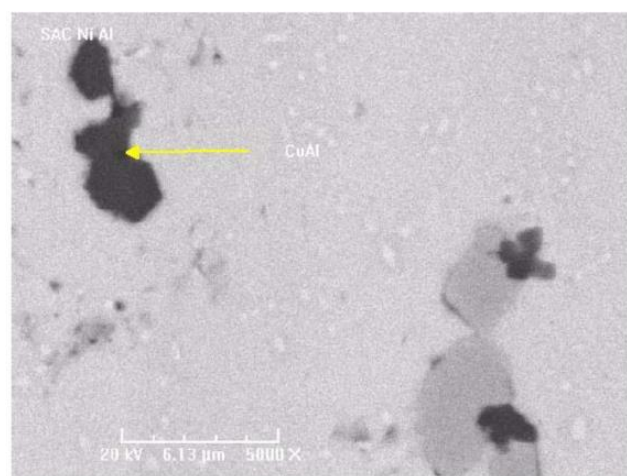


Figure 2.5: SEM of $\text{Sn}_{94.78}\text{Ag}_{4.0}\text{Cu}_{0.58}\text{Al}_{0.6}\text{Ni}_{0.04}$ (5000X) (Benlih et al. 2007)

The impact of surface finish (ENIG, ENEPIG, and OSP) on the shear properties and fracture behaviour of low alpha SAC-105 solder balls of 80- μm diameter have been investigated by Kumar et al. (2013). High-speed (from 10 to 3000 mm/s) shear tests were performed. Fracture energy has proven to be a better index than maximum shear force in interpreting the test results because the former better correlates with the fracture mode, as seen in Figure 2.6. Intermetallic compound composition and morphology have been found to have a significant effect on solder-joint strength. The shear strength of low-alpha SAC105 is found to be lower than the high-Ag-containing SAC305 and SAC405 solders, as shown in Figure 2.6.

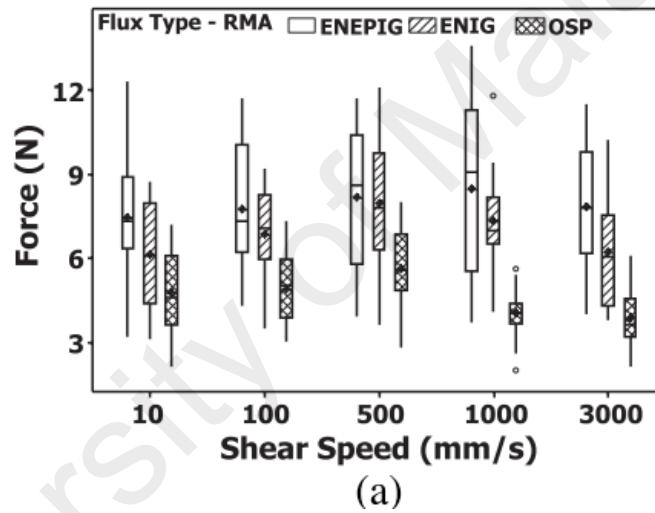


Figure 2.6: Graph of shear force as a function of shear speed for different pad finishes. (a) rosin flux. (Kumar et al., 2013)

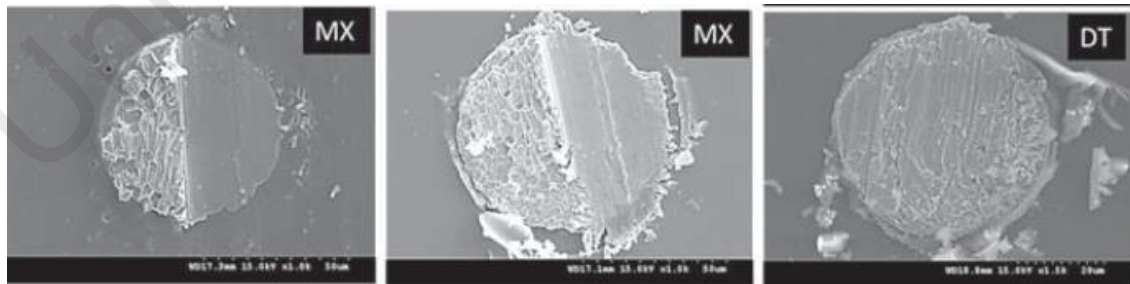


Figure 2.7: SEM images of the different fracture modes on Cu-OSP substrate (DT: ductile mode. MX: mix mode). (Kumar et al., 2013)

The minor addition of Ni in SAC105 was found to improve drop-shock performance compared to SAC105 and SAC305. This result was extracted from samples of solder alloys

assembled on Cu with OSP and Ni/Au surface finishes. The improvement was ascribed to the thicker IMC at the solder/substrate interface (Zhu et al., 2008). It also formed large $(\text{Ni,Cu})_3\text{Sn}_4$ IMC particles and caused the loss of Cu_6Sn_5 particles, resulting in the softening of SAC alloys. In addition, the inclusion of Ni drives microstructure shifting towards eutectic SnAg (Benlih et al., 2007)

2.3.2 Effects of addition of Al, B and SiC

Adding Al by 0.1-0.6% to SAC alloys is most effective in softening and sustaining the yield strength at the same level as SAC105, while the creep rate is similar to the SAC305 level. A slight decrease in modulus and elongation at break was also observed, although the tensile strength is not affected. Another finding for addition of Al from 0.2wt% to 1wt% into SAC105 was reported to demonstrate limited solubility of Al in the solder matrix. The formed Al-Cu and Al-Ag particles (Benlih, Hong-Sik, & Ning-Cheng, 2007)

The minor addition of Al below 0.5wt. % has found to enhance the SAC105 solder alloy by suppressing the growth of the interfacial Cu_6Sn_5 intermetallic compound (IMC). The modified SAC105 also exhibited higher hardness and modulus although inclusion of Cu_3Al_2 and Cu_3Al_2 IMCs mostly found near surface/edges. Besides, it was proven that addition of trace Al in SAC105 does not alter the morphology of the interfacial intermetallic compounds. Interestingly, additions of Al manage to control the thickness of Cu_6Sn_5 IMC layer. However, there is no significant effect on the thickness of Cu_3Sn . The governing mechanism was ascribed to the Al atoms hinder the flow of reacting species at the interface.

The effect of trace element addition (up to 0.1 wt %) of Boron (B) on the soldered joint on a Cu substrate were investigated by Choi et al., (2012). It was found that after ageing and multiple reflow, B-doped SAC105 exhibit superior solder joint strength by retaining the strength at 743 to 909g while SAC105 strength drop to 355g from 850g. Additionally,

after 10th reflow, the strength of the SAC105-0.05B sample was 115% higher than the SAC105. The superior performance was discussed to be ascribed to the reduced rate of grain growth in the IMC layers of B-doped solder joints after under ageing. Figure 2.8 presents the microstructure of B-added SAC105 before and after aging for 100h.

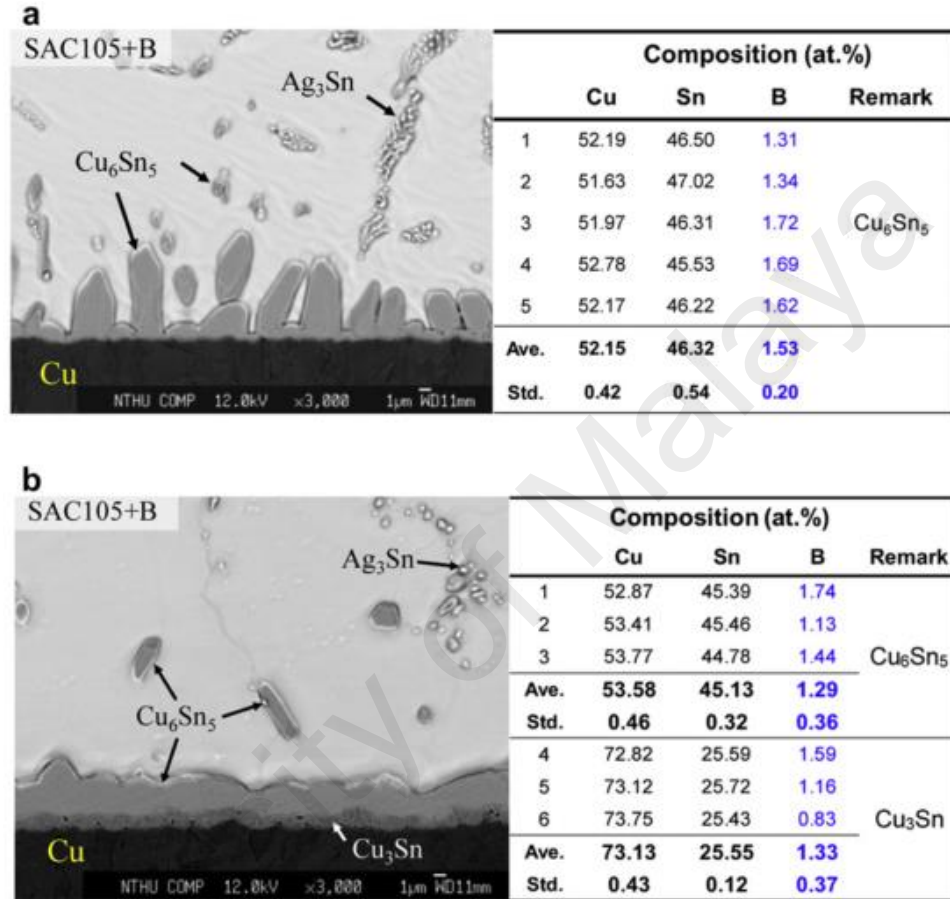


Figure 2.8: EPMA analysis on the distribution and composition of boron in the Cu₆Sn₅ and Cu₃Sn IMC interface layers of the solder joint doped with 0.1 wt.% B (a) before and (b) after aging at 150°C for 100 h. (Choi et al., 2012)

The IMC thickness evolves in parallel with ageing time. In contrast, the fracture force decreased. As shown in Figure 2.9, the IMC thicknesses of SAC105 and SAC105-0.05B solder joints with and without ageing differed approximately 3μm to 4μm, near to the values of 2-4 μm that were reported for Sn/0.3Ag/0.7Cu solder joints. These figures are much lower than that for the reported SAC305 solder joint (Oh et al., 2009). Interestingly, the thickness of the IMC layer seemed to have no effect to the strength of the joint.

However, retarded IMC layer growth generally is beneficial to the strength at joint (Chen et al., 2006; Chin et al., 2008; Yoon et al., 2008; Mayappan et al., 2010). Though the IMC layers measured for SAC105-0.05B sample after ageing for 200 h is 63% thicker, the joint strength was 156% greater than the baseline SAC105.

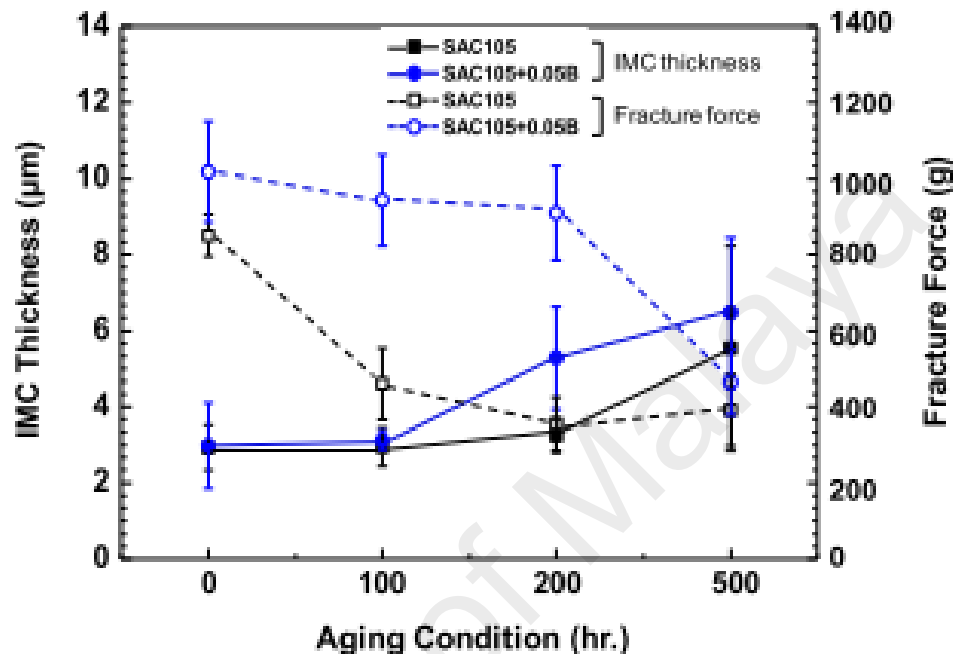


Figure 2.9; Changes in the IMC thickness and fracture force under the high-speed ball pull test at 400 mm/s after aging at 150°C for various aging times (hr). (Choi et al., 2012)

El Daly et al., (2013) studied the SiC nanoparticles mixing in SAC105 solder. The addition of SiC nanoparticles had effectively decreased the formation of Ag_3Sn and Cu_6Sn_5 and also form primary $\beta\text{-Sn}$ phase more. This eventually creates a weak interface with the solder matrix that in turn has resulted in improved ductility, lower UTS, elastic modulus and yield strength. The conclusion was made that the plasticity was improved as the better structural refinement through sub-grain sizes alteration by primary $\beta\text{-Sn}$ phases. This adjustment allowed the solder alloy to display larger elongation. The effect of reduction in undercooling makes the SiC nano-sized a reliable alloying element for existing soldering process as it maintained at the SAC105 behaviour. Furthermore, ductile fractures as seen in Figure 2.10 were found on SiC nanoparticle mixed SAC105. Similar modes were seen on

SAC105 solder alloy. Micro-voids coalescence caused the dimples fracture. Meanwhile generally, the cup and cone fracture mode is a typical to ductile materials. The larger and deeper dimple indicated a better plasticity (Song et al., 2010; Subramaniam et al., 2012). Hence, as shown in Figure 2.10, the fracture surface of SiC-contained SAC105 appeared to be more ductile than SAC105. As it shows rough and deeper dimple surface than SAC105 solder. This could be due to the distribution of uniform SiC nano-particles within the matrix. Conclusively, the plasticity improve by SiC nanoparticles addition.

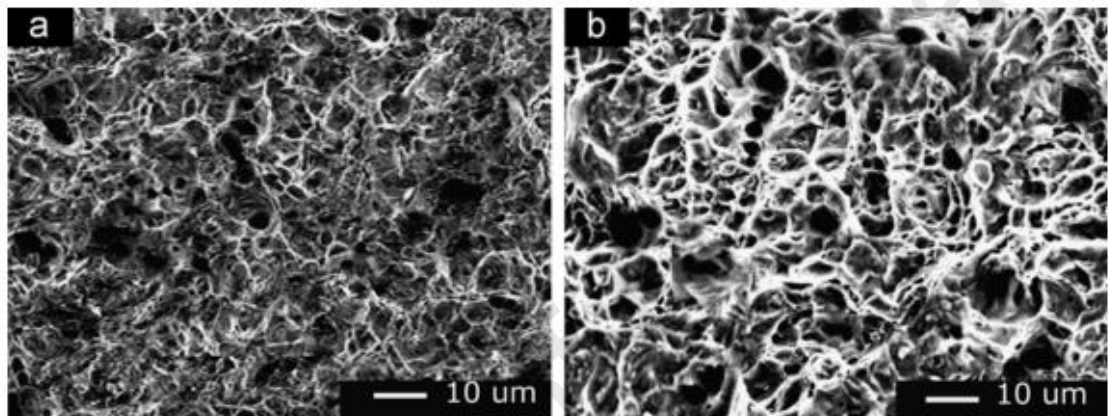


Figure 2.10: SEM fractrograph for (a) SAC105 and (b) SAC105–0.75SiC solders.(El-Daly, Fawzy, Mansour, & Younis, 2013)

2.3.3 Effects of addition of Mn and Ti

The beneficial impact of Mn and Ti additives on mechanical properties, microstructure and solidification of SAC105 were investigated by Lin et al. (2009). It was found that by alloying with Mn and Ti, undercooling reduce, coarser eutectic structure and dendritic size refinement through the extension of the proeutectic Sn volume fraction. Correlation on the element alloying impact on thermal and microstructural changes was ascribed to the formation of IMCs such as MnSn_2 and Ti_2Sn_3 which were formed in Mn-doped and Ti-doped alloys, respectively. By performing nanoindentation, as demonstrated in Figure 2.11, the fourth element alloying produced heterogeneous IMCs which were found harder and stiffer than Ag_3Sn and Cu_6Sn_5 that are also found in SAC alloys. The modified alloy

possesses a microstructure with shrunken eutectic regions and coarsened eutectic microconstituents. Hypothetically, the prediction was made that with higher additives, elastic modulus will ascend due to the increase of strength caused by the heterogeneous IMCs.

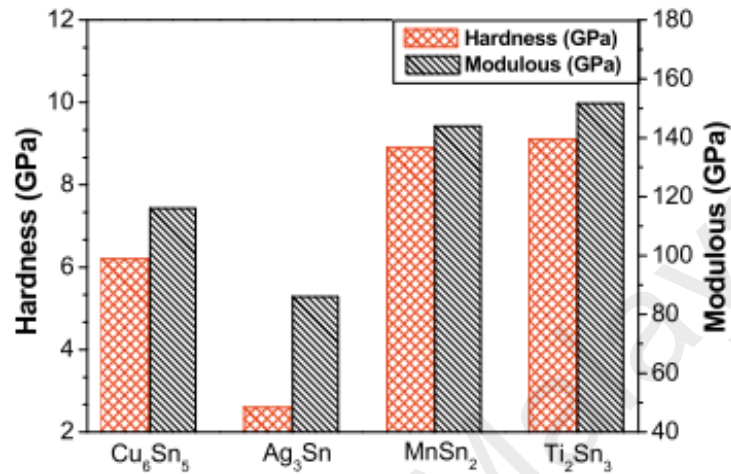


Figure 2.11: Nanoindentation results of the intermetallic phases. (Lin et al., 2009)

Rishi K. (2011) compared the tensile performance of SAC105 with the minor addition (0.1wt%) of Ti, Ni, Mn and rare earth. Conclusively the tensile strength of SAC105 with addition of Ti, Ni and Mn reported a better performance compared to the alloying with rare earth namely La, Ce and Yy. The better performance of Ti and Ni contained SAC105 were ascribed to the more ductile microstructure that created ductile fracture which consist microvoids and dimples. While the lower performing rare earth contained SAC105 displayed large microvoid and flat fracture surface which resulted in a brittle fracture.

2.3.4 Effects of addition of Fe and Bi

The effect of Fe and Bi addition on the microstructure, mechanical, and thermal properties of the SAC105 were investigated by Mahdavi et al. (2015). The addition was found to increase the yield and ultimate tensile strength (UTS). However, it also decreased the total

elongation. The effects are ascribed to the solidification and strengthening effects by Bi precipitation in the Sn matrix. While 0.05 wt.% Fe made few FeSn_2 in the solder bulk that was observe has no significant impact on mechanical properties. Addition of Bi creates particles that scatter in the bulk of SAC105-Fe solder alloy which increased β -Sn and degenerated Cu_6Sn_5 and Ag_3Sn into a chain-like arrangement. As shown in Figure 2.12, SAC-Fe-Bi solder alloys produce a brittle fracture mode. The inclusion of Bi hindered β -Sn to deform and thus decreased the ductility.

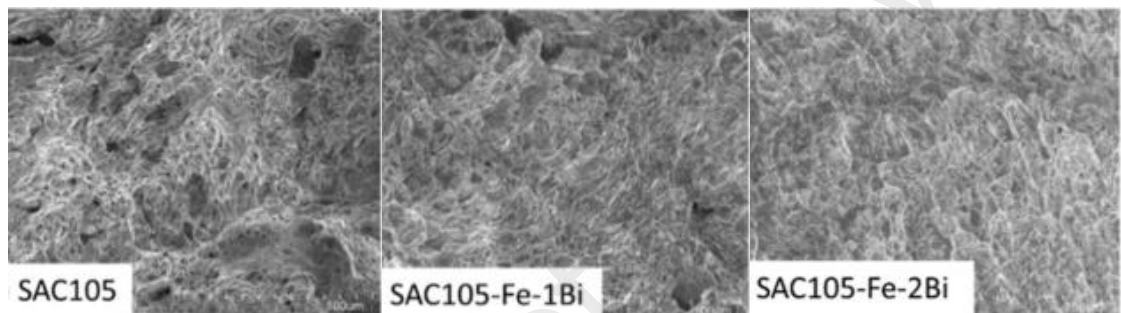


Figure 2.12: SEM images of fracture surface of SAC105, SAC105-Fe-1Bi, SAC105-Fe-2Bi. (Mahdavi et al., 2015)

Shnawah, Said, Sabri, Badruddin, & Che (2012) has investigated the minor addition of Fe in SAC105. The material exhibit a promising attributes as its melting temperature is similar to the established SAC105. Although the elastic modulus was reduced, the alloy demonstrated a longer plasticity region which enhances the elasticity when it is put under the same loading condition. This signifies a better ductility. The grain coarsening was found to be slow under thermal aging which indicated that the material is aging resistant. The addition of Fe was reported to alter the microstructure of SAC105 as it forms large circular FeSn_2 . This adds up to the readily available Ag_3Sn and Cu_6Sn_5 particles. The microstructure of this Fe-added SAC105 is as shown in Fig. 2.13.

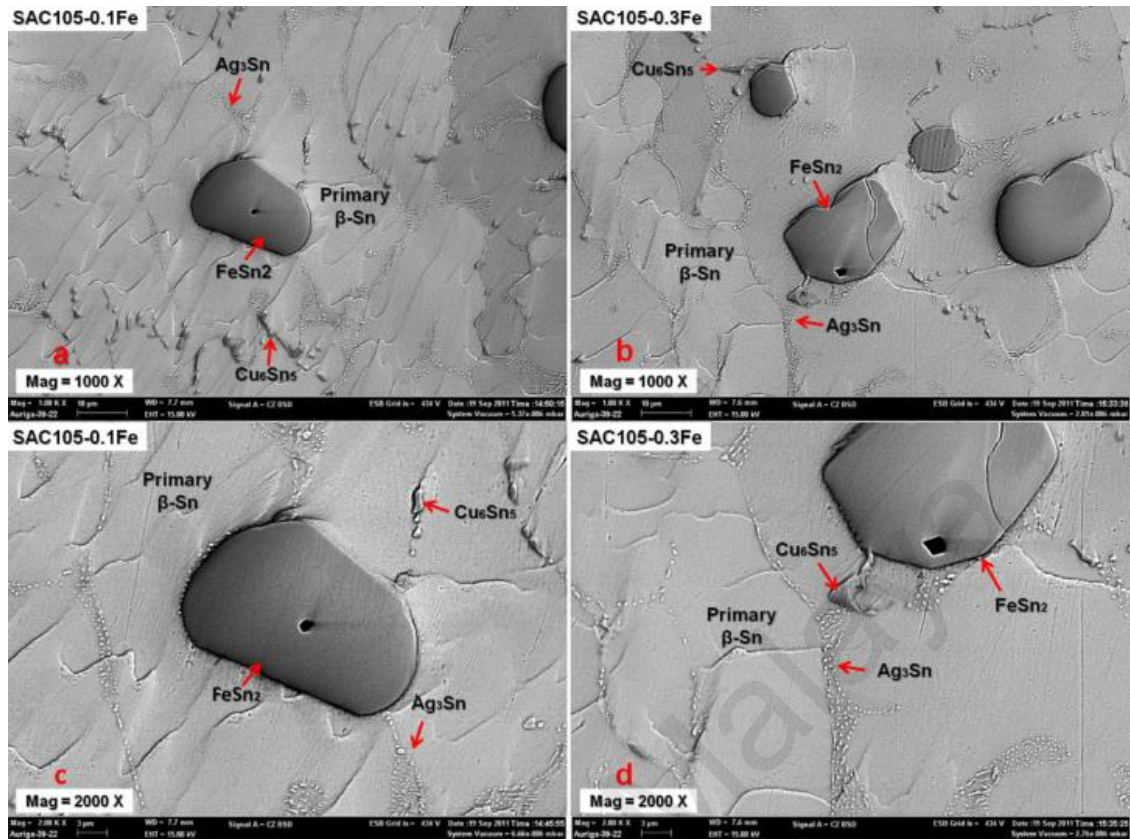


Figure 2.13 Microstructure of SAC105 and SAC105-xFe (Shnawah, Said, Sabri, Badruddin, & Che, 2012)

The effects of these microalloying elements highly depend on solidification rates (Swenson, 2007) and the concentration of the added fourth element (Anderson, 2007). The impact is on the alteration of microstructure by the addition of new IMCs after microalloying. The ability of the altered microstructure to enhance the solder performance is controversial. The outcome was found to be both good and bad. Some has concluded that element addition was able to reduce or suppress the formation of Ag_3Sn by decreasing the undercooling that enable easier nucleation of Sn solidification. On the other hand, some studies contend that IMCs have no obvious roles in inhibiting Ag_3Sn blade formation rather IMCs in excess quantities cause further embrittlement (Harris & Chaggar, 1998)

2.4 Electronics products assembly and packaging process

In electronics assembly and packaging, materials are exposed to diverse and combined condition of liquids, gas, temperature range and also pollutants. This mixed of these parameters rationally will impose chemical reaction. The requirement of environment and condition of a facility is different from one product to another. It is vital for all of the electronics products manufacturers and suppliers of assembled products to abide to the relative humidity (RH) in the production facility. As lower RH than requirement will compromise the products towards the ESD (Electro Static Discharge) related defects. The humidity in the air tends to ascend the surface conductivity, which subsequently cause the dissipation of the electrostatic charges. Commonly, ESD recommends an optimum RH of 40%, given that it does not promote delamination or corrosion of the materials used. Due to the complexity of the devices and components, product failures are cause by many issues, but one of the underestimated propagator of the failure is from moisture. Through the released standard by JEDEC in J-STD-033B1 and also IPC (Association Connecting Electronic Industries) in IPC-M-109, the condition and environment of moisture sensitivity level during products assembly is explicitly outlined. The later standard outlined 8 moisture sensitivity levels to be adhered by manufacturers. Moisture sensitivity level (MSL) could also be related to the precautions during handling and packaging of semiconductors. The MSL is a standard to monitor period of exposure of a moisture sensitive device within an ambient room conditions. The approximation is about 30° C of 60% RH for general products and will differ among products on the level of sensitivity towards moisture.

To date, the trend of the semiconductors manufacturing is towards smaller sizes. Thin and fine-pitch components and ball grid arrays (BGA) could be harmed during reflow as moisture trapped inside the component expands. The expansion of trapped moisture often causes delamination of the plastic materials from the die, damage to the wire bond and die

and also the internal cracks. All of these damages are invisible from the component surface. Additionally, the trapped moisture will also impose a spontaneous electrochemical reaction where a flow of electricity between certain areas of a metal surface through a solution capable of conducting an electric current. This electrochemical action causes destructive alteration of contact area as the weaker metal dissolve or flakes off. Simply, it's an effect of corrosion which is a complex function of many factors, but the three most important are about the voltage differential between noble and weaker elements in the area, physical conditions of temperature and humidity and also the presence of oxygen in the air.

It was discussed by Yoon, Noh, Lee, Lee and Jung (2008) on the impact of the temperature-humidity (TH) on the joint integrity of SAC305/Cu OSP ball grid array assembly. There was an association between mechanical reliability of the solder joint for the materials being aged and exposed in humidity. The voids caused by the oxidation of the OSP-finished Cu substrate during the TH test were responsible in deterioration of solder/Cu shear strength. While the impact of TH on the aged and IMC evolution was found to be insignificant

2.5 The impact of dissimilar metals of Sn-based solder alloy in humidity

Dissimilar metals that are placed together in the presence of moisture will eventually lead to the occurrence of dissimilar metal corrosion which is known as galvanic corrosion. This commonly comes in pair with pitting type of corrosion. The process involves the materials in contact with each other to oxidize or corrode. For this event to occur there must be two electrochemically dissimilar metals present to form a spontaneous redox couple, the presence of electrically conductive path between the two metals and also a conductive path for the metal ions to move from the more anodic metal to the more cathodic metal. Tin-based solder alloys in electronics products are prone to electrochemical reaction as the alloy is composed of a few metals with different anodic potential. Whereas the trapped

moist from contaminants or other sources could contribute to an electrolyte-like environment.

2.5.1 Potential risk assessments of material exposed in humid environment

Seawater is one of the most corrosive and most abundant naturally occurring electrolytes. The corrosivity of seawater is illustrated by its ability to attack most common metals. Alkaline solution such as sodium chloride (NaCl) is normally used as an electrolyte in simulation of natural seawater which implies on a harsh humidity exposure or threat. The aggressive nature of this solution is attributed to its high ionic conductivity. In standard testing condition provided by Joint Electron Device Engineering Council (JESD22-A107C), International Electrotechnical Commission (IEC) and American Society for Testing and Materials (B117), the acceptable ionic conductivity for a NaCl salt exposure for testing of electronics application is achieved at a concentration between 3.5 wt% and 5 wt.%.

2.5.2 Potentiodynamic polarization analysis of Sn-based solder alloys in sodium chloride: basic principles

Figure 2.14 shows the schematic profile of the potentiodynamic polarization for the Sn-based lead-free solders in a solution containing NaCl (Wu, Chan, & Alam, 2006). The content of the polarization analyses are the corrosion potential (E_{corr}), corrosion current (i_{corr}) and the critical current density at total passivation stage (Rosalbino, Angelini, Zanicchi, Carlini, & Marazza). The passivation properties of materials will also be revealed through the analysis. Generally, material passivation is observed from the plateau curve profile viewed at current progression at the anodic region. This plateau is caused by the reaction behave independent from the increase in the applied potential. The passivation

behaviour corresponds to the formation of passivation film as the barrier that shields the material surface against further corrosion. The passivation current density (I_p) indicates the reliability of the passivation film. A better surface protection if the I_p is small. In most cases, Pb-free solders produce multi passivation regions that involve primary and secondary passivation.

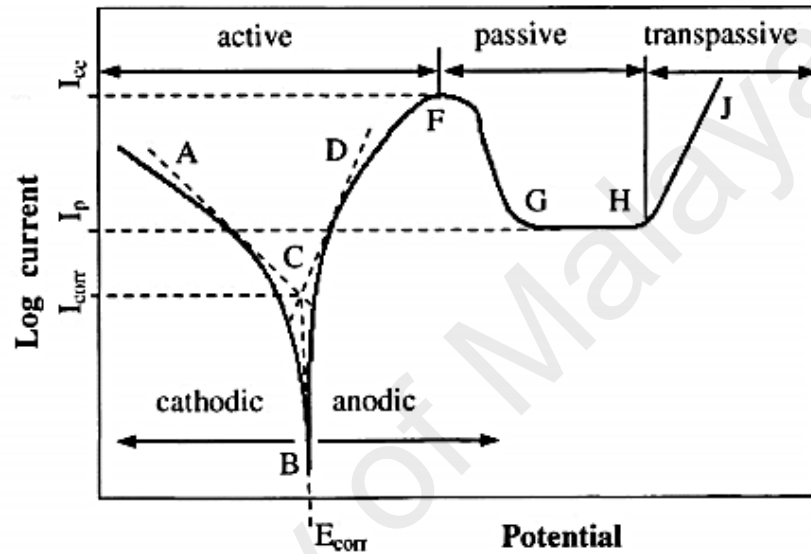


Figure 2.14: Electrochemical Potentiodynamic curve for lead-free solder (Wu, Chan, & Alam, 2006)

Yokoyama, Nogami and Sakai (2014) studied the effect of Ag and Cu addition to Sn on the potentiodynamic polarization behavior in 0.9 wt. % NaCl aqueous solution under aerated conditions and using a scan rate of 20 mV/min at room temperature. Polarization of both Sn-3Ag and Sn-0.5Cu resulted in almost identical curve. Differences were only recorded once the samples were tested under tensile loading and under surface morphology imaging using SEM. It was found that in the solution, preferential dissolution of Ag or Cu probably occurred in both materials. Compared to addition of Ag, minor addition of Cu exhibit superior corrosion resistance and it seemed that 0.9 wt% NaCl solution has no effect on crack nucleation for Sn-0.5Cu alloy under applied tensile stress.

Tsao and Chen (2012) had discovered the role played by Cu_6Sn_5 intermetallic (IMC) in corrosion resistance ability of Sn-based solder. In Table 2.2 (a), it is evident that increase in Cu brings the materials to a more noble state where corrosion potential is decrease while significantly large corrosion current was noted for pure Cu. Hence, suggestively for a SAC solder alloys, formation of more Cu_6Sn_5 intermetallics will increase the corrosion resistance of the material. Also, at the SAC/Cu joint where this IMC will form indicated that corrosion attack might be unlikely to occur.

Table 2.2: (a) Corrosion properties in 3.5 wt% NaCl solution for Sn, Cu and the intermetallics (b) Corrosion products and its morphology (Tsao & Chen, 2012)

(a)	Specimens	E_{corr} (mV _{SCE})	E_b (mV _{SCE})	ΔE (mV)	I_{corr} ($\mu\text{A}/\text{cm}^2$)
	Sn	-825 ± 23	-378 ± 16	447	1.73 ± 0.51
	Cu_6Sn_5	-460 ± 18	-12 ± 18	448	3.17 ± 1.12
	Cu_3Sn	-311 ± 21	-5 ± 15	306	22.65 ± 4.70
	Cu	-192 ± 16	236 ± 23	428	391.6 ± 16.41

E_{corr} : corrosion potential, I_{corr} : corrosion current density,
 E_b : breakdown potential, $\Delta E = E_{\text{corr}} - E_b$.

(b)	Sample	Surface element concentration (wt.%)				Morphology
		Cu	Sn	Cl	O	
	Sn	–	81.62	9.43	8.95	Platelet-shaped
	Cu	67.0	–	31.56	1.41	Triangular-shaped
	Cu_3Sn	54.0	10.39	24.27	11.34	Spiral shell
	Cu_6Sn_5	32.24	41.72	20.32	5.72	Coarse gravel
		35.09	38.82	21.74	4.25	Fine gravel
		32.67	40.0	21.51	5.82	All area

In table 2.2 (b), the morphology of the corrosion products were well classified. It could be suggested that the nature of fine gravel distributed on all area is the reason on a sturdy surface against corrosive ions. As Sn exhibit a platelet and flake-like corrosion layers as seen in Fig. 2.15(a), which enable easy rupture in the solution and eventually will provide bigger area contact ratio to the corrosion ions.

The work also outlined on the galvanic current densities for pure Sn with respect to Cu_3Sn , Cu, and Cu_6Sn_5 are about 12.12, 5.70, and 1.12 $\mu\text{A}/\text{cm}^2$, respectively. Which further confirmed that more stable reaction between Sn and Cu_6Sn_5 as the galvanic current is the closest which will result on unlikely to very small amount of Sn dissolution.

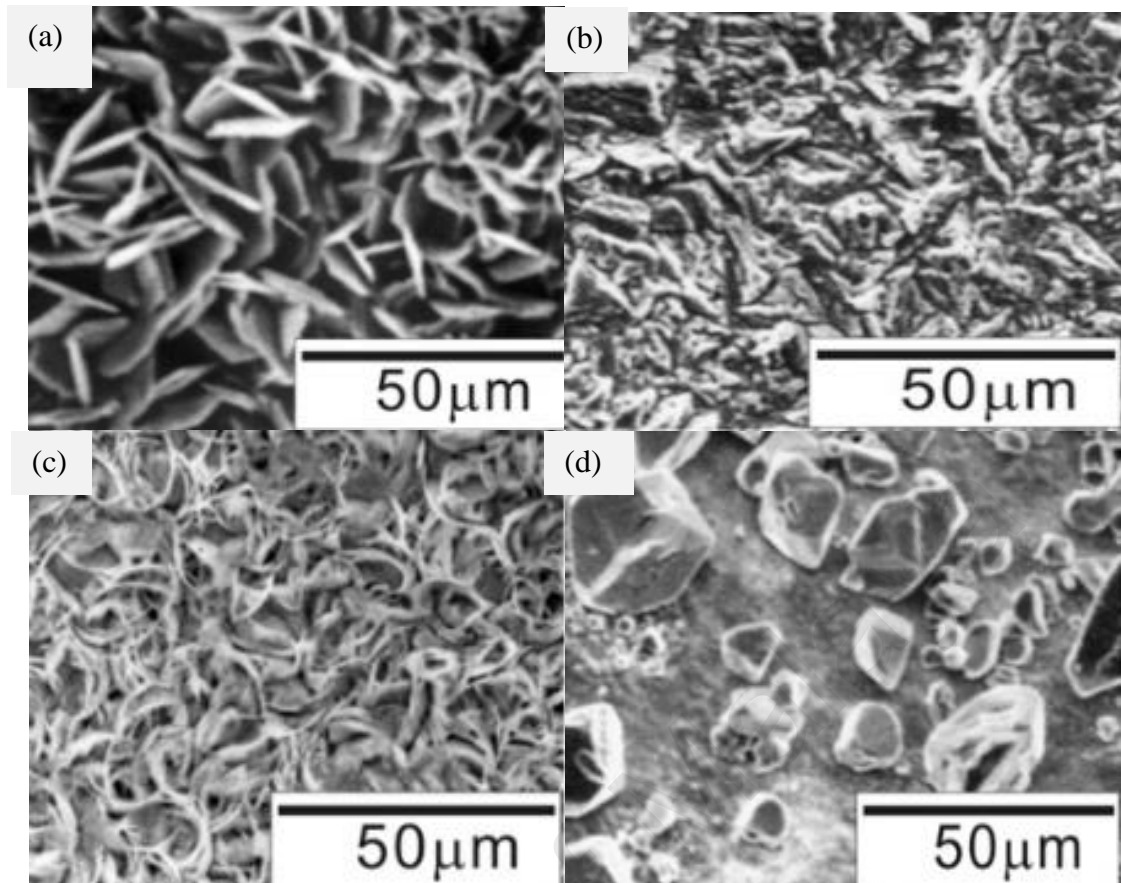


Figure 2.15: Corrosion products of the surface of (a) Sn (b) Cu (c) Cu_3Sn (d) Cu_6Sn_5 (Tsao & Chen, 2012)

Similarly, Wierzbicka-Miernik, Guspiel and Zabdyr (2015) has found that a decrease of Cu in ternary SAC alloy exhibit a more corrosive material. The study used high Ag content (S1: Sn-3.8wt% Ag- 0.7wt% Cu) and S2: (Sn-3.66wt% Ag- 0.91wt% Cu) SAC solder alloys that were immersed in NaCl with concentrations of 0.01, 0.1, 0.5 and 1M. As listed in table 2.3, the recorded result shows corrosion potential increase for lower Ag content by 3.68% and by 23.07% for increase in Cu. This pattern of reaction is found throughout all solutions used. The passivation range is observed to be shorter in higher concentration of NaCl. Pure Sn recorded the longest passivation range followed by S2(Sn 95.5wt%) and S1(Sn 95.43wt%). Higher concentration of NaCl contains more Cl^- that is active in causing the rupture of SnO layer. This is visible as the considerable increase of anodic current, which corresponded to the active dissolution of Sn stimulated by the Cl^- ions with the formation of soluble complexes of the SnCl_3 and SnCl_6 .

Table 2.3: Corrosion potential and current density for S-1 and S-2 solders (Wierzbicka-Miernik, Guspiel, & Zabdyr, 2015)

NaCl	Samples	E_{corr} (mV)	I_{corr} (uA/cm ²)
0.01M	S1:Sn-3.8wt% Ag- 0.7wt% Cu	-460	0.8
	S2:Sn-3.66wt% Ag- 0.91wt% Cu	-535	0.63
	Sn	-720	0.5
0.1M	S1	-525	0.83
	S2	-615	0.63
	Sn	-737	0.56
0.5M	S1	-541	1.00
	S2	-630	0.75
	Sn	-740	0.63
1M	S1	-549	1.2
	S2	-665	0.8
	Sn	-767	0.7

Rosalbino, Angelini, Zanicchi, Carlini, & Marazza (2009) also in the study that polarized two compositions, Sn–3Ag–0.5Cu and Sn–3Ag–3Cu (at%) in 0.1wt% NaCl had discovered that the SAC solder with lower content of Cu exhibit a more corrosive behavior. In this study, the decrease of the potential was associated with the increasing number of pores and surface roughness. The reduce amount of IMCs formation were found in SAC305. Specifically, it was demonstrated that higher count of IMCs contents make a material more resistant to corrosion induced by Cl^- .

As summarize in table 2.4, a careful planning on the setting for the test is required to minimize discrepancy in analyzing the result. As overall, it is important to set the scan rate sufficiently low to allow adequate penetration of corrosive agent and on adequate surface contact.

Table 2.4: The summary of some setting for the potentiodynamic polarization

Materials	Method	NaCl (wt%)	Scan rate (mV/s)	Area (cm ²)	Electrodes	Ref
Sn-Cu, Sn-Ag, SAC305	Potentiodynamic Polarization	0.9	20	-	Pt, SCE	(Yokoyama et al., 2014)
Sn,Cu Cu ₆ Sn ₅	Galvanic Potentiodynamic	3.5	1	0.785	Pt,SCE	(Tsao & Chen, 2012)
SAC405	Potentiodynamic Polarization	0.01,0.1,0.5, 1M	1	0.49	Pt,SCE	(Wierzbicka-Miernik et al., 2015)
SAC305 Sn-3Ag-3Cu	Potentiodynamic EIS	0.1M	0.5	0.5	Pt, SCE	(Rosalbino et al., 2009)

2.5.3 Sn-based solders under Salt Spray Test

Fubin and Lee (2006) used salt spray test to investigate corrosion impact at the board level, specifically corrosion attack at the solder/substrate joint. The study used a high Ag content SAC solder, the SAC405. With the increase in the Ag content is the material, amount of IMCs were proportionally rise. Hence the distribution of larger amount of Ag₃Sn IMC within the solder matrix. It is notable that potential of Ag₃Sn is similar to the noble Ag. Potential differences with the SAC alloy create instability of ions and more active element will react easily. However in this study, it was proven through the investigation at the locus of corroded spot that Ag₃Sn accelerate dissolution of Sn. It is evident for Figure 2.16 that through this study, SAC405 is highly susceptible to corrosion.

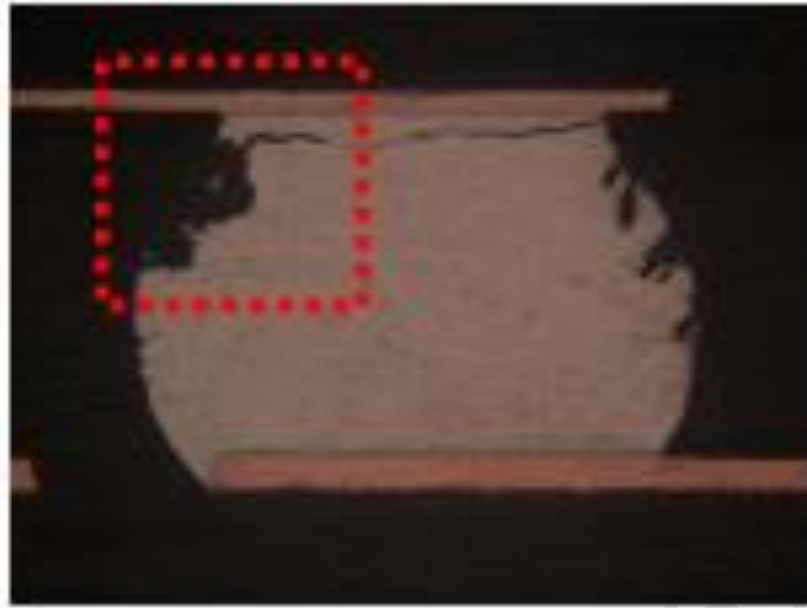


Figure 2.16: SAC405 after 96hr in salt spray test (Fubin & Lee, 2006)

For Sn-based solder alloys, it might be possible to induce that the expected corroded surface will be covered with a mixed of oxidized Sn and also Sn which reacted with hydroxide and chloride ions. Table 2.5 discretely outline the compounds that were found previously on corrosion test perform on some Sn-based alloys. The formations of corrosion products were characterized by using AES, XPS, XRD and SIMS.

Table 2.5 Corrosion products associated with to Sn-based solder alloy in NaCl solution

Materials	NaCl	Anodic reaction	Corrosion	Ref
	wt%		Product	
Sn	3.5	$3\text{Sn} + 4\text{OH}^- + 2\text{Cl}^- - 6\text{e}^- = \text{Sn}_3\text{O}(\text{OH})_2\text{Cl}_2 + \text{H}_2\text{O}$ (Sn oxyhydroxychloride)	$\text{Sn}_3\text{O}(\text{OH})_2\text{Cl}_2$	(Mohanty & Lin, 2013)
Cu	3.5	$\text{Cu} + \text{Cl}^- = \text{CuCl} + \text{e}^-$	CuCl	(Tsao & Chen, 2012)
Cu₃Sn	3.5	$3\text{Sn} + 4\text{OH}^- + 2\text{Cl}^- - 6\text{e}^- = \text{Sn}_3\text{O}(\text{OH})_2\text{Cl}_2 + \text{H}_2\text{O}$	CuCl $\text{Sn}_3\text{O}(\text{OH})_2\text{Cl}_2$	(Tsao & Chen, 2012)
Cu₆Sn₅	3.5	$\text{Sn}(\text{OH})_4 = \text{SnO}_2 \cdot \text{H}_2\text{O} + \text{H}_2\text{O}$	SnO_2 , Cu_2O $\text{CuCl}_2 \cdot 3\text{Cu}(\text{OH})_2$	(Tsao & Chen, 2012)
SAC405	0.01-1M	$\text{Sn}(\text{OH})_4 = \text{SnO}_2 \cdot \text{H}_2\text{O} + \text{H}_2\text{O}$	$\text{SnOHCl} \cdot \text{H}_2\text{O}$, $\text{Sn}(\text{OH})_4$ and SnO_2	(Wierzbička- Miernik et al., 2015)
		$3\text{Sn} + 4\text{OH}^- + 2\text{Cl}^- - 6\text{e}^- \rightarrow \text{Sn}_3\text{O}(\text{OH})_2\text{Cl}_2 + \text{H}_2\text{O}$	$\text{Sn}_3\text{O}(\text{OH})_2\text{Cl}_2$	(Mohanty & Kwang-Lung, 2007)
Al		$2\text{Al} + 3\text{H}_2\text{O} \rightarrow \text{Al}_2\text{O}_3 + 6\text{H}^+ + 6\text{e}^-$	SnO	(Khireche, Boughrara, Kadri, Hamadou, & Benbrahim, 2014)

2.6 Numerical modelling of solder joint failure

Solder joint reliability relies on the fatigue failure of solder joints and is possible to easily address by its life prediction. Commonly for fatigue, the assessments of in-service reliability of electronic packages involve an uneconomic and very time consuming cycling of thermal/mechanical shock and tests in humidity. The accelerated test has become more relevant as it is shorter to deliver result. Solder alloys are malleable materials with viscoplastic behaviour. Hence, it is a challenge to predict the material's fatigue life under the high homologous due to the dependency towards time, rate and temperature. The exploration on the subject has to consider all temperature profiles, including ramping, dwell time and temperature and also the effects on microstructures and correlated IMCs alterations. For solder joint, fatigue failures are related to the entire electrical open circuits, crack initiation and propagation along solder joint and drop of stress amplitude at joint.

Recent methods to investigate solder joint reliability involve both computer modelling and accelerated test with combination of test conditions. Initial setup commonly based on input from the experiment methods and outputs. Typically for prediction, most models will require stress-strain data. Reduction of dimensions of electronics devices had developed solder joint with a size that is difficult to monitor. Thus, the easier approach is by using finite element analysis (FEA) modelling. Generally, there are four primary steps to model fatigue. The first is the basis for modeling, which is the theory or constitutive equation. For this, an some assumptions are required to draw equation. Second, the model is created after the FEA program is developed from the constitutive equation. The FEA is responsible to compute the stress-strain values as prediction and then returns the simulated stress values for the selected condition. Third, the results from FEA will be used to create a model predicting the number of cycles to failure, N_f . Fourth, verifying FEA results with experiment.

2.6.1 Types of solder joint fatigue models

Most fatigue models were constructed from experiments such as thermal and mechanical cycling. In the past, several life prediction methods have been proposed to study solder joint fatigue. Among the existing approaches: (i) plastic strain-based; (ii) creep strain-based; and (iii) energy-based, constructed based on the fundamental mechanism that is possible to initiate and induce damage. The stress-based approach is classified as the force is applied to a component that produces strain as a result. Literally, there is still a heated discussion on suitable and an accurate fatigue models to predict life span of solder joint. Up to this point, there is no single model, though plastic strain-based model (Coffin-Manson) is among the popular method.

2.6.1.1 Plastic Strain Approach

The Coffin-Manson equation is a plastic strain based method for low cyclic fatigue (Coffin et. al., 1954). The method is used widely for life prediction of solder alloys subjected to deformation dominated by shear strain (Solomon, 1994). The prediction was made by calculation or experimental determination of the applied plastic shear strain.

The Coffin-Manson (CM) equation calculates the number of cycles to failure (N_f):

$$N_f = \theta (\Delta\gamma_p)^{-\Phi} \quad \text{Eq (2.1)}$$

where the calculation rely on the input from $\Delta\gamma_p$ is plastic strain range, while Φ and θ are material constants. For solder joints, Φ and θ are 1.3 and 1.9, respectively (Solomon, 1986). The plastic strain-based fatigue models require geometry data from experiment or FEA to calculate the fatigue life. The CM formulation is specific for plastic deformation and hence is inadequate for thermal fatigue prediction at solder joint. Which for this, it has relation to the time depend creep deformation.

2.6.1.2 Creep Strain Approach

Creep strain-based approach is closely related to the creep deformation at solder joints. For solder joints, normally creep is due to grain boundary sliding and/or matrix dislocation. Knecht and Fox (1991) have proposed a simple matrix creep fatigue model relating the solder microstructure and matrix creep (Knecht, 1991). The creep mechanism due to grain boundary sliding is incorporated with matrix creep into fatigue model by Syed (1996). In this model, creep strain is partitioned into two parts as,

$$N_f = ([0.022D_{gbs}] + [0.063D_{mc}])^{-1} \quad \text{Eq (2.2)}$$

where D_{gbs} is the accumulated equivalent creep strain per cycle for grain boundary sliding and D_{mc} is the matrix creep. It has been reported by Syed (1998) that the fatigue lifetime of solder joint is caused by a complex number of parameters. The possible parameters were dwell and hold times, ramp rate, top and bottom temperature extremes. However, the limitation of the creep based models is that it excludes plastic strain effects. Normally, plastic strain effects could only be neglected if strain rate is too low which cause a constant stress.

2.6.1.3 Energy-based Approach

In general, there is similarity between this method and CM, in terms of inelastic hysteresis energy density, W^I , and the equation is written as follows,

$$N_f = C^E (W^I)^{-\delta} \quad \text{Eq. (2.3)}$$

where δ and C^E is the material constants. The unit of W^I is mm-N/mm³ for calculation convenience.

In each cycle, the total strain energy density consists of the elastic, plastic, and creep strain energy density. The relationship of each component of the energy density with

fatigue life follows Eq. (2.3). Total creep fatigue damage then follows the Miner's linear superposition rule.

The energy density-based approach is convenient for the life prediction of thermal fatigue. The energy approach does have its technical merit for 3D deformation states (Dasgupta et al., 1992). In fact, the ranges of inelastic Mises strain and inelastic energy density are the only two parameters needed for thermal fatigue life prediction of solder joints, based on FEA.

2.6.2 Viscoplastic constitutive model

Previous section has briefly discussed on the history of life prediction of materials and their governing numerical calculations. Tin based leadfree solder alloys are known for its viscoplastic characteristic (Amalu & Ekere, 2016; J.-W. Kim & Jung, 2006; Mustafa, Suhling, & Lall, 2016; Qin, Zhang, Zhou, Li, & Mai, 2015; Tamin, Nor, & Loh, 2010). This implies that the material has a rate-dependent inelastic behavior of solids. Rate-dependence in this context means that the deformation of the material depends on the rate at which loads are applied.

The selection of a suitable constitutive model is important for an accurate prediction on the stress-strain response of the solder joint. Considering the impact of temperature and strain rate dependency of the solder alloy, the viscoplastic constitutive model, the creep or the fatigue model is possible to be employed by the FEA. Various constitutive models have been coded in commercial FEA software. Among the models are the Anand (1985), Johnson-Cook (1985) and also the creep models, including hyperbolic sine and Arrhenius equations. The most challenging part of employing numerical simulation is due to the difficulty in realistically copying the physical phenomena. These include modeling the various effects of microstructure features, the long-term response that

causes materials degradation and the property relationship between processing and the. This subsection will presents the existing effort on simulating the solder/substrate joint strength using FEA.

Kim and Jung (2006) used a 2D non-linear finite element analysis of an elastic-viscoplastic constitutive model to evaluate the effect of shear height and shear speed. ANSYS was used to analyze the solder ball joints. Analytical stress and averaged equivalent plastic strain analyses were performed to interpret the failure mechanisms. The shear ram was considered as a rigid body and scale factor of effective thickness was calculated and applied for getting the shear force as this work used 2D model. The surface-to-surface target element (TARGE169) and the contact element (CONTA172) were employed to simulate the contact between the shear ram and the solder ball. Figure 2.17 shows the constructed 2D model. This creep option was combined with the Multilinear Isotropic (MISO) hardening using von Mises plasticity to represent the viscoplastic properties of the solder material. The linear elastic material properties used are the Young's modulus (E), poisson ratio (ν) and density. While the steady state creep constants are the pre-exponential factor (A), the stress level at which the power law dependence breaks down (α), the activation energy (Q), the gas constant (R) and the strain rate sensitivity of stress (m). These steady state creep constants were those converted from the Anand model constants (Amagai et al., 2002; Lau, 1995). The governing equation for the implicit creep model in ANSYS is as shown in Eq. (2.4). The study concluded that if the IMC layer between the solder and pad metallization is too thick, brittle interfacial failure can be more easily achieved under conditions with lower shear height and that ball shear mode is also closely related to the region of high von Mises stress contours. This is due to simulation result that the strain is very densely accumulated in the right above the Ni layer for samples with a shear height of 10 μm , while the strain is spread out in the upper region of the solder for samples with a higher shear height.

$$\frac{d\varepsilon_p}{dt} = A \exp\left(-\frac{Q}{RT}\right) [\sinh(\alpha\sigma)]^{\frac{1}{m}} \quad \text{Eq. (2.4)}$$

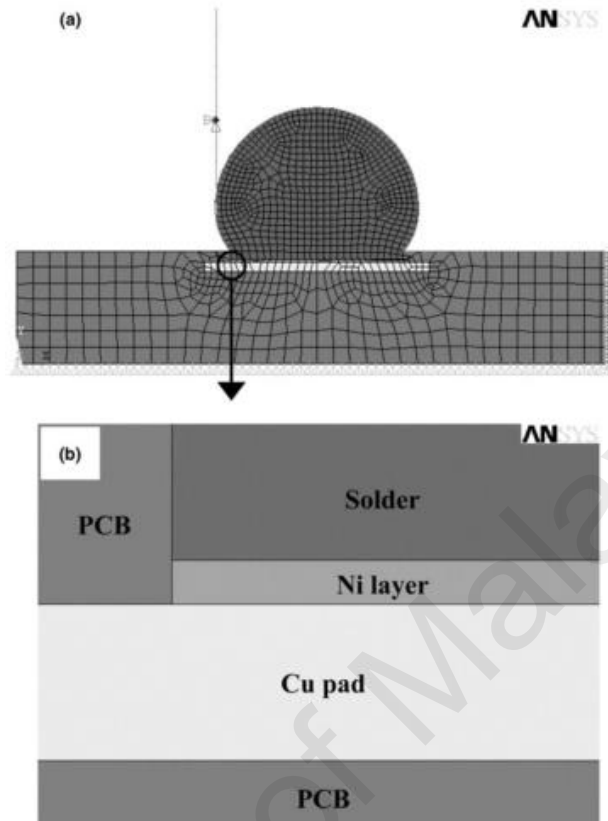


Figure 2.17: Solder/cu 2-dimensional model in ANSYS (Kim and Jung (2006))

Similar study was also carried out on other solder alloy, such as SAC305 (Qin et al., 2015). The study was trying to extract the magnitude and distribution of stress, strain and strain energy inside the solder of the joints due to limitation in experiments. The IMC layer was assumed as identical to the planar Cu_6Sn_5 layer (Li et al., 2013), with 5 μm thickness. Linear elastic material properties were used for the SAC305 solder alloy, copper, solder mask layer, substrate material and IMC (Cu_6Sn_5) (Chromik et al., 2003; Ma et al., 2009). The Anand model is used as the material constitutive model for the viscoplastic SAC305 solder in FE simulation (Anand et al., 1985; Brown et al., 1989). The element type of the viscoplastic SAC305 solder was selected as element VISCO107, and the rest was SOLID185. All elements in the FE models are 8-node hexahedron elements. The average mesh density of solder in all FE models is fixed at $3.6 \times 10^4 \text{ mm}^3$. Figure 2.8 displays a half

symmetric FE model of a solder joint with $h = 300 \text{ } \mu\text{m}$. The study concluded that although FE simulation results indicate that the shear strength of solder joints increases with decreasing standoff height, the experimental shear strength data of the micro-scale joints show a parabolic trend with the standoff height. Additionally the Von mises stress distribution and plastic strain energy density in the solder of BGA joints with different h under a shear stress of 22.10 MPa (Qin et al., 2015) proven that the maximum equivalent stress decreases with decreasing h under the same shear stress. Thus, according to the von Mises criterion in plasticity theory by Hosford (2005), solder joints of smaller dimension solder ball may have higher shear strength.

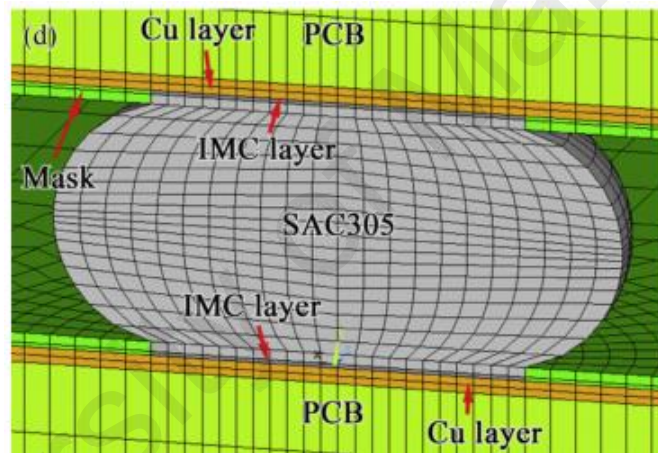


Figure 2.18: A half symmetric FE model of BGA solder joint (Qin et al., 2015)

2.7 Summary

Researchers have used various methods to comprehensively study the character of lead-free solders. The vital role of the solder alloy as an electrical, mechanical and heated dissipation channel appears to be a common research theme. Both the correlated microstructure and the nature of the intermetal within it play important roles in demonstrating a good or bad solder alloy. Given the emphasis on eradicating Pb from electronic components and devices, Sn-Pb alloy can no longer be used as a solder material. Aggressive research on Pb-free solder alloys has been conducted. Earlier studies have focused very closely on the Sn-Ag-Cu ternary alloy, which offers superior mechanical properties compared to Pb-bearing alloys. However, the use of silver (Ag) in this alloy increases the total cost of mass production. The near-eutectic SAC105-Fe/Al has also been suggested as a promising lead-free substitution candidate for low-Ag SAC solder alloys among other suggested fourth element for alloying.

In addition to the selection of a good solder material, a suitable solder deposition technique is required to cost-effectively mass-produce the alloy of interest. The recent trend in the electronics world is towards miniaturization, lightweight, and multifunctional products. Accordingly, the encapsulation of maximum interconnections in minimum space is required. The bridging instantaneous connection between leads soldered on the Cu pad can cause shorts and other detrimental issues. Thus, this study was performed on the impact of humidity or trapped corrosive ions on the possible corrosion behaviour of the material. This study addresses the inherent reactive property of Fe/Al as an alloying element in SAC105 solder alloy.

In addition to the development of corrosion behaviour, solder ball shear properties of the soldered joints needed considerable focus. Solder joints are subjected to thermal and mechanical loading during service. Solder ball shear tests are widely used to investigate the shear, creep and thermal fatigue behaviour of solder joints because the deformation mode

simulates the real-life loading of the interconnections. Intermetallic compounds formed at the solder/substrate interface can have a substantial effect on the strength and fracture mode of the solder joints. To better understand the shear and deformation behaviour of SAC105-Fe/Al/Cu solder joints, the interrelationships between IMC formation, shear strength and the fracture mode of the solder joints are of great interest.

Because of the high cost of experimental work, simulation has always been an option to extend the study, provided the material property is given. There has been research on SAC105 since 2008 (Heshall et al., 2008). Through the years, the material properties of SAC105 have been extracted from experiments. Utilizing the simulation approach, studies could be extended to conduct many more assessments of the loading conditions and dimensions of the structure being assessed. This study will eventually predict the impact of solder ball size reduction on the strength of the adhesion on the Cu pad. The model will utilize a model whose stress-strain input is obtained from the experiment.

CHAPTER 3 : METHODOLOGY

This chapter describes the materials, equipment, experimental procedures and simulation steps used in this study. Figure 3.1 is a flowchart that summarizes all the methodologies of the experiment. In general, the methodologies can be divided into the following five major stages:

- i. Solder alloy and test samples preparation;
- ii. Microstructural, elemental, and structural characterization of the as-prepared samples;
- iii. Simulation of the possible threat of humidity to the assembled joint using a salt spray chamber;
- iv. The assessment of the associated potential and current of the solders immersed in 5 wt% NaCl solution; and
- v. The assessment of joint strength using a solder ball/Cu substrate shearing test.

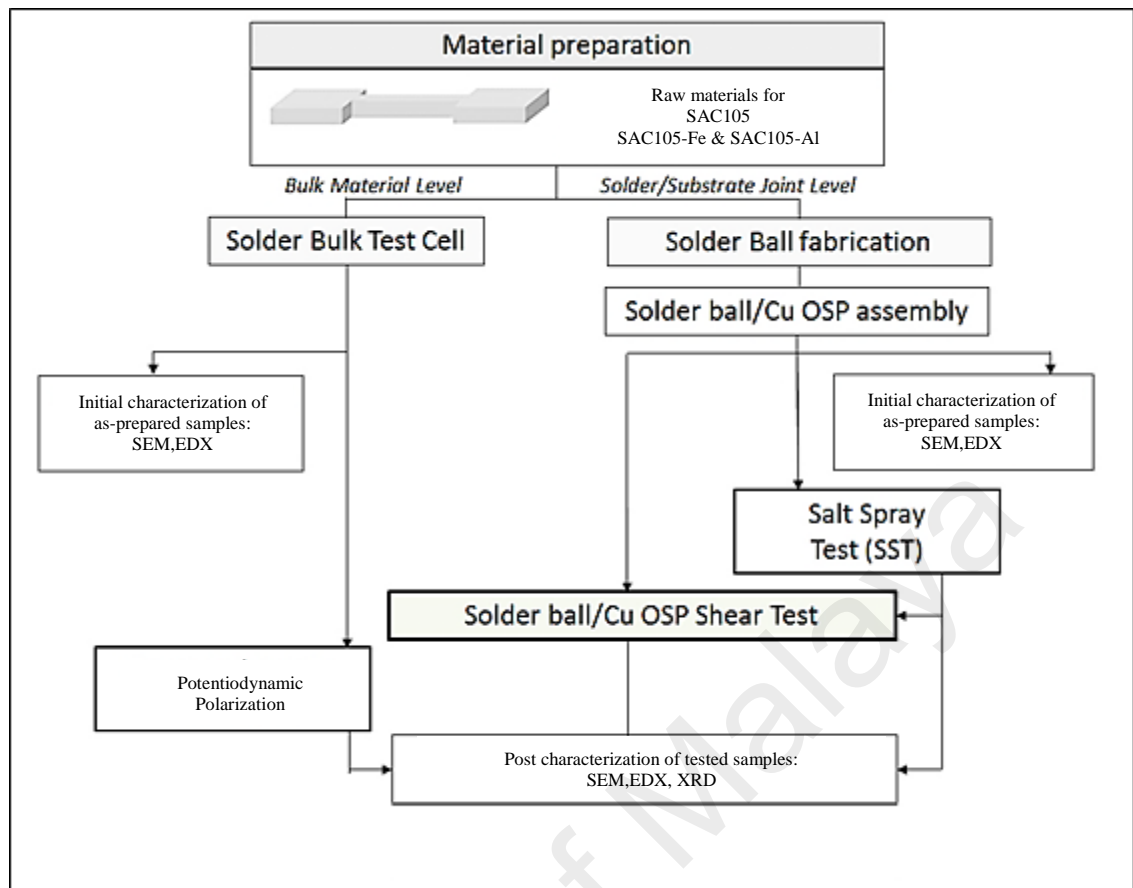


Figure 3.1 Overall flow chart of the material preparation, experimental procedures and post-processing of results

3.1 Material preparation

The study employed an assembled solder/Cu OSP substrate specimen for the solder ball shear and salt spray test, but a test cell specimen for the potentiodynamic polarization test.

The material compositions used in the study are as listed in Table 3.1.

Table 3.1 Chemical composition of solder materials

	Sn (wt%)	Ag(wt%)	Cu(wt%)	Fe(wt%)	Al (wt%)
SAC105	98.5	1.0	0.5	-	-
SAC105-0.1Fe	98.4	1.0	0.5	0.1	-
SAC105-0.3Fe	98.2	1.0	0.5	0.3	-
SAC105-0.5Fe	98.0	1.0	0.5	0.5	-
SAC105-0.2Al	98.3	1.0	0.5	-	0.2
SAC105-0.5Al	98.0	1.0	0.5	-	0.5
SAC105-1.0Al	97.5	1.0	0.5	-	1.0

The alloys were prepared by melting pure ingots of Sn, Ag, Cu and Fe/Al in an induction furnace at 1500 °C for 40 min. Then, the molten alloys were poured into preheated aluminium alloy moulds at 120 °C to 200 °C; the moulds were naturally air-cooled to room temperature. Finally, the moulds were disassembled and the bulk samples were removed and element compositional analysis was performed using EPMA. Figure 3.2 shows the solder alloy in a dog-bone shape. This alloy is the raw material used to form all types of specimens for all of the experiments used in the study. There are two types of specimens: solder ball and solder cubic cell.

There are a few precautions which need to be taken during the solder spheres fabrication process to ensure high quality of samples produced. A constant gas pressure (10bar) was used to force the molten solder flow through the tip, the speed of the magnetic stirrer was set to 50rpm and a collector was filled with resin flux to coat the spheres from react with air. The fabrication managed to consistently produce 1.2mm solder balls.

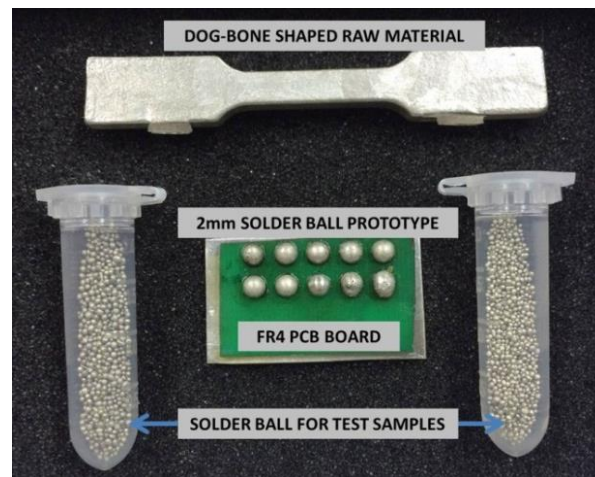


Figure 3.2 Forms of solder alloys used throughout the study

3.1.1 Solder/substrate assembly and salt spray test

The study is divided into two stages that involved material preparation before the experiment and a post-processing of the experimental data for an analysis of the results. During the first stage, material preparation occurred when the solder balls and solder cubic cell were prepared and fabricated.

A portion of the dog-bone shape SAC105, SAC105-xFe and SAC105-xAl solder alloys mentioned in Figure 3.1 is positioned in a solder ball fabrication syringe. The controller attached to the band heater is set to 245 °C. Once that temperature has been achieved, a syringe air pump is activated. At this point, the solder has melted completely. Pressure from the syringe pump will force the molten solder to be pumped out through the tip. The produced solder balls are collected and put through a sieve with a 1.2 mm opening diameter. The diagram of the syringe pump is displayed in Figure 3.3. The selected solder balls are later cleaned with acetone, allowed to dry and stored in a separate canister for each alloy composition. To prevent oxidation of the developing spheres, this formation process is performed under a nitrogen flow.

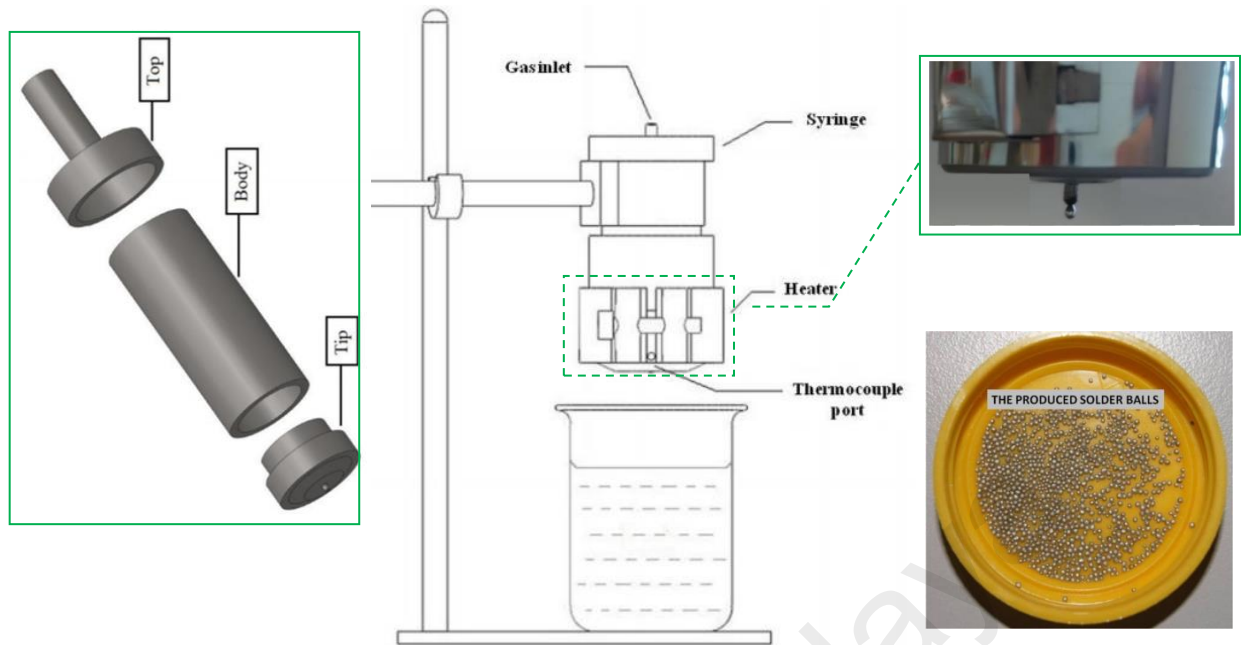


Figure 3.3 Solder ball fabrication using a metal syringe

Following the fabrication of solder balls, the solder balls are assembled on fire retardant (FR4) PCB boards. Each sample board mounts only one solder alloy composition. The complete experiment consists of 7 solder alloy compositions, all of which are listed in Table 3.1. The board was designed to have a 1.0 mm solder mask defined (SMD) copper pad opening for soldering of a 1.2 mm diameter solder ball. The surface finish for each copper pad is covered with organic solderability preservatives (OSP). Once the solder balls are aligned on each pad, all of the sample boards are placed in the oven to undergo reflow soldering. The temperature will slowly increase: the peak temperature is set at 275 °C for 15 seconds, approximately 50 °C higher than the melting temperature of the solder alloy used in this study. This is because the PID sensor between sensor on the board (sensor A) and the sensor near the heater (sensor B) has a difference of approximately 30 °C in temperature and the reflow oven is heating based on the reading by sensor B. A higher peak temperature than melting is set to allow the solder to reach its melting temperature, soak and completely solder the pad. The assembled sample boards are kept in the dry

cabinet, ready for testing. The finished samples to be sent forward for the salt spray test are shown in Figure 3.4.



Figure 3.4 Test boards for salt spray test

3.1.2 Test cells for potentiodynamic polarization test

The potentiodynamic polarization test is a type of corrosion behaviour assessment for materials. The test requires a known area of sample to be exposed and submerged in a desired aqueous solution. Care must be taken when preparing the sample so that the connected electrode is above solution level. For each composition, a 5 mm x 5 mm x 5 mm sample dimension was cut from the master alloy. To provide electrical connections, these cubic samples are separately attached to a Cu sheet 5 mm x 20 mm in diameter. The samples are then cold-mounted with an epoxy resin prior to being positioned in the standard 3 electrodes potentiodynamic polarization measurement setup. All of the mounted samples were ground, polished, and cleaned with water to obtain a mirror finish. The corrosion morphology of the candidate alloys after polarization tests was analysed using table top FESEM. Figure 3.5 shows the diagram of the preparation of the test cell.

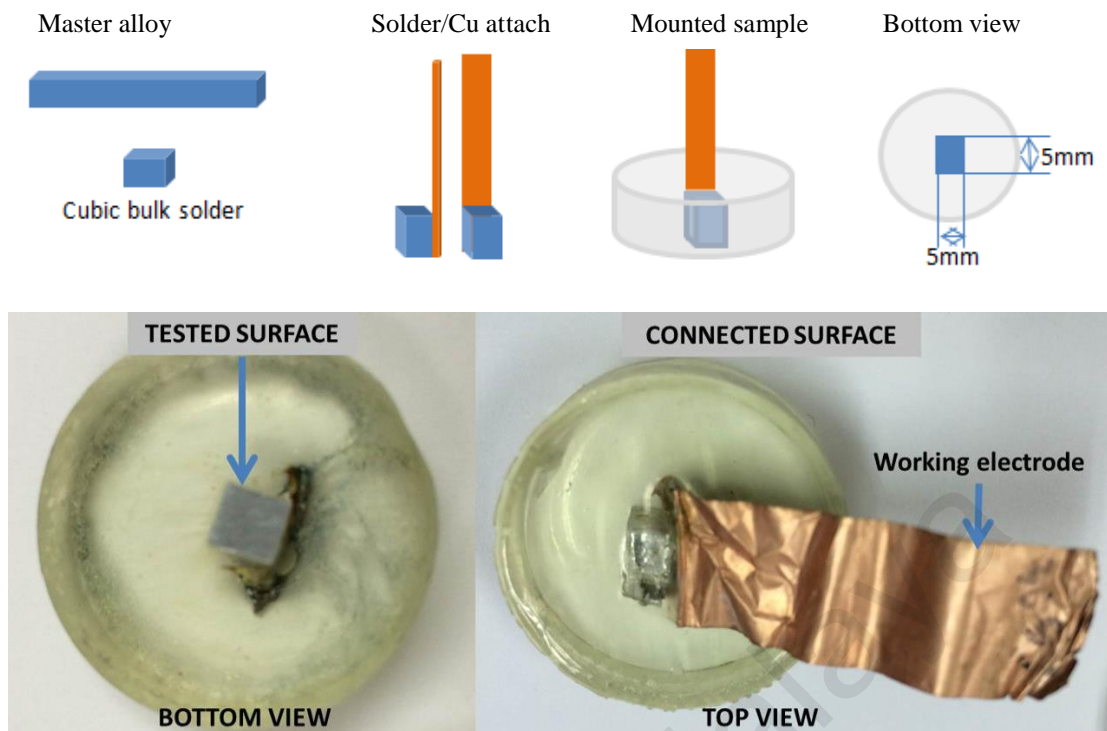


Figure 3.5 Sample preparation for potentiodynamic polarization

3.2 Assessments and characterization

3.2.1 Solder ball shear test

The use of the ball shear test method to assess the integrity of the solder ball bond is typically limited to quasi-static conditions, where the applied shear rate ranges from 0.6 mm/min (0.01 mm/s) to 60 mm/min (1 mm/s) (Coyle et al., 2000; Kim et al., 2004; Huang et al., 2001). Recently, the need to use lead-free solder and the increased popularity of portable electronics devices such as mobile phones and PDAs have resulted in increased concern about solder interconnect integrity during impact handling, logistics and storage.

The Instron universal tester (model 3369) dual-column system is employed in this test. The sample board is positioned in the jig and later positioned in the bottom clamp of the tensile machine. A shearing ram is placed in the upper clamp of the tensile machine. A diagram of the setup is shown in Figure 3.6. The speed of the ram movement is set at 0.60 mm/min. Bluehill 2450 software is connected to the tensile machine to record all related

data and instantaneously plot the shear strength data. To account for repeatability and accuracy, the sample size for testing the shear strength of each solder alloy composition is set at 15 solder balls. An average of the recorded reading will be the final value taken. Fracture surfaces of all of the test samples are then taken to SEM for fracture mode characterization. The solder ball joint with shearing specification was correlated with the JEDEC (Joint Electronic Device Engineering Council) solder ball shear test specification, JESD22-B117. High-speed shear test experiments have been added into the new version of JEDEC, which is JESD22-B117A. The approval criteria of a solder joint for shear failure step modes are also given in the JESD22-B117A (2006).

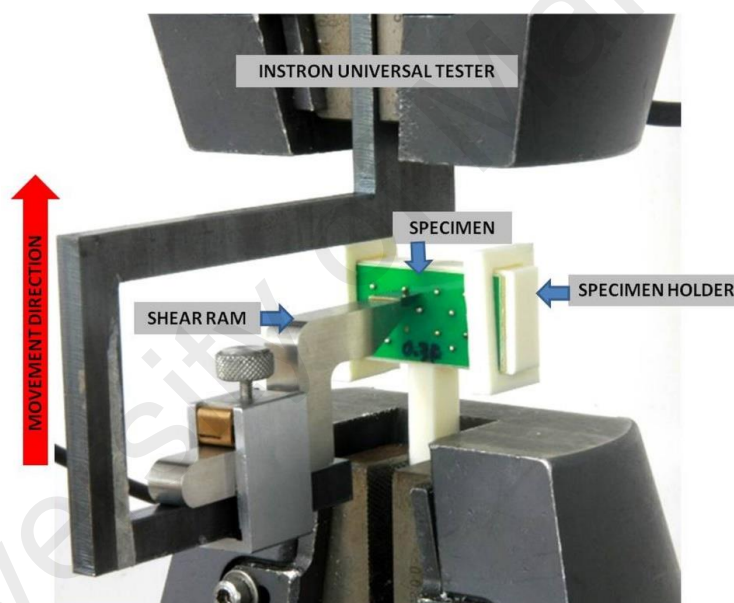


Figure 3.6 Solder ball shear test setup

3.2.2 Potentiodynamic Polarization Analysis

The Gamry Potentiostat Reference 600 was used to characterize the behaviour of all solder alloys tested in a 5 wt.% NaCl solution. The potentiodynamic polarization was performed at scan rates of 2.0 mV/s. A three-electrode electrochemical cell system, with the mounted sample as the working electrode with an exposure surface area of 0.25 cm², a platinum rod and SCE, were used as counter and reference electrodes, respectively, (Figure

3.7). The scan potential ranged from -2.0 V SCE to 2.0 V SCE. A General-purpose Electrochemical System was used as the interface software to calculate the corrosion rate using the following equation:

$$\text{Corrosion Rate, CR} = 3272 i_{\text{corr}} \frac{W}{AD} \quad (3.1)$$

where i_{corr} is the corrosion current (A), A is the surface area (cm²), W is the equivalent weight (g) (Table 3.2) and D is the density (g/cm³).

Table 3.2 List of material weight and corresponding density for each composition used in the test

		SAC105	With Fe addition (wt. %)			With Al addition (wt. %)		
			0.1	0.3	0.5	0.2	0.5	1.0
Equiv. Weight (gram)		59.642	59.512	59.252	58.994	59.238	58.641	57.672
Density (g/cm ³)		7.309	7.309	7.310	7.312	7.284	7.247	7.187

The samples are then subject to a cycle of phase, microstructural, and elemental analyses to determine the evolution after potentiodynamic polarization.

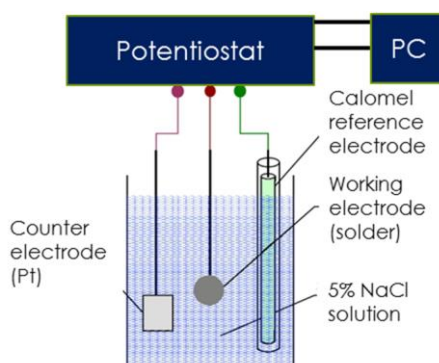


Figure 3.7 Schematic diagram of the cell used in the potentiodynamic polarization

3.2.3 Salt Spray Test

The experiment was conducted in Reliability Laboratory, MIMOS and using a Votsch VSC 450 Salt Spray (480litre) chamber. Figure 3.8 shows the standard of procedure in mixing the salt for the experiment performs in this lab prepared by Mimos Reliability Laboratory. The facility adheres to JESD22-A107C Salt Atmosphere assessment by JEDEC.

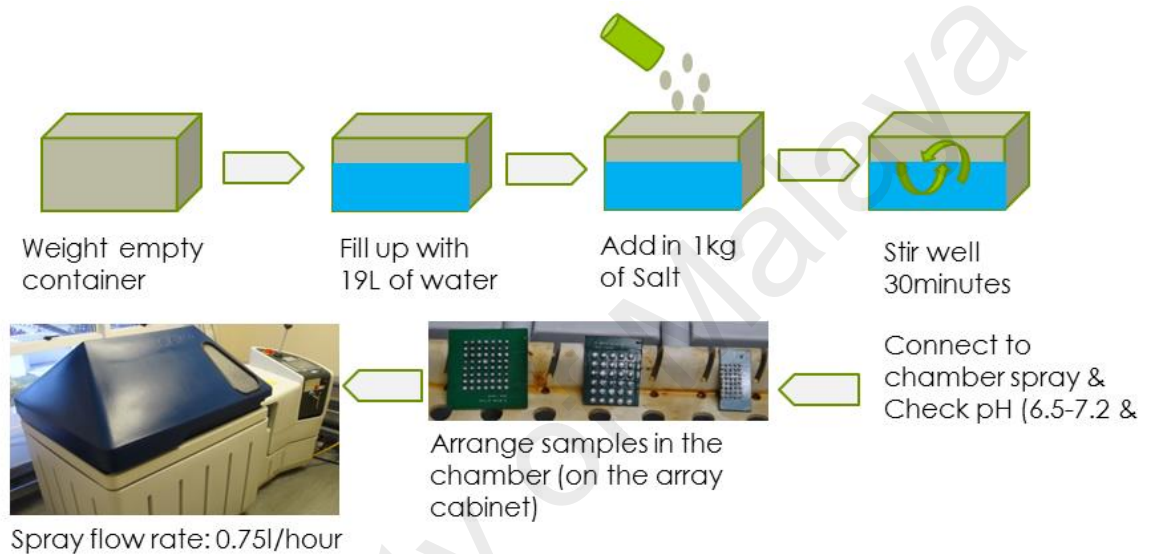


Figure 3.8 Standard of procedure in mixing the 5% NaCl saline solution

The assembled solder/Cu OSP FR4 boards were positioned in the salt spray chamber. Three sets of boards for each composition are prepared in which two of it is for the examination of salt deposit after 24hours and 96hours while the other one is assign as control sample at 0 hour condition. Examination of results involve inspection of surface degradation between solder composition at different hour of exposure to the salt mist, cross section of samples to investigate the impact of exposure towards intermetallic growth and also at the solder/substrate joint. The salt spray test chamber used for the salt exposure is as displayed in Figure 3.9.



Figure 3.9 The salt spray test chamber in Reliability Laboratory, MIMOS.

3.2.4 Microstructural, elemental and structural characterization of solders

The mounted specimens are subject to preliminary characterization procedure. To determine the phases formed, XRD was performed using a Bruker AXS D9 diffractometer at 2θ values between angle 10° to 90° . The radiation is generated by $\text{Cu K}\alpha$. The X-ray tube is supplied by a 40 kV voltage and a 30 mA current. The software, EVA is used to scan and auto-match the corresponding peaks of interest with the standards from the International Committee of Diffraction Data (ICDD) X-ray data file to filter the data from noise.

The microstructures of all samples pre and after test are analysed using a Phenom table-top SEM and FESEM. Meanwhile, the specific elemental properties were analysed using an energy-dispersive X-ray (EDX) spectrometer which is attached to a FESEM (Zeiss Supra 35 VP).

An Olympus BX51 optical microscope (OM) was also used to analyze the material surface, measure the IMC layer at solder-substrate joint and also to inspect smoothness of the surface prior to start the potentiodynamic polarization test and FESEM micrograph analysis.

3.3 Simulation

In the experiment part, only 1.2mm solder ball diameter solder balls were used for shear test. In practical, the dimension of solder ball use is far smaller. Due to limitation in laboratory facility and reliable materials fabrication, further shear test on smaller solder balls are not performed. On the other hand, it is impossible to investigate qualitatively on the mechanism occurring to the structure when the dimension is too fine. Hence, FEA is the right option to proceed with the effort to predict on the impact of miniaturization on solder joint strength.

There are a few steps required before simulation can run. Once physical assessment of interest has been identified, pre-processing shall start. At this stage, the geometry structure is sketch, material and loading type are selected, boundary conditions are set and contact behavior is determined. Figure 3.10 shows the graphical breakdown of the process to simulate a system. The accuracy of the model depends on the meshing arrangement and validity of the calculated result is proven by the magnitude of the simulated shear strength.

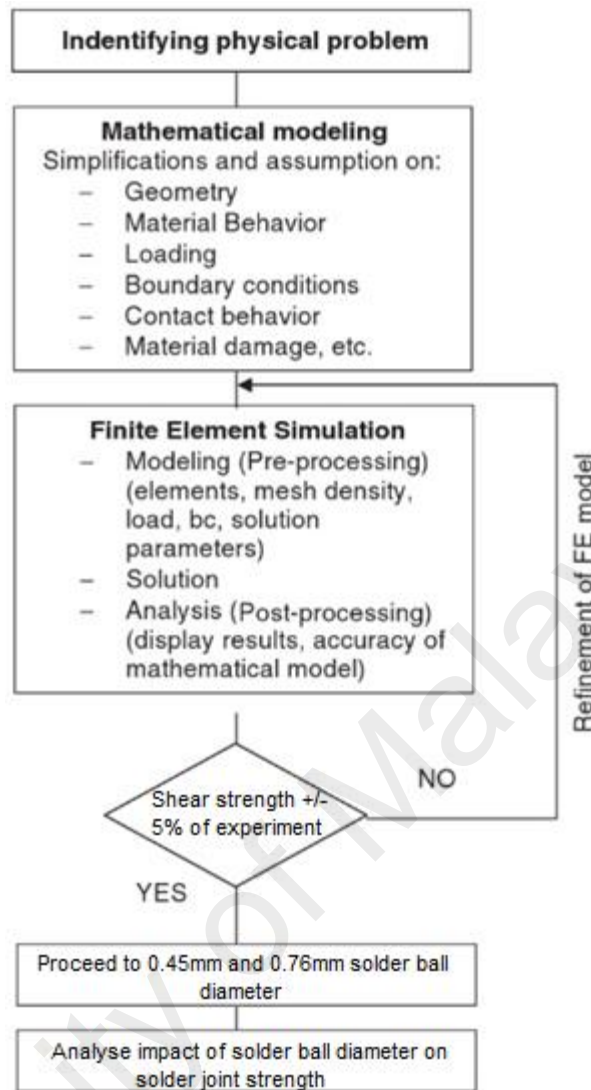


Figure 3.10 Process flow of problem solving by finite element simulation

3.3.1 Element type

SOLID186 is a higher order 3-D 20-node solid element that exhibits quadratic displacement behavior. The element is defined by 20 nodes having three degrees of freedom per node: translations in the nodal x, y, and z directions. The element supports plasticity, hyperelasticity, creep, stress stiffening, large deflection, and large strain capabilities. It also has mixed formulation capability for simulating deformations of nearly incompressible elastoplastic materials, and fully incompressible hyperelastic materials. The SOLID186 element type is suitable to model irregular meshes produce by smartsize meshing control.

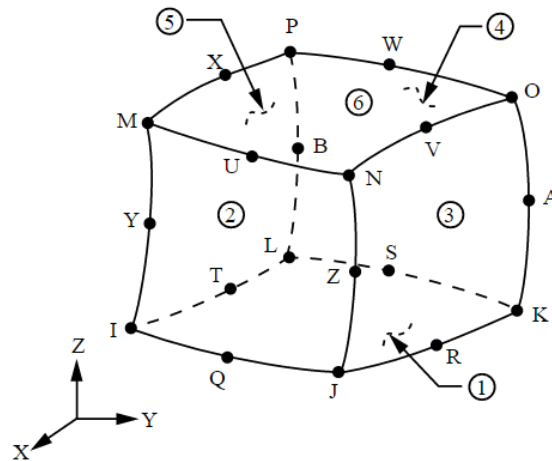


Figure 3.11: 20-nodes SOLID186 Structural Solid Geometry

The geometry, node locations, and the element coordinate system for this element are shown in Figure 3.11. The element coordinate system orientation is as described in Coordinate Systems. Element loads are described as a nodal loading. For the case of viscoelastic materials, the output of stress and strain is always with respect to the material/element coordinate system.

Element type CONTA174 is used to represent contact and sliding between 3-D target surfaces and a deformable surface defined by this element. The element is applicable to 3-D SOLID186 solid structural. For a shear ram/solder contact, the target surface is defined by CONTA174 elements (for deformable solder surfaces) or TARGE170 elements (for shear ram rigid body). Contact occurs when the element surface penetrates an associated target surface.

3.3.2 Material type and meshing

To simplify the calculation, the materials are assumed to be isotropic and thus all properties are independent of direction. There will only be two constant or variables to be considered. These constants represent the material's hardness and compliance and the constants are the Young's Modulus, E and the Poisson's ratio. Table 3.3 lists the constants for all materials used in the solid structure.

Table 3.3 Material Properties

Material	Young's Modulus, E (GPa)	Poisson ratio, ν	Density (kg/m³)
Copper Pad	128.70	0.40	8940
SAC105	32.50	0.34	8410
FR4	17.50	0.28	1200
Shear Ram	170.00	0.30	7750
Cu₆Sn₅ (IMC layer)	119.89	0.29	8260

Meshing for the whole structure was assign to be quadrilateral type and manually set. Area of interest is finer meshed while other supporting parts of the structure were coarsely meshed. This technique ensures reduction of timing use for calculation without compromising the validity of the calculated response at the area of interest. Quadrilateral, mapped and control mesh was chosen. Mesh controls were set prior to meshing the solid model. All these settings are accessible by using the chosen element type Solid 186. Meshing control for this structure was using smart sizing technique that ensures a better chance of creating reasonably shaped elements during automatic mesh generation. This feature provides a range of settings from coarse to finer meshing.

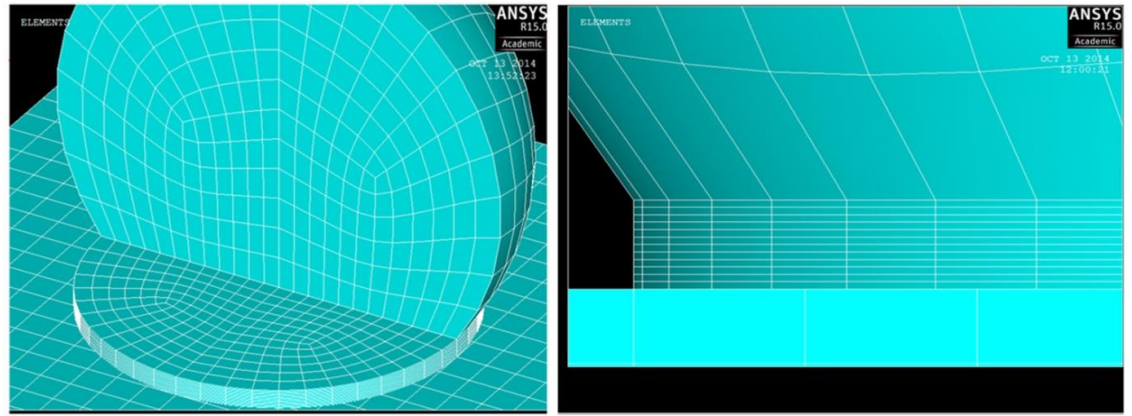


Figure 3.12 Meshing for continuous element divisions of solder ball, copper pad and FR4 board.

3.3.3 Load and boundary condition

For introducing load to the structure, it is imperative to initially create an area or a volume by moving it to the favourable place and adding it to the surface for impact test. The area or volume created represents the load source to the structure. Figure 3.13 displays the introduction of shear load, represents by the area in pink that touches the solder ball surface at node 96165.

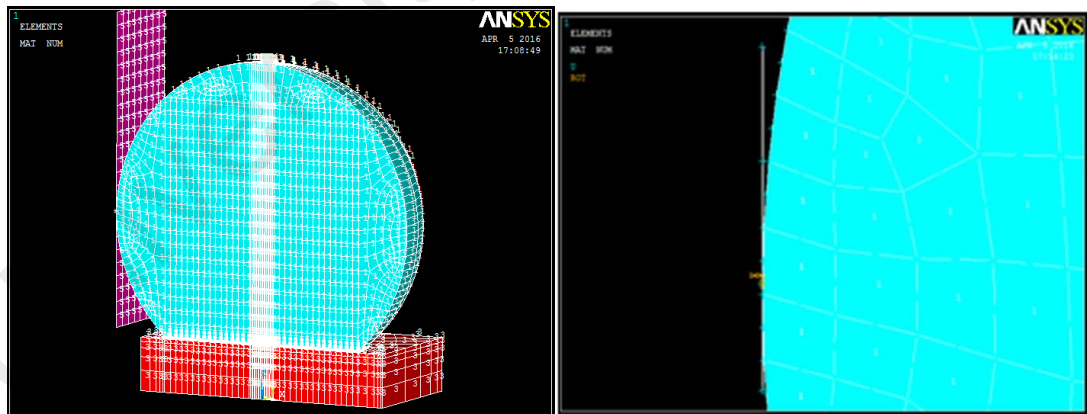


Figure 3.13: Shear load on the solder ball surface

Loading of solder joint was done by moving shear tool from left to right for a fixed distance at a specified constant speed. Solder ball sizes were varied in order to account for change in strength for individual cases. In this study, size of the solder balls was varied from 0.45mm, 0.76mm and 1.2mm.

When solder breaks the shear force monitored at the shear tool drops significantly. Shear force values were considered till after first fall in shear force. The mechanism is commonly represents by a stress-displacement curve as in Figure 3.14. The boundary conditions are set so that the structure's degree of freedom (DOF) is being controlled to impact only on X-axis while Y and Z-axis are fixed to zero DOF.

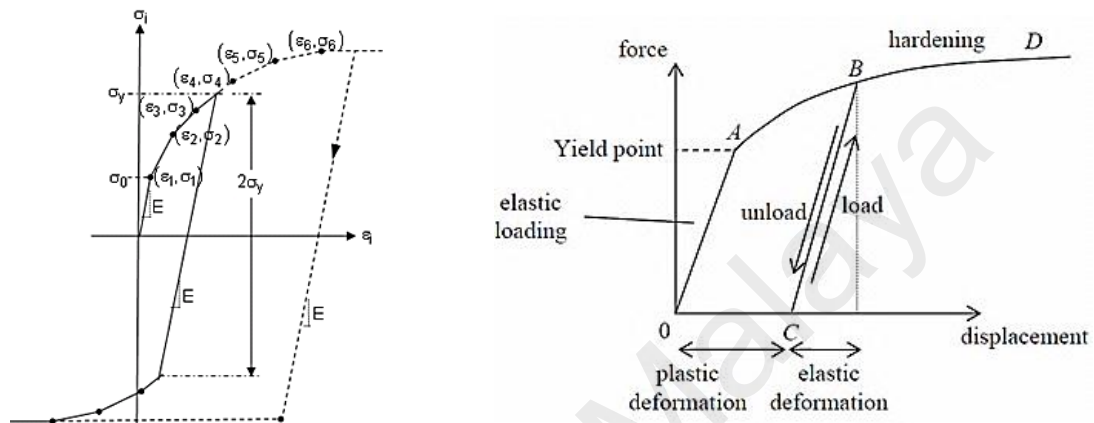


Figure 3.14 Stress vs. Total Strain for Multilinear Isotropic Hardening

3.3.4 Solver

ANSYS has a few equation built-in equation solvers for the selected model used. For a nonlinear structural analysis, iterative solver is the most suitable and several are available. Preconditioned Conjugate Gradient (PCG) solver employs a proprietary preconditioner. The solver is very efficient for structures that are hard to converge. It offers an element to element option which reduce memory requirement for calculation.

3.3.5 Post processor

To view the results of an analysis in order to understand how the applied loads affects the structure, POST 1 post processor is used. POST1 postprocessor presents the static or steady state problems. The POST1 enable the contour displays, deformed shapes,

nodal displacements, stress contour, von mises stresses, principal stresses etc. As these results are used to reflect the output of the simulation.

University of Malaya

CHAPTER 4 : SOLDER BALL FABRICATION AND BALL SHEAR BENCHMARK TEST

As discussed comprehensively in the literature review, one of the most effective methods of assessing the solder joint strength of a BGA chip is to conduct a joint stress test. This study has been planned and designed to perform a solder/substrate shear test. The material and apparatus are as described in Chapter 3. Prior to the experiment, the solder balls must be fabricated. The raw material is similar to that used in Phase I of the study on Fe/Al-added SAC105 (D.-A. Shnawah et al., 2012; D. A.-A. Shnawah et al., 2012a). The solder ball shear test is conducted using an Instron universal tester with a custom-made shear jig. This is not like the equipment used to obtain most published data. Therefore, this work will conduct a benchmark test against published data to validate the result from both its setup (Instron Universal) and the popular method (DAGE shear tester). The first part of this chapter will elaborate on the work of solder ball fabrication and the second part will present the outcome of the test apparatus benchmark experiment.

4.1 Solder ball fabrication

There are a few options for producing lead-free solder balls. One could start from powder or transform another solid form, such as a bar, wire or paste. This study is Phase II of the investigation into the potential of SAC105 with minor addition of Fe/Al. Thus, the work will start from the dog-bone shape bar used in Phase I. The first phase presented comprehensive data on the bulk material. Subsequently, this study will focus on the solder/substrate joint performance of the material, specifically the BGA soldering application. Therefore, the bulk material in Phase I must be transformed into solder ball spheres.

The methods used to fabricate solder balls include the nozzle ejector (Zenin et al., 2008; Hayes et al., 1993), wire reflow (Zenin et al., 2008), fabrication over a wafer (Tong et al., 2003), immersion in heated oil (Maslinda, Anasyida, & Nurulakmal, 2016) and metal droplet jetting (Q. Liu & Orme, 2001). This study will implement a method similar to the method used by Liu and Orme (2001), using the droplet method through a heated metal syringe.

4.1.1 The Apparatus

The chosen method is composed of 7 major parts: the metal syringe, band heater, the PID controller, the K-type sensor, the rosin-filled collector, the platform heater and the metal syringe holder. The band heater is attached to the lower body of the metal syringe, the closest area to the syringe tip. This is to ensure that the solder retains its liquidity while flowing through the tip and dropping into the heated collector. A K-type thermocouple is taped to the inner body of the syringe to give PID input into the controller. The controller controls the ramp-up heating of the band heater to reach the melting temperature of the solder alloy.

There were two fabrication stages. The first stage is the initial process, in which the experiment was unable to achieve reliable solder ball production. The second stage is after the optimization of the metal syringe design and including stirring in the heated collector. Figure 4.1a shows the initial arrangement of the experiment with a basic setup. The outcome of the produced solder droplets is shown in Figure 4.1b. The droplets are a mixture of non-uniform solder balls and numerous burst solid solders.

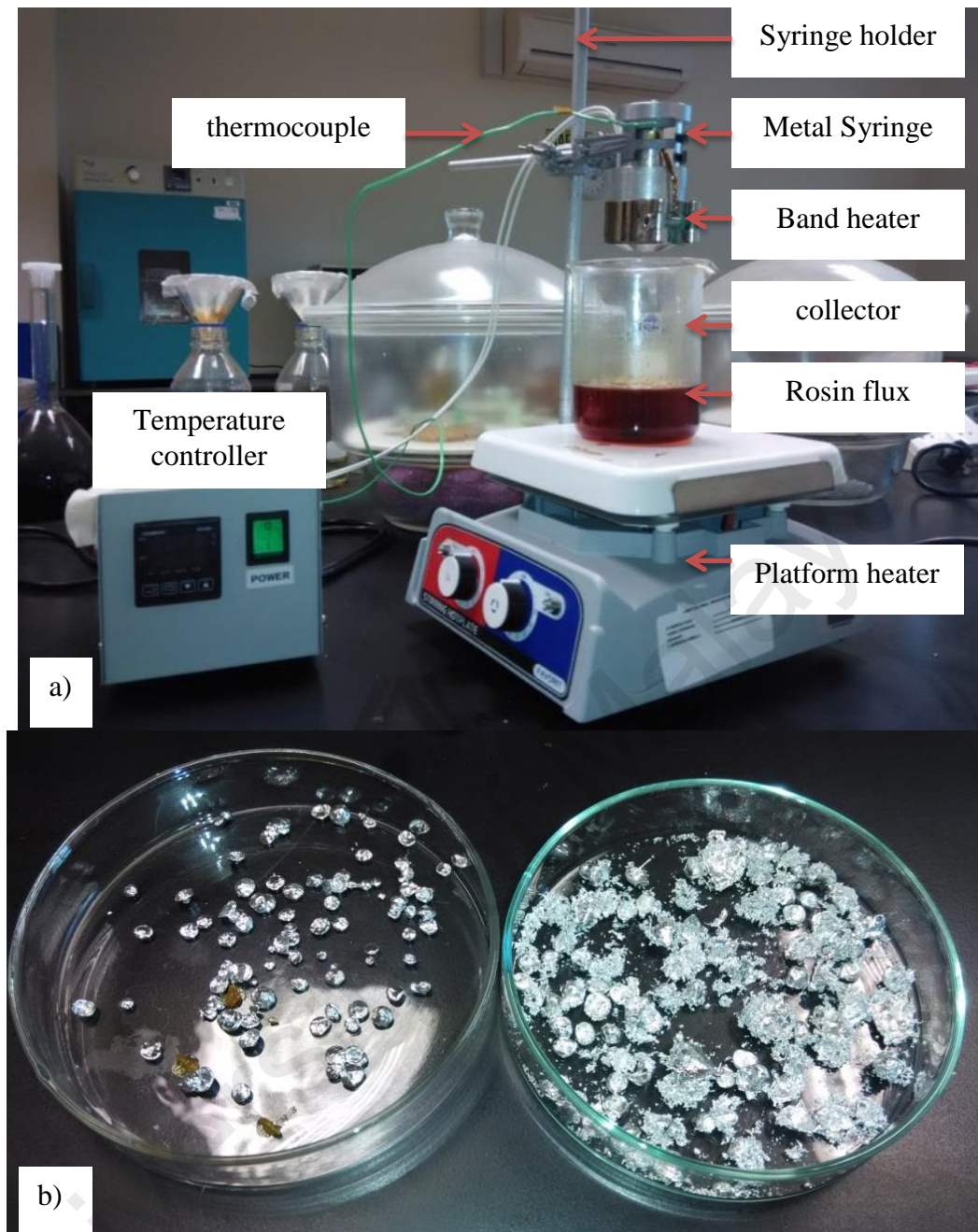


Figure 4.1: (a) Solder ball droplet method using a heated metal syringe (b) The fabricated droplets

The metal syringe is optimized by reducing the inner space to decrease the area volume and increase the air jetting force from the gas inlet to the syringe tip. This is done by reducing the total length of the syringe to 100 mm from 195 mm and the diameter to 10 mm from 40 mm. In addition, the tip's inner diameter is reduced to 0.30 mm from 0.50 mm. The alteration of the metal syringe is as shown in Figure 4.2a. A tremendous

reduction in space volume was effective in producing reliable solder balls. This is because the new syringe produces multi-dimensional solder spheres. These spheres were separated by their diameter using a sieve and the separated spheres are shown in Figure 4.2b.

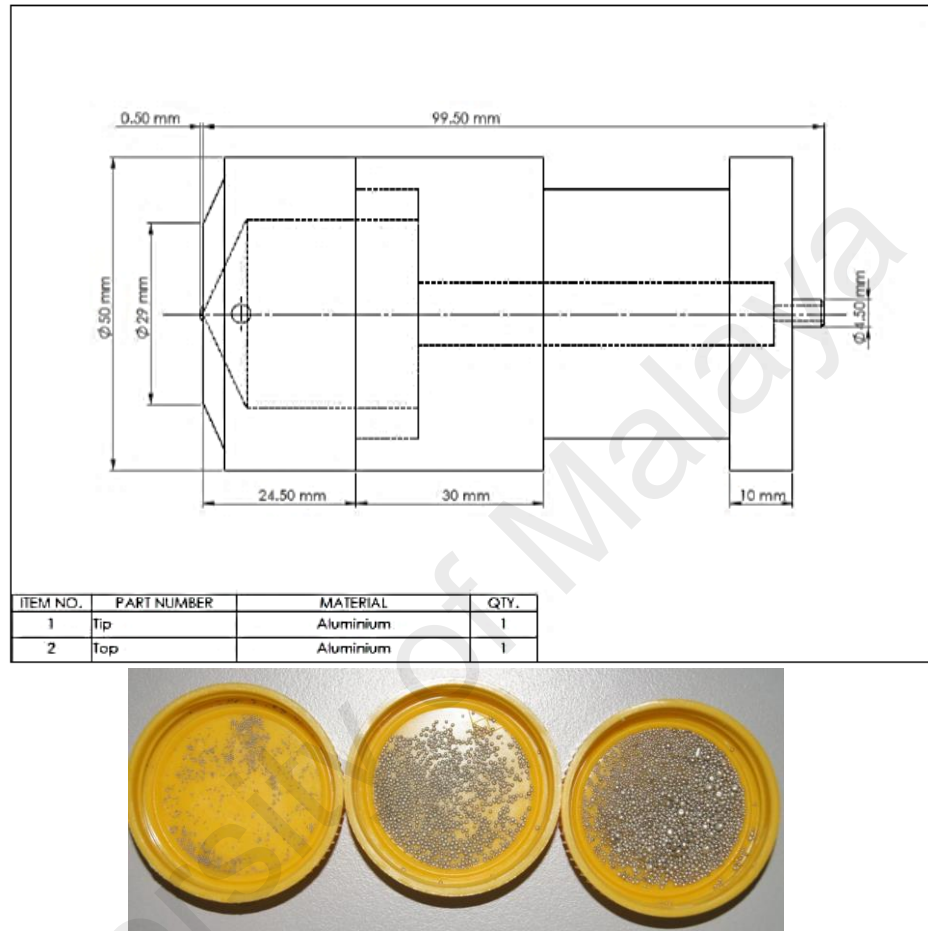


Figure 4.2: (a) Metal syringe after optimization of the design (b) Multi-dimensional solder balls.

Table 4.1 Approximation of solder balls produced in the experiment

	diameter\leq500 μm	500μm<diameter\leq1.5mm
Average diameter of majority solder balls (mm)	0.36	1.20
Volume of one solder ball, sphere (m³)	2.442×10^{-11}	90.5×10^{-11}
Density of solder (kg/m³)		7300
Mass of one solder ball (kg)	1.783×10^{-7}	6.606×10^{-7}
Mass of solder ball produce (kg)	0.312×10^{-4}	4.551×10^{-3}
Total number of solder ball produce (rounded off)	175	689

From this new setup, it was found that usable solder balls could be produced with this method. Based on the results, this experiment is capable of producing micro solder balls even below 500 μ m. By referring to Table 4.1, it was estimated that this experiment created more solder balls $>500 \mu$ m with the majority of the average has a diameter of 1.22mm, thus allowing ample specimens to start with the ball shear test and salt spray test.

4.2 Ball shear benchmark test

This solder ball shear test in this study uses an Instron Universal Tester with attached custom-made shear jig and shearing ram. To ensure that the setup is reliable in producing results that are comparable to other published data, this work has conducted a benchmark test. This pre-assessment aims to validate both the instrument and the resulting data. Therefore, lead-free solder materials, PCB and flux provided by Sujan et al. (2014) were used as the testing specimens, and a similar test arrangement was set up for the pre-assessment using the Instron Universal tester.

4.2.1 Shear strength of Ni-doped SAC305

Lead-free Sn-3.0Ag-0.5Cu (SAC305) solder balls of diameter 450 μm were used in this study. Nickel (Ni) nanoparticles (0.1wt.% Ni, Accumet Materials, Co., USA) with an average size of 44 nm were mixed with a commercially available water soluble flux (Sparkle Flux WF-6317, Japan) to prepare the 0.1wt.% Ni nanoparticle doped flux. The BGA printed circuit board (PCB) used in this study as the substrate had a double-sided polyimide solder mask with an opening diameter of 300 μm . The underlying Cu pads were 30 μm in thickness with OSP surface finishing at the opening end. Before reflow, the PCB substrates were dipped in 2-propanol solution (R & M Marketing, Essex, U.K.) for 120 s to clean the opening pads of the OSP surface finished substrates. Next, the substrates were rinsed with deionized water and dried in acetone. The 0.1wt% Ni nanoparticle doped flux was placed on the clean OSP-Cu substrate. Solder balls were then placed on top of the flux and reflowed in a reflow oven (Forced Convection, FT02) at 240 $^{\circ}\text{C}$ for 45 s. The ball shear test was performed using an Instron Universal tester as in Figure 3.6 using the methodology described in Chapter 3. The shear height and shear speed were set as 20 μm and 650 $\mu\text{m/s}$, respectively. Twenty solder bumps were considered for this experiment.

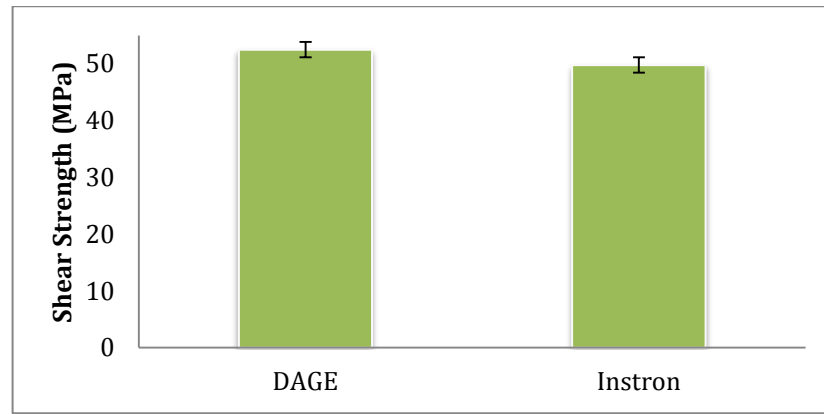


Figure 4.3: Comparison of shear strength of a 450 μm solder ball on Cu/OSP using a DAGE DT 4000 tester or an Instron Universal tester.

Figure 4.3 shows the ball shear strength of SAC305-0.1wt.% Ni as a function of the equipment used to test the solder joint. It is seen that the average shear strength of the Dage BT 4000 tester is marginally higher than that of the Instron Universal tester. The difference is because DAGE is an instrument design that is fabricated for conducting shear tests on small structure such as the IC chips. Therefore, the setup of shear speed, shear height, and displacement of the shear tool is built into the instrument, thus ensuring accuracy, reliable specimen handling and smoothness of the experiment. Conversely, the Instron Universal Tester needs to have an additional apparatus attached to it to perform the ball shear test. The external tools are the shear jig to hold the specimens and the shear ram to provide the shear load on the solder bumps. Additionally, the load referring to the compressive or tensile work of the machine and shear height is controlled by another external standoff layer to ensure 20 μm shearing height, similar to the setting applied by Sujan et al. (2014). Therefore, compared to the Dage DT 4000, the compartmentalized setup makes the procedure be more extensive and challenging to control of an exact displacement. However, a comparable outcome is achievable using this setup.

CHAPTER 5 : RESULTS AND DISCUSSION

Based on the literature review of minor element alloying in low Ag SAC lead-free solder alloy discussed in Chapter 2, this material has attracted continuous interest among both industrial and academic researchers. This implies that the material has some potential to be an important solder alloy. There are three main effects of fourth element addition to the ternary SAC solder alloy. First, fourth element addition alters the microstructure of the bulk and interface layers at the substrate. Second, there are obvious changes in mechanical properties of the material. Third, fourth element addition is found to control IMC layer thickness. Additionally, the effect of Fe or Al as the fourth element alloying on the corrosion behaviour of SAC105 solder has not yet been investigated. The types and workflow of assessments to assist the investigation were designed and discussed in Chapter 3. Therefore, this chapter is divided into four main subsections to present the outcome of the study extracted from the planned experiments. Sections 4.1, 4.2 and 4.3 will separately discuss the findings related to SAC105, SAC105-xFe and SAC105-xAl, respectively. In each of these subsections, the details of the results of the impact of Fe/Al addition to SAC105 pertaining to the control of the IMC layer at the substrate, strength of the solder joint and their corrosion behaviour are discussed. In the last section, Section 4.4, the numerical FEA results are presented and elaborated.

5.1 Sn-1Ag-0.5Cu

5.1.1 Surface morphology and microstructure

The as-reflow microstructure of the Sn-1Ag-0.5Cu (SAC105) solder alloy is shown in Figure 5.1. The microstructures consist of primary β -Sn dendrites and interdendritic regions consisting of Cu_6Sn_5 and Ag_3Sn IMC particles dispersed within the Sn-rich matrix. The particles of Cu_6Sn_5 are larger than those of Ag_3Sn , and the emerging pattern of these two particles within the matrix is easily characterized. The Ag_3Sn is not only smaller (approximately 0.10 to 0.70 μm) but also typically exists in groups, which are easily observed as dotted straight lines or dotted circles. This specific character is shown in Figure 5.1. Conversely, Cu_6Sn_5 exists singularly, without a specific pattern and with a dimension of approximately 0.40 to 3 μm .

It is established that compared to the primary β -Sn matrix, Cu_6Sn_5 and Ag_3Sn particles possess higher yield strength and elastic modulus (Kim, et al., 2007; Suh, et al., 2007). These differences in the core characteristics of the components in the solder matrix were attributed to their bonding. The IMC particles possess covalent bonds, whereas the β -Sn has metallic bonds. The metallic bonds enable the motion of the atoms without causing major disruptions that could alter mechanical integrity. This leads to the inherent ductile and malleable properties of Sn (Denga, et al., 2004; Kamal & Gouda, 2007).

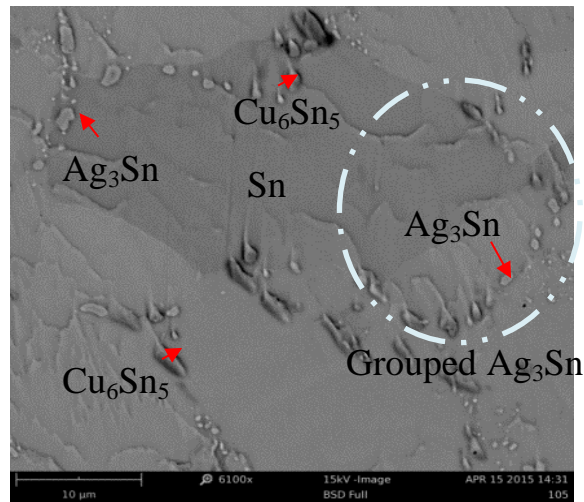


Figure 5.1 Surface microstructure of as-reflow SAC105

An optimized ratio of the elements that constitute within the solder alloy matrix would define the alloy's character. Ductility of solder alloy relies on the modulus of elasticity and the yield strength as reduction in both parameters will result in a soft and more ductile alloy. Both of these key properties eventually will increase if there are more addition of Cu_6Sn_5 and Ag_3Sn IMCs as the inclusion would create a stiffer alloy. As investigated in a multiple spot of the bulk SAC105 micro-section image, there are far fewer Cu_6Sn_5 IMC particles than there are Ag_3Sn . Thus, the dominant contributors to the mechanical property of SAC105 solder alloy are the primary β -Sn and the Ag_3Sn IMCs.

5.1.1.1 Surface morphology after Salt Spray test

The solder balls surface morphology changes of SAC105 after the salt spray test are shown in Figure 5.2. These images show that, as expected the corrosion after 96-hour exposure is more serious than the corrosion after 24-hour exposure. However, the impact of the 96-hour exposure is reduced tremendously after the samples were aged for 24 hours at 180 °C prior to exposure in the salt spray test. Evidently, ununiformed attack on the ball surface. The corrosion is confined to a few localized pits. It is apparent that after 24 hours of salt spray exposure, insignificant visual surface degradation was observed. In contrast, Figure 5.2c exhibits solder balls surface is largely covered with numerous pits. As in the result for

96 hours of salt spray samples, the pits merge, and the area of corrosion enlarge and penetrated deeper.

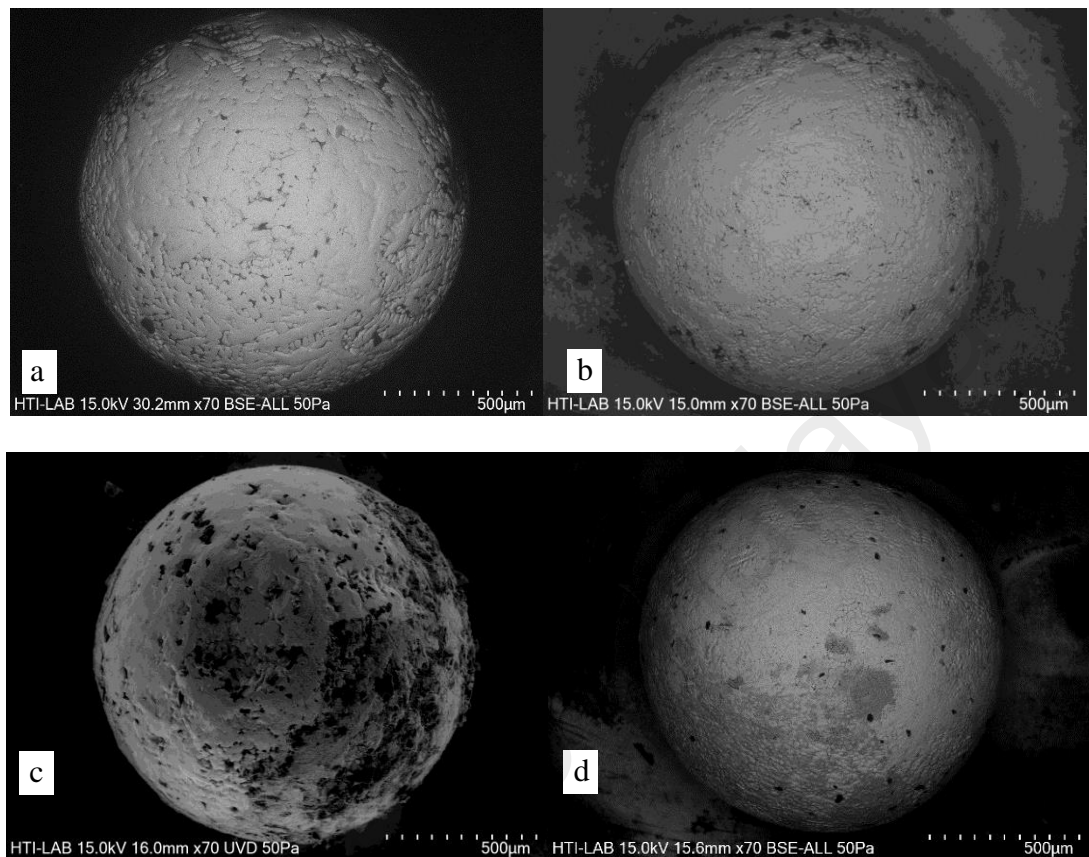


Figure 5.2: FESEM micrographs of (a) as-reflow SAC105 solder alloy and after salt spray (b) for 24 hr (c) for 96 hr (d) for 96 hr with 24 hr of ageing at 180 °C

Figure 5.3a depicts the corrosion mechanism that occurs. The suggested corrosion products found are derived from the XRD analysis performed on the surface after the samples were tested. The result is shown in Figure 5.3b. As also suggested in Figure 5.4, the surface was covered with corrosion products that consist of SnCl_2 , SnCl_4 , SnO and SnO_2 .

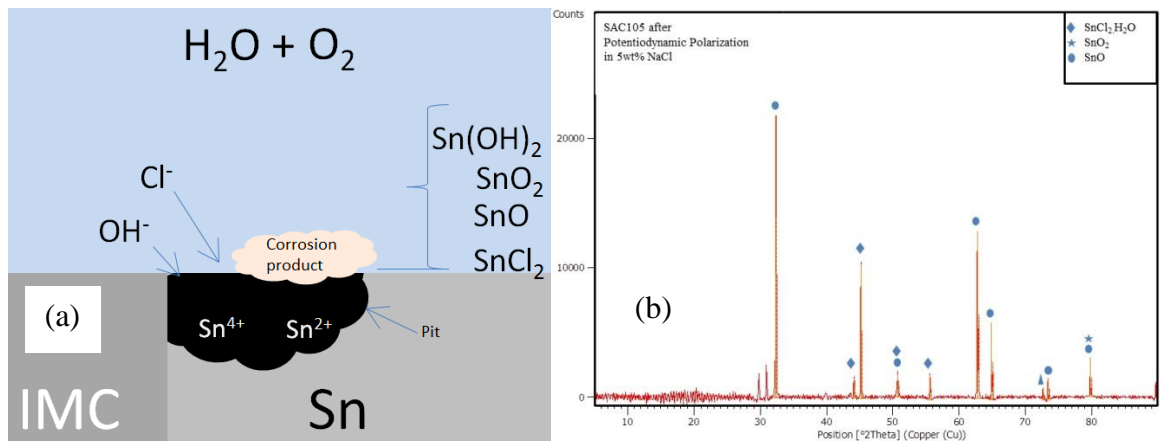


Figure 5.3: Corrosion mechanism caused by Cl^- and the formation of corrosion products on the material's surface


Through EDX analysis, further analysis of a specific spot on the surface showed that Cl^- was detected on the material surface after testing. This is because of the reaction of the elements within the solder alloy to the penetration of Cl^- . The EDX analysis detected Sn, O, C, Ag and Cl within the corrosion spot that was scanned. The atomic concentrations before and after the test measured by EDX are displayed in Table 5.1. After exposure to NaCl, the Sn content decreased by 20-30%, either because of the material falling off or because the β -Sn areas are effectively covered by corrosion products. The Ag content was detected in higher concentrations than before the test started. This indicates that the corrosion attacks tin, while the Ag remained within the solder bulk. The high content of Carbon, for scanning prior to exposure to salt spray could be assumed to be from surface preparation technique which left residues on the surface. Contaminants in the microscope vacuum can be deposited upon the surface of the specimen as carbon. Most commonly, carbon layer will spontaneously cover the surface and it is significant prior to corrosion test. As after corrosion test, the surface is completely covered by corrosion products consists of Sn, Cl, O which precede the detection of carbon by EDX.

Table 5.1 EDX analysis of solder ball surface after salt spray test

Element	0 hour	24 hour	96 hour
C K	31.79	20.63	25.72
O K	14.59	32.75	35.43
Sn L	59.52	47.62	40.72
Cu K	14.12	-	-
Ag L	2.35	8.98	19.48
Cl K		2.58	10.67

Pure Sn forms a protective oxide film but is not stable and easily reacts with chlorides because of the impact of differential galvanic series between the elements. The galvanic series is listed in Table 5.2. During the surface initial exposure to oxygen, Sn forms SnO. As the Sn content is higher, hence being the main matrix. Simultaneously, other constitutive elements are oxidized on the surface to yield a mixed oxide that forms a passivation layer, as shown in Figure 5.4. In the beginning, however, this layer is unstable, reacts with chlorides and breaks down easily. This incident enables another cycle of oxidation and material spalling. This principle of oxide layer reactions is employed during the process of PCB soldering, which is performed in a controlled atmosphere mainly using inert gas such as N₂ containing a trace of less than 1% formic acid. The acid spontaneously reacts with oxides on metals and metalized ions to form metal formats. The formats will eventually decompose or vaporize at soldering temperature.

Table 5.2: Galvanic series of commercial metals in seawater

Metal	Electrode Potential, E° (V)	
Al	-1.66	
Fe	-0.44	
Sn	-0.1375	
Cu	+0.34	
Ag	+0.7996	
Ag₃Sn	+0.7996	
		Noble/Cathodic

For Sn, the pit nucleation step alone could involve Cl⁻ adsorption on the passive surface, ionic transport processes in the oxide, void formation or pore formation. The formation of voids is also a function of polarization, similar to an observation by Mohanty et al. (2013). The void origin was assigned to cation and anion vacancy saturation at the metal/oxide interface resulting from the ionic transport properties in the oxide. Hence the non-uniform surface degradation could be a result of uncontrol and non-uniform contact between the metal and the oxide on the surface.

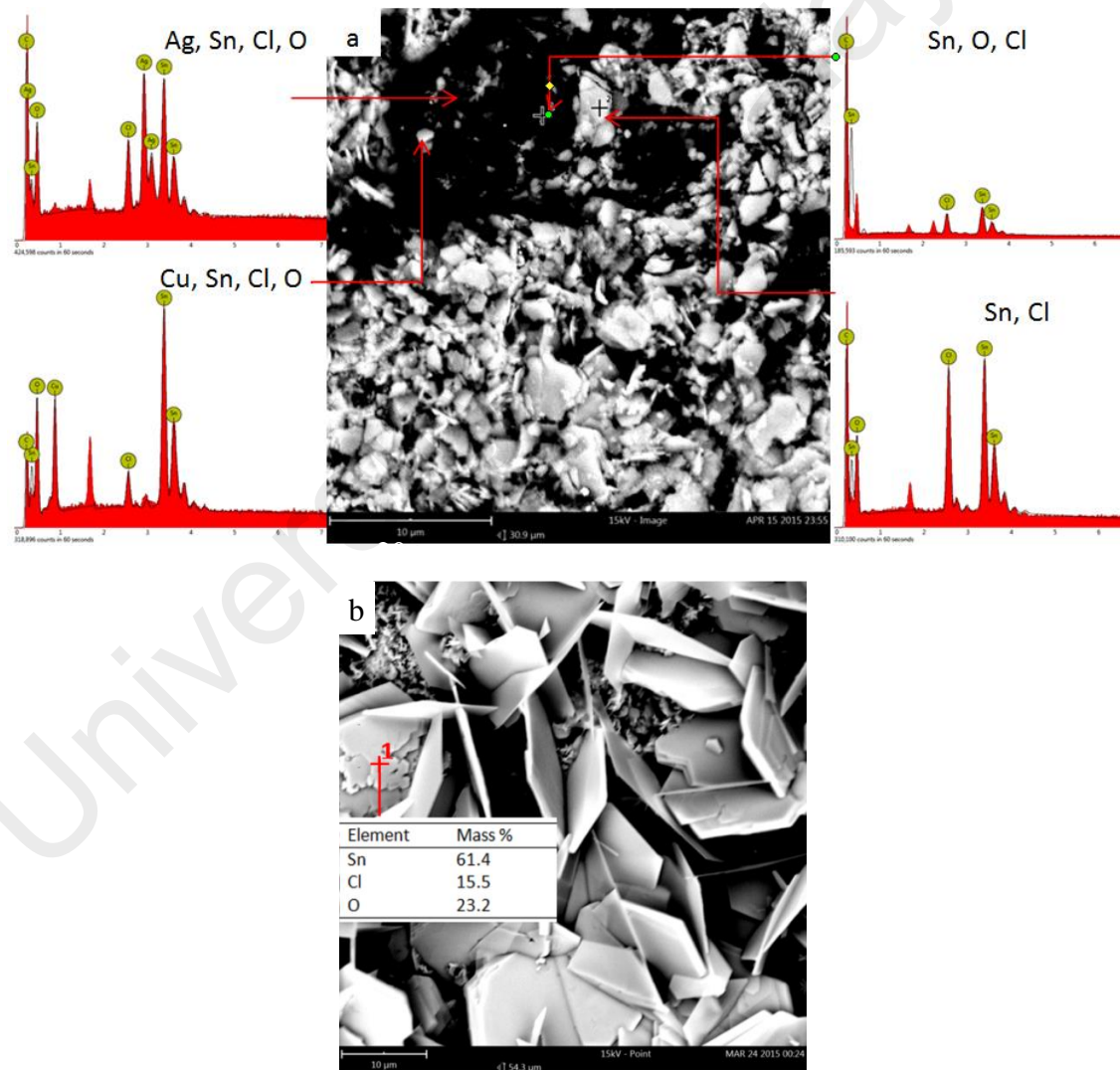


Figure 5.4: EDX analysis of SAC105 solder alloy after salt spray test

5.1.1.2 Interfacial reaction as reflow

One of the characteristics of IMC at the solder/substrate is the scallop-type morphology. Figure 5.5a shows the cross section micrograph of the as-soldered SAC105/Cu sample. The solder-Cu pad reaction layer shows this specific morphology formed at SAC105/Cu interface consist of Cu_6Sn_5 after 1x reflow. Through EDX analysis, the composition of this layer is approximately 45.2 at. % Sn and 54.8 at. % Cu.

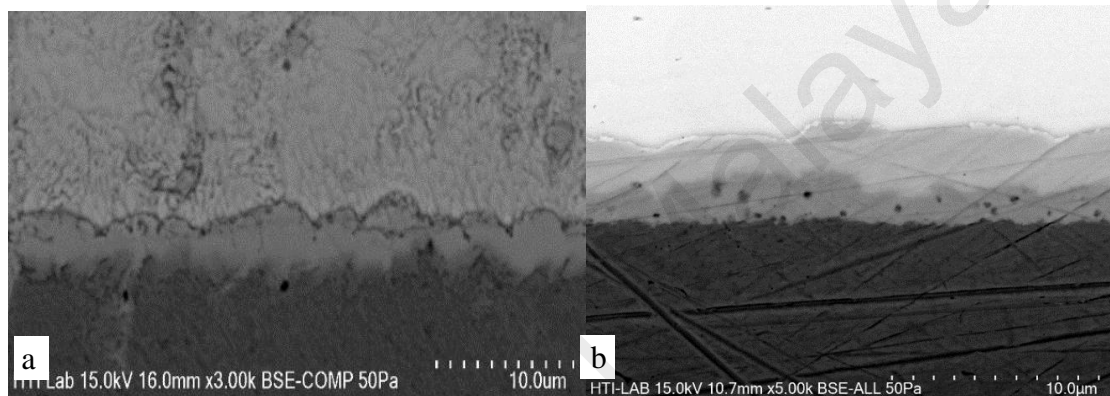


Figure 5.5: FESEM micrographs of SAC105 (a) as reflow (b) 96hour aged, 180°C

In soldering, interactions between the substrate and the molten solder eventually form interfacial phase and growth of IMC layer near substrate. Generally, the formation of IMC and its growth is a complex processes. The initial process is the instantaneous partial dissolution of substrate into the molten solder upon contact. The dissolution progress and become saturated near the substrate's interface. This prompts to the ensuing growth and formation of interfacial layer. In the Sn/Cu system, the process starts with dissolution of Cu that is through substrate into the molten solder. Subsequently the formation of Cu–Sn IMCs in a form of Cu_6Sn_5 and Cu_3Sn particles.

According to the analysis on kinetics of dissolution of solid in liquids by Dybkov, Cu dissolution in molten solder is express as the equation below,

$$\frac{dc}{dt} = k \times S \times V (C_s - C) \quad (5.1)$$

The main concern is the $(C_s - C)$ of the equation where this part implies the dissolution mechanism of Cu. Substituting k (dissolution rate), S (substrate surface) and V (solder volume as constant, a higher $(C_s - C)$ implies higher rate of Cu to dissolve. C_s represents the solubility of Cu while C represents the Cu substrate concentration in the molten solder (Dybkov, 1998). The similar mechanism applies to the IMC dissolution in the liquefied solder. Therefore, the rate of Cu dissolution is significantly affected by the initial Cu content in the solder (Yu et al., 2005; Choi et al., 2000). As local concentration of Cu at the interface exceeds solubility limits of Cu ($C > C_s$), Cu_6Sn_5 formation starts at the interface. Concurrently, atoms around the interfacial region continuously diffuse into molten alloy. The mechanism is due to the differences in concentration of Cu at the interface and affecting the drop of Cu concentration to be lower than the limit of solubility. The scattered Cu_6Sn_5 particles continuously dissolve to sustain the equilibrium (Choi et al., 2000; Yu et al., 2005; Zeng et al., 2010).

Soldering is a process of instantaneous growth of IMC and dissolution of Cu. The dissolution of the Cu_6Sn_5 occurs until molten solder is in Cu saturation. This results in mixed mechanism that controls the IMC layer thickness. This mechanism is possible through the surface that is in contact with the molten solder or through the grain boundaries. The continuous diffusion from the substrate during soldering is through the interface layer which is formed by Cu_6Sn_5 and along the grain boundaries between the IMC and the molten solder interface (Lord & Umantsev, 2005). It then reacts with the adjacent Sn within the adjacent molten solder. The process alters the thickness of the interfacial layer. Conclusively, the thickness is the effect of Cu dissolution rate and its ability to react with Sn to form Cu_6Sn_5 . Secondly, the Cu diffusivity due to the prompt and continuous occurrence of the concentration gradient.

5.1.1.3 Interfacial reaction after aging

The formation of another IMC layer in between and Cu substrate was observed and the thickness of Cu_6Sn_5 and Cu_3Sn IMCs after ageing is shown in Figure 5.5b. The interface layer evolves continuously with further ageing at solid state, resulting in morphology and layer thickness alteration, due to the diffusion mechanism between Cu and Sn (Yang et al., 2013; Li et al., 2013). This is because there are two IMC layers formed in between the bulk solder and the substrate. As reported by other researchers (Liu et al., 2009; Li et al., 2013; Hu et al., 2014), who found that Cu_3Sn formed and grew rapidly within 115–180°C of ageing. The growth of Cu_6Sn_5 layer by spontaneous and continuous diffusion of Cu and Sn, while the Cu_3Sn layer forms and grows when Cu contained in substrate reacted with the Cu_6Sn_5 . The reaction is express in the equation below:



Consequently, a great diffusion reduction of Cu atoms from Cu_6Sn_5 to the molten solder . As a result, Cu_3Sn grows rapidly by consuming Cu_6Sn_5 at the interface of $\text{Cu}_3\text{Sn}/\text{Cu}_6\text{Sn}_5$ as mentioned in the Eq. 5.2. Due to Cu deficiency, the growth of Cu_6Sn_5 on the solder side is suppressed.

In Figure 5.5b, after the IMC layer was formed, the layer continuously grow at the expanse of Cu substrate. The scallop-like morphology growth is perpendicular to the formed IMC layer (Cu_6Sn_5) (Gorlich, et al., 2005). Once the Cu_6Sn_5 layer formed, the thermodynamic between Cu_6Sn_5 /substrate enables the initiation of Cu_3Sn phase layer. This phenomenon is achieved in later stage of the soldering reaction, commonly the layer will already observable after 24h of ageing. The thickness of the Cu_3Sn is thinner than Cu_6Sn_5 because Cu_3Sn occur through solid state diffusion which is very slowly.

The evolution of Cu-Sn interface layer at Cu substrate is based on the continuous growth of Cu_6Sn_5 after ageing and on the formation and evolution of Cu_3Sn in between

Cu_6Sn_5 and the substrate. The layer growth depends on diffusivity and correlate to the Cu concentration within the alloy and also the adjacent layer of IMC or substrate (Vianco, 1999). The equation governing the phase stability that causing the formation of Cu_3Sn is as written in Eq. 5.2.

Conversely, Cu_3Sn could either dissolve itself to produce Cu_6Sn_5 or is also possible to react instantaneously with Sn atoms to form Cu_6Sn_5 . The transformation equations Cu_3Sn from to Cu_6Sn_5 are shown as follows:



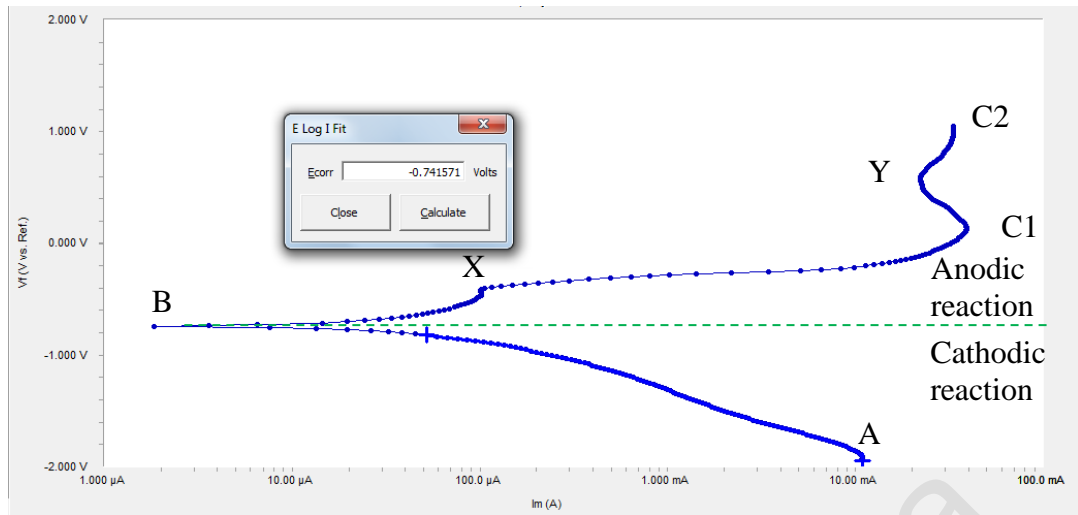
While cooling, some part of Cu_3Sn will transform back to Cu_6Sn_5 by the peritectic reaction. Mainly the part that is near to the bulk solder.



The Cu_6Sn_5 has a larger flux of interdiffusion compared to Cu_3Sn , hence it was formed earlier. The mechanism is related to the change in Gibbs free energy and the reaction from growth rate. The superior ability of Cu_6Sn_5 to form easier and earlier than Cu_3Sn is attributable to its large interdiffusion flux. Additionally, the governing mechanism could be related to the product of Gibbs free energy and also the resulting reaction from their inherent rate of growth.

5.1.2 Corrosion behaviour through potentiodynamic polarization

The potentiodynamic polarization technique permits the measurement of the polarization behaviour of the investigated solder alloy by continuously scanning the potential while monitoring the current response. Figure 5.6 shows the results of the potentiodynamic polarization curve of SAC105 solder alloys immersed in 5wt% NaCl. The polarization behaviour shows a Tafel (activation control) of SAC105 to approximately 700 mV. Then, the plot gradually enters mixed activation-diffusion control for approximately 850 mV.



Material	E_{corr} (mV)	I_{corr} (μA)	Corrosion Rate(mmpy)
SAC105	-741.6 mV	70.8	2.302

Figure 5.6: Potentiodynamic curve for SAC105

The polarization tests were conducted in an aerated solution, hence the curve at cathodic part (region A to B) relate to the reduction reaction, described by Eq. 5.6:



Rapid increase in current in Figure 5.6 as the potential in the anodic direction inclined. The peak observed at B is ascribed to the starting of an active material dissolution during polarization of the solder alloys to 750 mV. While region B to C in the curve corresponds to an increased dissolution with further increase of the voltage. At this region, an increase of potential results in simultaneous current increase which indicated material is still conducting current through it. The anodic dissolution of Sn produce Sn^{2+} and Sn^{4+} (Almeida, Rabóczkay, & Giannetti, 1999; Ogura, 1980). This chemical activity is shown in Eqs. (5.7) and (5.8):

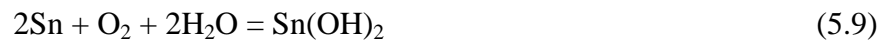


Subsequently from this reaction, formation of Sn^{4+} ions as follows:



The dissolution of Sn will also be affected by the existence of other elements within the solder matrix. This is due to the electromotive force hold by each adjacent elements of the dissimilar materials of an alloy. The electrode potential of Ag and Sn are 0.7996 V and 0.1375 V, respectively. The difference in potential will spontaneously induce the dissolution of Sn into the corrosive solution as Ag possesses higher potential, hence is more inert. Moreover, a previous study by Mori, Miura, Sasaki, and Ohtsuka (2002) reports that the presence of Ag₃Sn in SAC solders accelerates the dissolution of tin attributable to galvanic corrosion. Through a potentiodynamic polarization test, the corrosion potential (E_{corr}), corrosion current (I_{corr}) and corrosion rate for SAC105 solder alloy is found to be -741.6 mV, 70.8 μA and 2.302 mmpy, respectively.

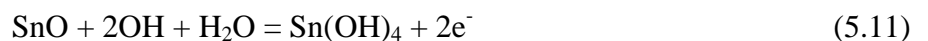
Point B in Figure 5.6 is the corrosion potential (E_{corr}), the point is the intersection of the extrapolated anodic and cathodic Tafel slopes. The corrosion potential (E_{corr}) towards lower potential values indicates a rise of Sn dissolution which is related to higher reactivity and vulnerable to corrosion. The dissolution of Sn continues with the potential increase until the concentration of the corrosion products on the surface are too dense and thus obstruct further current increase as at points C1 and C2. The current at these points are at its maximum and the potentials at this point are referred as the passivation potentials (E_{pp}). Formation of Sn oxides occurred and hinders further corrosion processes. The formation of the layer follows the equations set forth below:



Dehydration of $\text{Sn}(\text{OH})_2$ forms SnO



While SnO_2 could be from the continuous oxidation of SnO that formed $\text{Sn}(\text{OH})_4$ which partially hydrate and produce SnO_2 . The reactions is as below:





The corrosion products containing Sn(OH)_4 is highly insoluble and precipitates. This eventually will promote more protective passivation film. Hence, dehydration process increase the corrosion stability (Abd El Rehim, Zaky, & Mohamed, 2006). At higher over potentials, the fractions of diffusion control from the total polarization increase, presumably indicating the formation of oxide and a deposit effect of reaction with chloride ions (SnCl , SnO , Sn(OH)_4) on the specimen surface. Other works have also discussed partial stabilization that involved active-passive events attributable to the dissolution of Sn, the formation of oxide layers and the possible initiation of precipitation and dissolution of SnCl_2 , Sn(OH)_4 , SnO and SnCl^{-3} (D. Li, Conway, & Liu, 2008; X. L. Zhang, Jiang, Yao, Song, & Wu, 2009).

5.1.3 Shear Strength of Solder Joint

The solder joints for solder ball/substrate shear tests were loaded to failure in a shear mode at a shear speed of 0.01 mm/sec. Figure 5.7(a) represents the shear stress/strain curve of the test samples. At solder joint, the elastic part of the curve is comparable for all four conditions. This indicates that the shear modulus is not affected by varying the pre-treatment by exposing to salt spray with or without ageing.

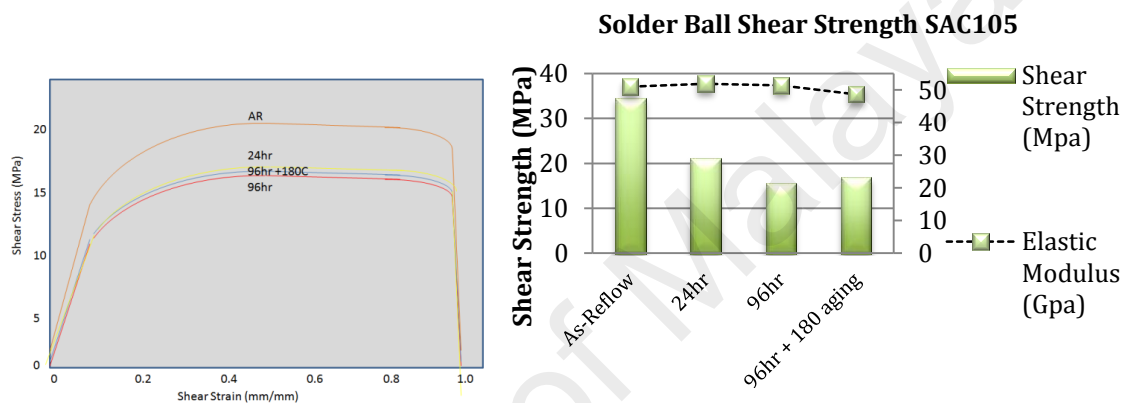


Figure 5.7: (a) Stress-strain curve (b) shear strength of SAC105 solder ball interconnect, before and after salt spray test and after ageing

For as-reflow sample, the values of Young's modulus are within the values found in the literature, which range from 30 GPa to 66 GPa (Kanchanomai, Miyashita, & Mutoh, 2002; Vianco et al., 2003). The similarity is in the inclusion of the impact of the intermetallic layer at the actual solder joints. The wide range of differences results from the different parameters of settings such as solder joint dimensions, shear speed, shear height and the reflow process setting. On another note, the values in the literature for the shear of the bulk solders will give different results and most commonly are much lower than those of the shear assessment of joints. This is because the IMCs that are sparsely distributed within the microstructure have a lower impact than the IMCs that form a continuous layer between the bulk and the substrate. With respect to the SAC105 solder alloy, the IMC layer

mentioned is the Cu_6Sn_5 . This IMC is in a form of particle that is randomly distributed within SAC105 microstructure. It also exists in a layer form as the result of a reaction between the β -Sn matrix and the Cu-substrate of the PCB board. The Cu_6Sn_5 interface layer is important because it defines the solder joint strength of the components on the PCB board.

The average Cu_6Sn_5 layer thickness was measured as $3.85\text{ }\mu\text{m}$ for SAC105. Cu_6Sn_5 was the only IMC found at the interface layer. The Cu_6Sn_5 IMC is known as a brittle compound, whereas β -Sn has a ductile characteristic. The sliding shear before total rupture that is seen in the stress-strain curve in Figure 5.7a indicates that the solder alloy is experiencing ductile shear failure. Therefore, the failure is suggested to occur in the bulk region where β -Sn is the dominant constituent. Ductile fracture mode is the most desired for solder joints where there is residue on both sides of the joint, the IC and the substrate. This suggests that the solder alloy used has excellent metallurgical bonding that ensures reliability under harsh handling or environments.

5.2 Sn-1Ag-0.5Cu solder alloy bearing 0.1 wt. %, 0.3 wt. % or 0.5 wt. % Fe

Previous sections presented the results of SAC105, which will be the benchmark data for this study. This subsection will discuss the results of the impact of adding 0.1 wt.%, 0.3 wt.% or 0.5 wt.% Fe to SAC105. Similar to the focus of the outcome related to the microstructure, the IMC layer formed for as-reflow and after aging, its solders joint strength, and its inherent corrosion behaviour will be emphasized and elaborated. A comparison with the result from section 5.1 will be made concurrently.

5.2.1 Surface morphology and microstructures

The top view of SAC105 and Fe-added SAC105 solder balls attached on a Cu substrate is shown in Figure 5.8. As the content of Fe increases from 0.1 wt. % to 0.5 wt.%, the solder ball exhibits a surface similar to that of the SAC105 after 1x reflow. The samples were further positioned in a salt spray chamber for 24 hours and 96 hours and aged at 180 °C for 24 hours before being placed in the chamber. Although slight surface morphology degradation was seen after 24 hours, the surface changed dramatically after 96 hours of exposure to the salt spray. Interestingly, for all aged samples, the surface appeared to be unaffected by the corrosion threat induced by the salt fog, even after 96 hours in the chamber.

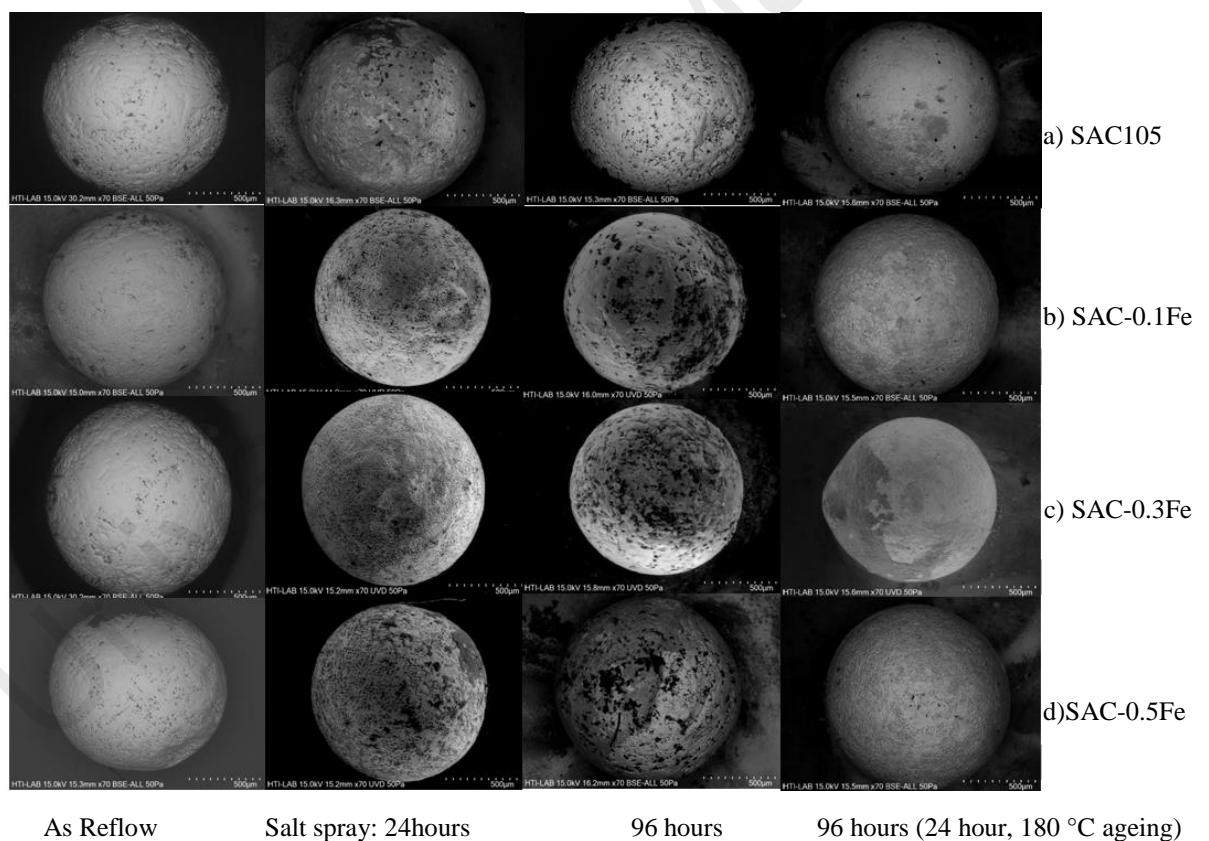


Figure 5.8: FESEM micrographs of SAC105 and Fe-added SAC105 solder balls after salt spray test and 24 hr of ageing at 180 °C

As seen in the surface morphology, as the additions of Fe increase from 0.1 wt. % to 0.5 wt. %, the surface morphology degrades along a linear trend. The trend shows a correlation between the time of exposure to NaCl and the weight percentage of Fe in SAC105. This correlation is associated with the inherent microstructure of the solder alloy. The most common cause of material spalling from the surface of an alloy is the unstable electromotive force (EMF) at the grain boundary between the adjacent elements within the microstructure of the alloy. Specifically, for SAC105 with added Fe, these elements would be the intermetallic particles and the Sn matrix. As in the phase diagram of Figure 5.9a, SAC105 consists of Ag_3Sn and Cu_6Sn_5 IMC particles. Thus, with the addition of Fe, the solder alloy is added with FeSn_2 ; see Figure 5.9b. Different IMC forms as the temperature increases and Fe is expected to form FeSn_2 in the Sn matrix when the solder alloy is heated between 231.9 °C and 513 °C. The quantitative analysis of the investigation, in which potentiodynamic polarization analysis was performed, will be described in the next section. The aim is to demonstrate the corrosion behaviour resulting from the local electrode formed by these IMCs within the Sn matrix.

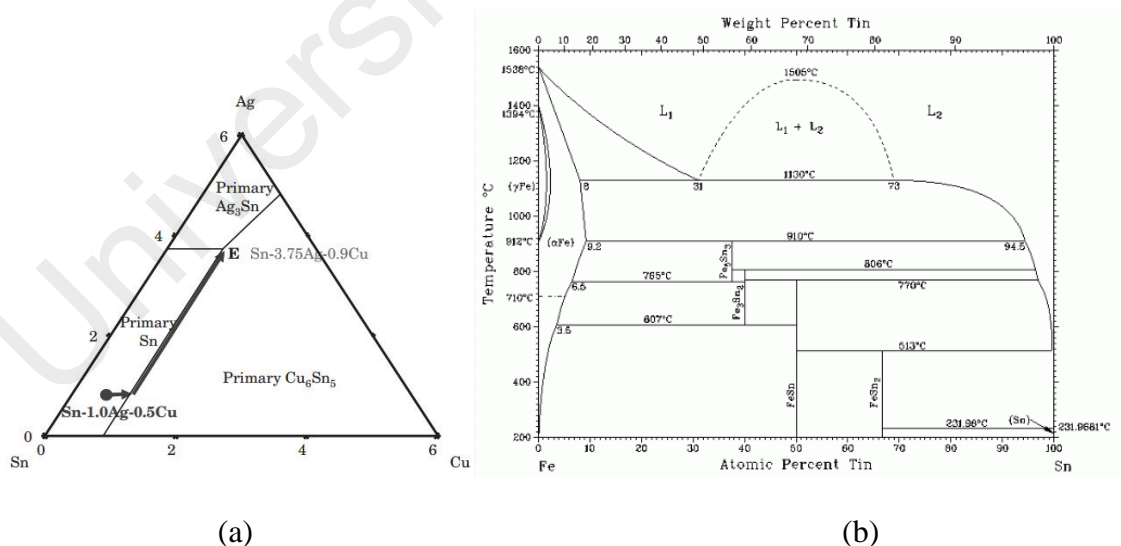


Figure 5.9: Phase diagram of (a) Sn-Ag-Cu (b) Fe-Sn (ASM International)

5.2.1.1 Interfacial reaction as reflow

The FESEM micrographs in Figure 5.10 display the cross section of Fe-added SAC105 soldered on a Cu substrate. They are two parts of the micrograph that could provide input into the investigation on the impact of minor Fe addition in SAC105. First, as noted earlier, FeSn₂ IMC was formed after minor alloying. The micrographs in Figure 5.10 (d,h,l) of the cross-sectioned samples exhibit the large circular FeSn₂ IMCs. The IMC is located in the interdendritic region. This could explain the poor surface morphology, as seen in Figure 5.8, associated with the linear trend on salt exposure and percent of Fe added into the SAC105. The enlargement of the corroded area is associated with the EMF strength of each IMCs and the β -Sn. The Ag₃Sn, Cu₆Sn₅ and FeSn₂ IMCs are not only brittle but also more noble than Sn. Instantaneous pairing of local electrodes to form anode-cathode pairs between the adjacent elements is expected to occur whenever the solder alloy is in a humid environment. Humidity initiates the reduction-oxidation mechanism that introduces the microstructure to the threats of the free corrosive ions. Often, these ions penetrate the surface layer and establish a pit that enlarges, widens and merges over a period of time to create even greater morphology degradation. In addition to including large circular FeSn₂ IMCs, it also includes itself in Cu₆Sn₅ and Ag₃Sn and enlarges the β -Sn dendrite. Inclusion in the IMCs suppresses the coarsening of Ag₃Sn and Cu₆Sn₅ IMCs during ageing, also described by Shnawah et al., (2012). This incident could explain the surface of the ageing samples in Figure 5.8 that exhibit a morphology similar to that of SAC105.

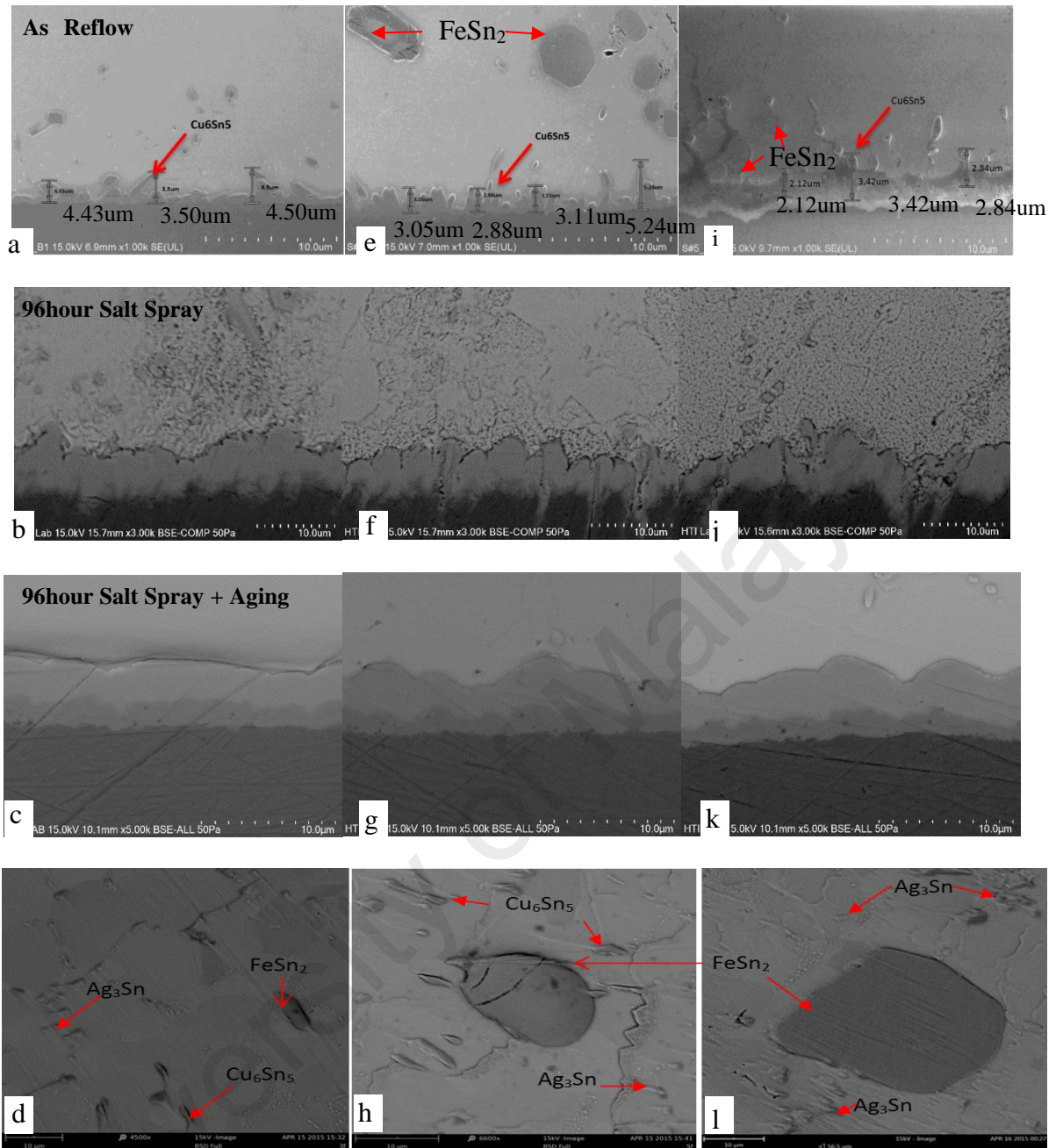


Figure 5.10: Cross sectional FESEM micrographs (a-d) SAC105-0.1Fe (e-h) SAC105-0.3Fe (i-l) SAC105-0.5Fe after 1x reflow, 96-hour salt spray test and ageing, respectively.

It is vital to conduct further investigations of the solder/substrate interface layer because of the possibility that the IMC thickness of the Cu_6Sn_5 at the interface layer is altered by the inclusion of Fe. Table 5.3 summarizes the IMC interface thickness formed on the Cu substrate. Fe addition to SAC105 led to a slightly thicker IMC layer as reflow samples. The varying thickness compared to SAC105 is between 4.05% and 30.6%. The thickness was seen to decrease as the wt% of Fe increased.

Table 5.3 Intermetallic thickness at solder/substrate joint for as-reflow a) SAC105
b)SAC105-0.1Fe c) SAC105-0.3Fe and d) SAC105-0.5Fe

Thickness (um)	SAC105	SAC105-0.1Fe	SAC105-0.3Fe	SAC105-0.5Fe
As reflow	3.1625	4.5575	4.004	3.296

The melting temperature sustain but the degree of undercooling of SAC105-Fe increase from 207.82 °C to the between 194 °C and 197 °C. Conversely, the range shows decreasing values as the amount of Fe increases (Fallahi, Nurulakmal, Arezodar, & Abdullah, 2012; Shnawah, Said, Sabri, Badruddin, & Che, 2012). Decreasing under-cooling indicates that the melting and solidification phase occurs too swiftly. Consequently, it is difficult for Ag_3Sn and Cu_6Sn_5 IMCs to enlarge. Additionally, smaller amounts of Sn-rich solders reacted with Cu, which requires a large under-cooling to nucleate and solidify (Elmer, Specht, & Kumar, 2010; Reid, Punch, Collins, & Ryan, 2008). Therefore, the thickness of the IMC layer decreases as the Fe addition to SAC105 increases.

5.2.1.2 Interfacial reaction after ageing

Figure 5.10 (c,g,k) shows the cross-sectional micrographs of isothermally aged SAC105-0.1Fe, SAC105-0.3Fe and SAC105-0.5Fe. After thermal ageing for 24 hours and exposed to 96 hours of salt spray, another (inner) intermetallic layer is formed between the first IMC layer (Cu_6Sn_5) and the Cu substrate in both SAC105 and Fe-added SAC105 solder

alloys. Using elemental ratio by EDX analysis, it is confirmed that Cu_6Sn_5 is the outer layer and the inner layer is Cu_3Sn ; the ratio is shown in Figure 5.12. By using EDX, Fe was not detected within both interfacial layers formed after thermal ageing. The figure plotted the corresponding layer thickness as a function of Fe content. It is conclusively shown that SAC105 solder alloy preserves strength at the solder joint with the minor addition of Fe. Cu_3Sn is known to be more brittle than Cu_6Sn_5 . Therefore, the ability of SAC105 to keep the layer thin after the addition of Fe will allow the mechanical properties to be similar to those of SAC105.

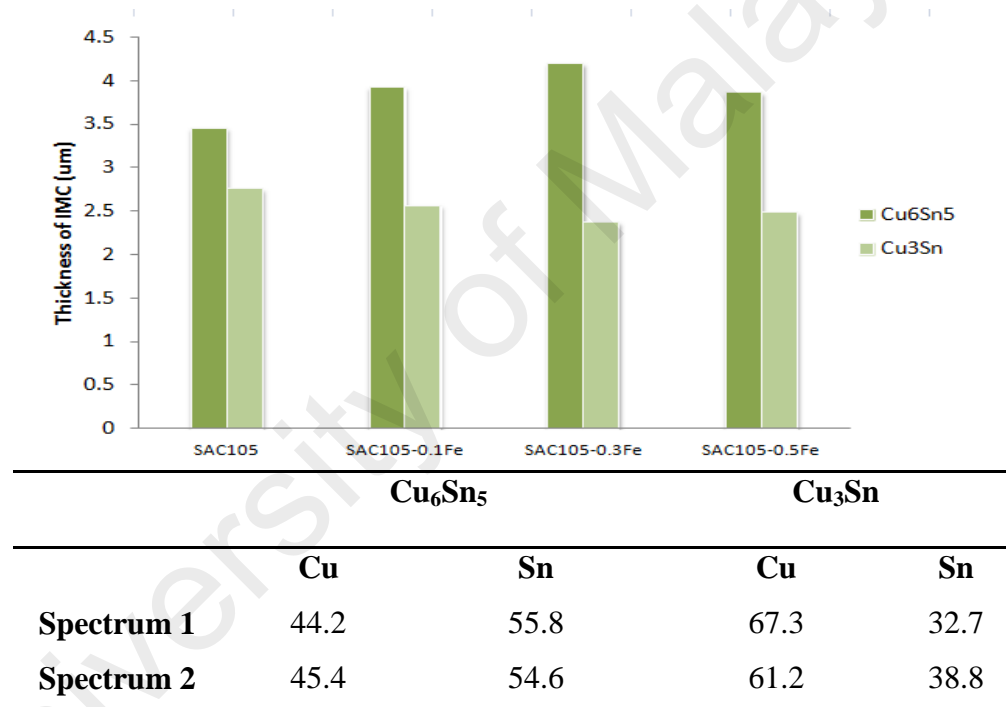


Figure 5.12: Variation of IMC thickness with Fe addition after ageing at 180 °C for 24 h.

5.2.2 Material corrosion behaviour in potentiodynamic polarization

The potentiodynamic polarization technique permits the measurement of polarization behaviour of the investigated solder alloy by continuously scanning the potential while monitoring the current response. Figure 5.13 shows the results of the potentiodynamic polarization curve of SAC105 and the Fe-added solder alloys being immersed in 5wt%

NaCl. The polarization behaviour shows a Tafel (activation control) of SAC105 and 0.1 Fe addition SAC105 to approximately 700 mV and only 100 mV for 0.3wt% and 0.5wt% Fe-added compositions. Next, the plot gradually enters mixed activation-diffusion control for approximately 850 mV.

As seen in the curve in Figure 5.13, rapid increase of current with further scanning of the potential in the anodic direction. The E_{corr} for all Fe-added solder alloys displayed a more negative potential, thus indicating more active dissolution of Sn from the solder matrix. A summary of all of the corrosion potential and corrosion current density is tabulated in Table 5.4. That same principle, the presence of FeSn_2 in the solder matrix, had a synergistic impact with Ag_3Sn , accelerating the dissolution of Sn attributable to the galvanic corrosion mechanism. Although it has been reported that FeSn_2 is chemically inert, the compound's potential has been reported to be more positive than those of the forming metals, thus explaining the spontaneous anodic reaction of the Sn matrix to the compound (Covert & Uhlig, 1957).

Table 5.4 Corrosion properties of SAC105 and SAC105-xFe

	SAC105	SAC105-0.1Fe	SAC105-0.3Fe	SAC105-0.5Fe
Corrosion Rate(mmpy)	2.302	1.665	4.132	3.978
I_{corr} (μA)	0.5199	0.513	1.279	1.237
E_{corr} (mV)	-768.7	-822.2	-815.9	-870.2

Point B in Figure 5.13 points the corrosion potential (E_{corr}) for SAC105 and Fe-added SAC105 solder alloys. It was observed that with an increase in the Fe content from 0.1wt.% to 0.5 wt.%, the corrosion potentials (E_{corr}) were shifted towards more negative values. This indicates that with more Fe content, dissolution of tin increase. The dissolution of materials continues with increasing potential until current reached a critical

value at points C1 and C2. The critical current density observed at these points are the optimum (Rosalbino et al. 2009); the potential corresponding to this current is referred to as the passivation potentials (E_{pp}). At this point, oxide layers and other corrosion products have fully covered the surface, the corrosion products gathered on the surface of the samples after test are as shown in Figure 5.14.

Beyond this potential, the onset of the layer on the material surface that creates passivation cause the rapid drop of the active current. The rightwards shift of curves for Fe added SAC105, possibly because of the higher density of SAC105 with added Fe. The densities are 7.3097 g/cm^3 , 7.3108 g/cm^3 and 7.3118 g/cm^3 for SAC105-0.1Fe, SAC105-0.3Fe and SAC105-0.5Fe, respectively. Thus, the relative densities were approximately 0.0074%, 0.022% and 0.037% for SAC105-0.1Fe, SAC105-0.3Fe SAC105-0.5Fe, respectively. In these fourth element alloyed samples, the surface density increases the effective area for galvanic pairing, which could induce pitting corrosion. This instantaneously affects the associated current density compared to the ternary SAC105.

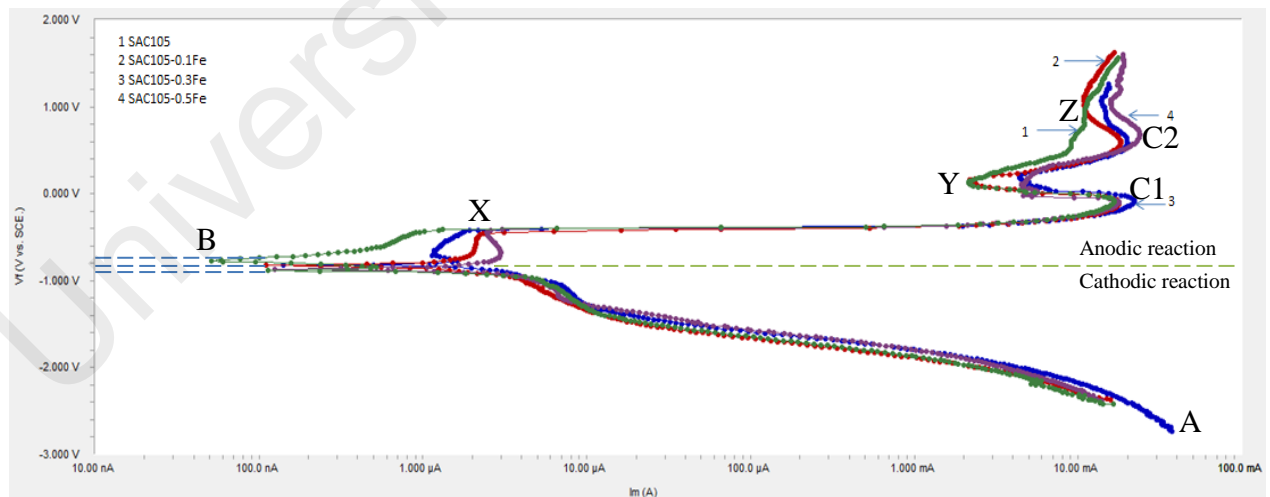


Figure 5.13: Potentiodynamic Curve for SAC105 and Fe-added SAC105

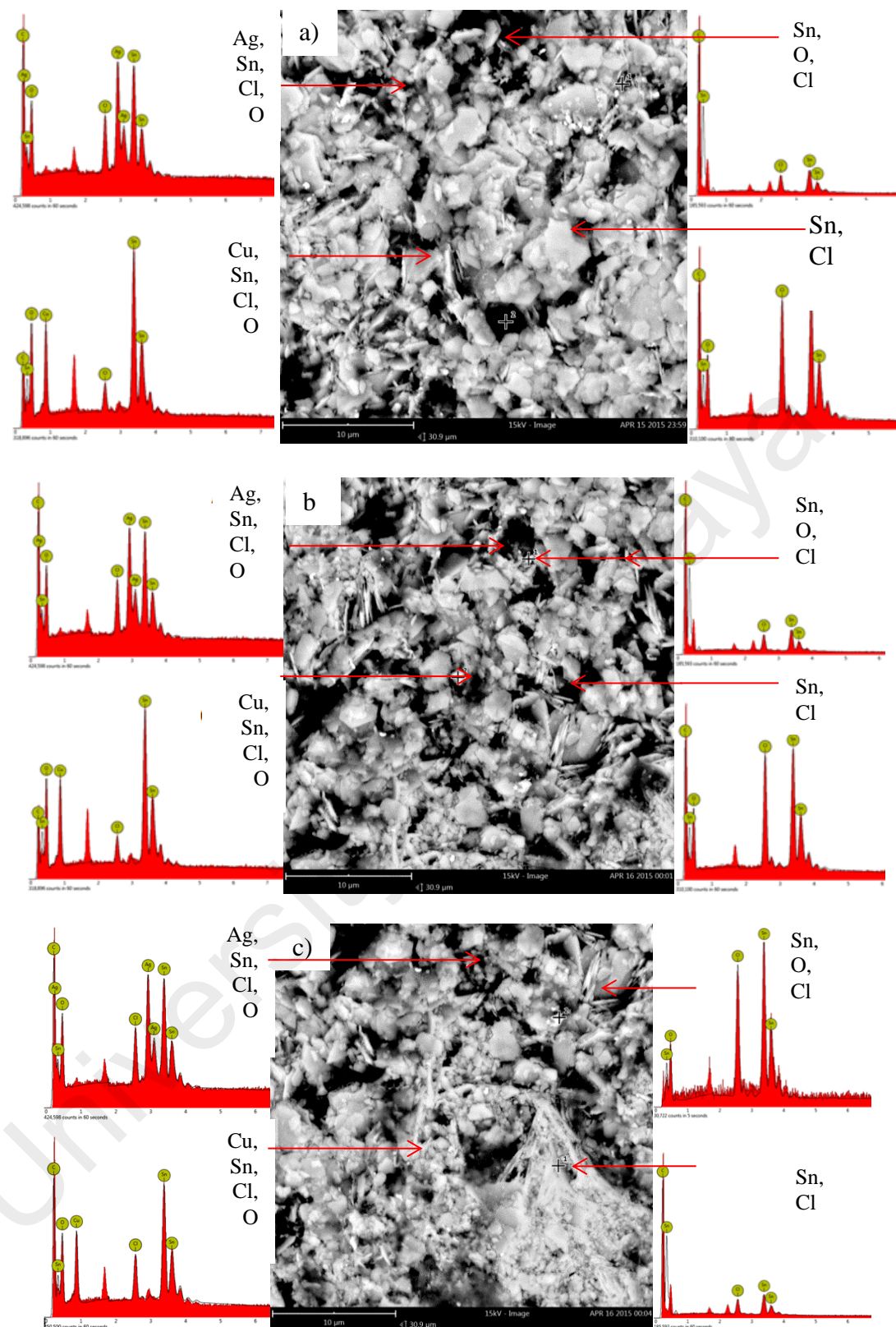


Figure 5.14: Surface morphology of polarized a) SAC105-0.1Fe b) SAC105-0.3Fe and c) SAC105-0.5Fe at 10 μm magnification

The anodic regions in the potentiodynamic polarization curve of SAC105 and SAC105-Fe ($x = 0.1, 0.3, 0.5$ wt. %) involve two peaks, four peaks, five peaks and six peaks,

respectively. This implies the natural switching of incidents of permanent surface passivation and dissolution of surface elements in the corrosive media. These results are similar to those reported in previous studies of higher Ag content SAC alloys. (Álvarez, Collazo, Nóvoa, & Pérez, 2014; Bui et al., 2010; Wang, Wang, Feng, & Ke, 2012). These results indicate that the SAC105-0.1Fe solder alloy demonstrates passivation abilities and corrosion resistance properties similar to those of the SAC105 although with the minor addition of the reactive element of Fe. The corrosion resistance of the other Fe-added alloys degraded approximately 0.04 to 0.1% from the total 0.25 cm² area exposed in the polarization test.

Certain assumptions can be made about the passivation of SAC105-xFe solder alloy. Sn, which is the main constituent of the matrix and also the least noble component of the alloy, will be the first to react. This event will eventually lead to the formation of a passivation tin oxide layer on the surface. The partial protective layer eventually will inhibit further element dissolution from the alloy. However, the presence of multi-IMCs within the solder matrix, namely Ag₃Sn, FeSn₂ and Cu₆Sn₅, presumably contribute to the dissolution and passivation behaviour of the alloy through corrosion caused by galvanic series. The galvanic series tabulated in Table 5.2 shows a rank of single element and IMCs related to the study.

As previously reported by Covert et al. (1957) that was proven by micropotential measurement, FeSn₂ is an inert compound in NaCl solution. This is because of the inability to measure the corrosion rate given that the magnitude is too low to be easily measurable. This insightful finding indicates that the impact of the presence of FeSn₂ caused by the addition of Fe in SAC105 in the aspect of this individual IMC performance in the solution and the chemical reaction with other constituents of the solder matrix is close to unattainable. However, given that its potential is higher than that of Sn, it is likely that the

impact of Fe addition contributes to the alteration of SAC105 corrosion performance. As with IMCs that are more noble than the Sn matrix, the highest level of localized corrosion will eventually occur at the grain boundary between the IMC and the Sn. The potential difference between FeSn_2 and the Sn will continuously force the Sn to dissolve. This event creates Sn^{2+} and Sn^{4+} , as described by Eqs. (5.7) and (5.8). This attracts free chloride (Cl^-) and will form SnCl_2 and SnCl_4 . This progression eventually provides continuous electron movement that generates electric current flow, enlarging the pit spot and resulting in the rougher structure of the impacted surface. This impact is apparent in Figure 5.15, in which the remaining particles are among FeSn_2 whereas the adjacent constituents of the spot, most likely the Sn from the solder matrix, spalled off the matrix.

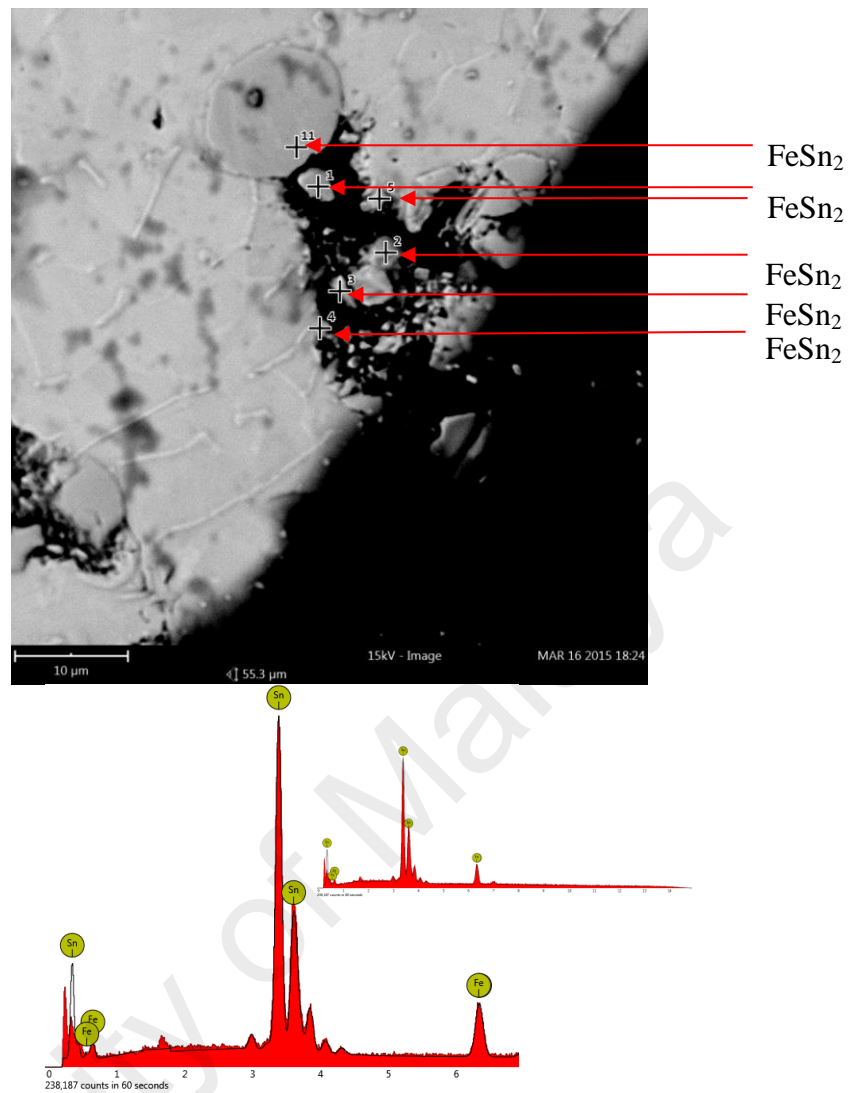


Figure 5.15: Material integration from the impact of dissimilar adjacent elements

In addition to the impact of galvanic corrosion, solder alloys are potentially threatened by the pitting mechanism. As shown in Figure 5.13, the early detection of a peak was observed in the plot for SAC105-0.3Fe and SAC105-0.5Fe at point X. This indicated a small ΔE_{pit} , meaning that the pitting corrosion potential is close to the corrosion potential, E_{corr} . However, the addition of 0.1wt% Fe yielded almost identical corrosion behaviour with SAC105, in which the first pit occurred much later than in the other compositions tested.

The corrosive agents of a free Cl^- contributed to the pitting occurrence because this ion was responsible for the rupture of oxide layer and later penetrated the localized area. This

provided the path from the electron transfer and continuity of the current flow (Ogura, 1980; Refaey, Taha, & Hasanin, 2006; Wislei Riuper, Leandro Cesar de Lorena, Leonardo Richeli, Amauri, & José Eduardo, 2012). Thus the observed peak at point X for SAC105-0.3Fe and SAC105-0.5Fe, point Y and point Z for all Fe-added alloys. At these three points, (X, Y, Z), the material experienced passivation where it had achieved the corrosion current density. A further increase in current was halted and progressed to a lower magnitude, even during the increase in potential. However, this process stops shortly after it begins. It was perceived that the current start was behaving proportionally to the increase in the potential. This indicates the start of another cycle of the material activation-passivation process. The polarized samples exhibit a similar surface microstructure between the Fe-added alloys and the SAC105. EDX scanning showed high chloride ions (Cl^-) and high O together with the high detection of Sn, Ag and Cu. As shown in Figure 5.14, these flake-like surfaces found after testing could have been SnCl_2 , SnCl_4 , SnO and SnO_2 .

Overall, the interdendritic Ag_3Sn possesses the smallest area ratio within the solder matrix. Nevertheless, these IMC particles are in a group containing multi-particles that allocate themselves close to one another and will eventually develop a closed loop formation. As discussed by Wang et al. (2012) regarding the impact of Ag_3Sn on corrosion resistance in SAC solder, this material will naturally form a cathode-anode interaction. The cathodic Ag_3Sn IMCs and the anodic Sn matrix will eventually instigate microgalvanic corrosion. The worsening resistance is proportional to the increase in Ag_3Sn . Microstructures containing finer Ag_3Sn exhibit better corrosion, and protective layers of SnO and SnO_2 were found to contribute to a better corrosion performance.

On a more significant note, the hazardous impact of exposure to salt should be inspected at the joint interface area. The ball grid array type of soldering offers a very confined and

limited space underneath the flip chip. Additionally, the concave shape of the after-soldered joint creates a potential of salt or corrosion agent residue to clog or leave unclean. This will quickly become an initiation site for pitting and galvanic corrosion when the chip is exposed to humidity. The corrosive agent is readily available at the site and is expected to transform it into the weakest spot of the joint. However, no evidence of trapped Cl⁻ or ruptured joint was seen in all of the samples tested in this specific assessment for SAC105 and Fe-added SAC105. Figure 5.16 shows that the area near the solder joint is free from any threat from corrosive activity, for 96 hour exposure in salt spray chamber. Hypothetically, material spalling off the solder matrix could occur because there is a large electromotive force (EMF) around the joint. The EMF is attributable to the pairing of inherent IMCs within the microstructure and the large β -Sn. As discussed above, Sn is the least noble element among the constituents of the alloy. Even after the addition of Fe, the FeSn₂ formed is more noble. This implies that Sn will preferentially dissolve during exposure to the salt mist because that medium promotes an electrolyte-like condition in which the Sn is anodic to the more noble elements, which are the IMCs formed in the alloy.

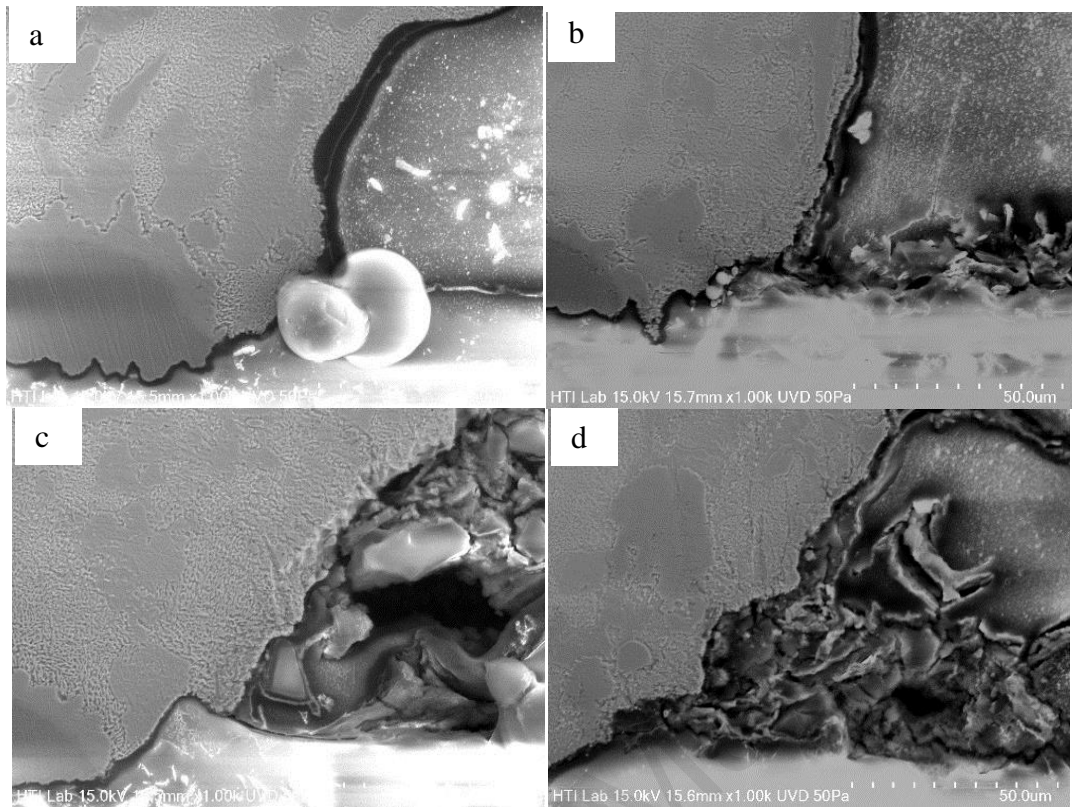


Figure 5.16: Solder joint of a) SAC105 b) SAC105-0.1Fe c) SAC105-0.3Fe and d) SAC105-0.5Fe after a 96-hour salt spray test

5.2.3 Shear Strength of Solder Ball/Cu Joint Interface

The material has the ability to absorb and distribute the stress within the bulk and crack initiated at the weakest spot, near the interface. The solder joints for solder ball/substrate shear tests were loaded to failure in a shear mode at a shear speed of 0.01 mm/sec. Figure 5.17 represents the solder ball shear strength of all samples tested. As reflow samples, a reduction of approximately 2.2% shear strength was calculated after SAC105 was added with Fe from 0.1 wt. % to 0.5 wt. %. This strength is decreased even more after the solder/substrate assemblies were placed in a salt spray chamber for 24 hours and 96 hours. Isothermal ageing produced an additional IMC interface on the Cu substrate, as shown in Figure 5.10(c,g,k). Although the Cu_3Sn is more brittle than the common Cu_6Sn_5 , its IMC

layer is thin. Hence, the tested samples were all found to preserve their strength prior to ageing.

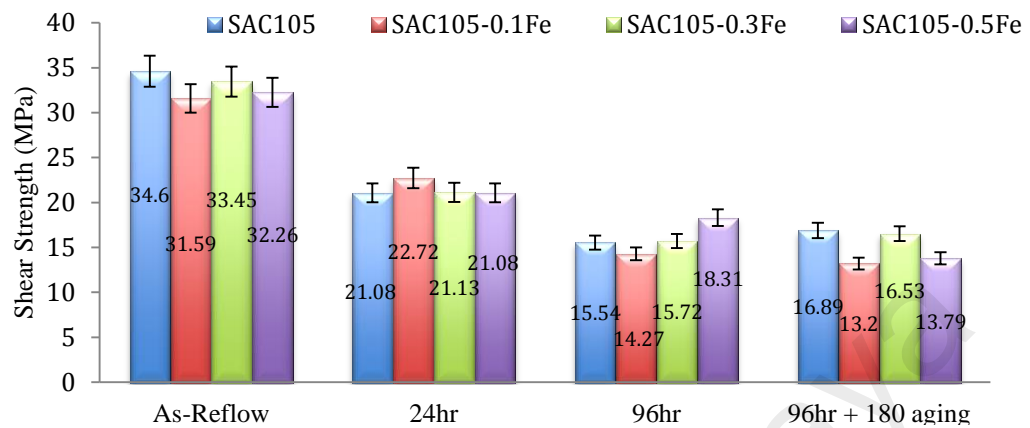


Figure 5.17: Shear strength of SAC105-xFe solder ball interconnect before and after salt spray test and after ageing

The solder joint shearing behaviour is closely related to the mechanical properties and microstructural morphology of the materials. As demonstrated by the stress-strain curve from the tensile test on bulk material, the elastic modulus of the bulk of SAC105 with minor alloying of Fe recorded a lower value than the SAC105 (D. A.-A. Shnawah et al., 2012a). Intermetallics prevalently formed in metal alloys are typically characterized by their brittleness and hardness. The addition of Fe in SAC105 induced the formation of large, circular-shaped FeSn_2 IMC particles within the matrix. Although Sn is known for its ductility, the addition of FeSn_2 distributed within the bulk created a mixed ductile and brittle microstructure. Furthermore, the presence of Ag_3Sn and Cu_6Sn_5 IMC particles aggravates the grain sliding discontinuities, which correspond to the fracture initiated at the spot of shear failure. Additionally, it could be that the large dissimilarity in mechanical properties amongst IMCs and the β -Sn leads to a weak interface within the solder matrix. The inherent mechanical properties of the IMCs play a major role in their material properties. Higher-Fe content lead-free solder has higher shear strength (H. Zhang et al.,

2014). This strength was directly correlated to the thinner, straighter IMC interface layer (C.-B. Lee, Jung, Shin, & Shur, 2002; H.-T. Lee & Chen, 2002).

The acceptable shear behaviour of these solder alloys could be explained by investigating the fracture mode. The next section will elaborate on this issue. However, it is important to mention that for Fe-added SAC105, the shear strength at the solder joint is almost identical with the core SAC105 in both treated and untreated conditions.

5.2.4 Fracture behaviour

To further study the effect of adding Fe to the SAC105 solder alloy, the fracture surface of the SAC105, SAC105-0.1Fe, SAC105-0.3Fe and SAC105-0.5Fe assembled solder joints were examined after the solder ball shear test. The surface sliding fracture mode phenomenon was seen clearly in the tested SAC105 sample. All tested samples of Fe-added SAC105 exhibit similar fracture pattern, as shown in Figure 5.18. This indicates that the fracture is ductile in nature, and the pattern slides in the direction of the shear blade motion. Thus, the addition of Fe to the SAC105 sustain the shear behaviour and the mode of fracture of the alloy.

This observation is explained by the formation of large circular FeSn_2 IMC particles that has a weak interface with the solder matrix. Therefore, at the beginning of shear, cracks are easily initiated along the interface. This eventually created nucleation sites for fracture. Due to the sparse distribution of FeSn_2 within the microstructure, the cracks surrounding these large FeSn_2 IMCs may depart from the propagation path of the boundary crack as the crack attached more to the solder matrix. Thus, the main cracks are expected to be isolated from boundary of FeSn_2 , and insignificant to failure mechanism domination. The dominant primary β -Sn dendrites within the microstructure cause the depths of these cracks to retain as malleable on further straining.

Eventually, large primary β -Sn dendrites effectively toughen the crack tip and delay the time to total fracture. This is achieved through high plasticity of the β -Sn dendrites that dissipates energy. Increasing load time caused the pulling of primary β -Sn dendrites and eventually it is sliding along the direction of loading. The plastic deformation of the primary β -Sn dendrites is not affected by the inclusion of large FeSn_2 IMCs microstructure as there is no association between the plasticity of β -Sn matrix and the IMCs. This results in an ascending internal stress and nucleation of microvoids at the interface between the β -Sn and the IMCs as the stress accumulates. The IMCs provide spots for microvoid nucleation. As it starts, the microvoid grows in both the longitudinal and the crosswise directions. Upon coalescing, the particles completely disintegrate from the matrix. Finally, the crack expanded until the solder ball/substrate joint is fully ruptured.

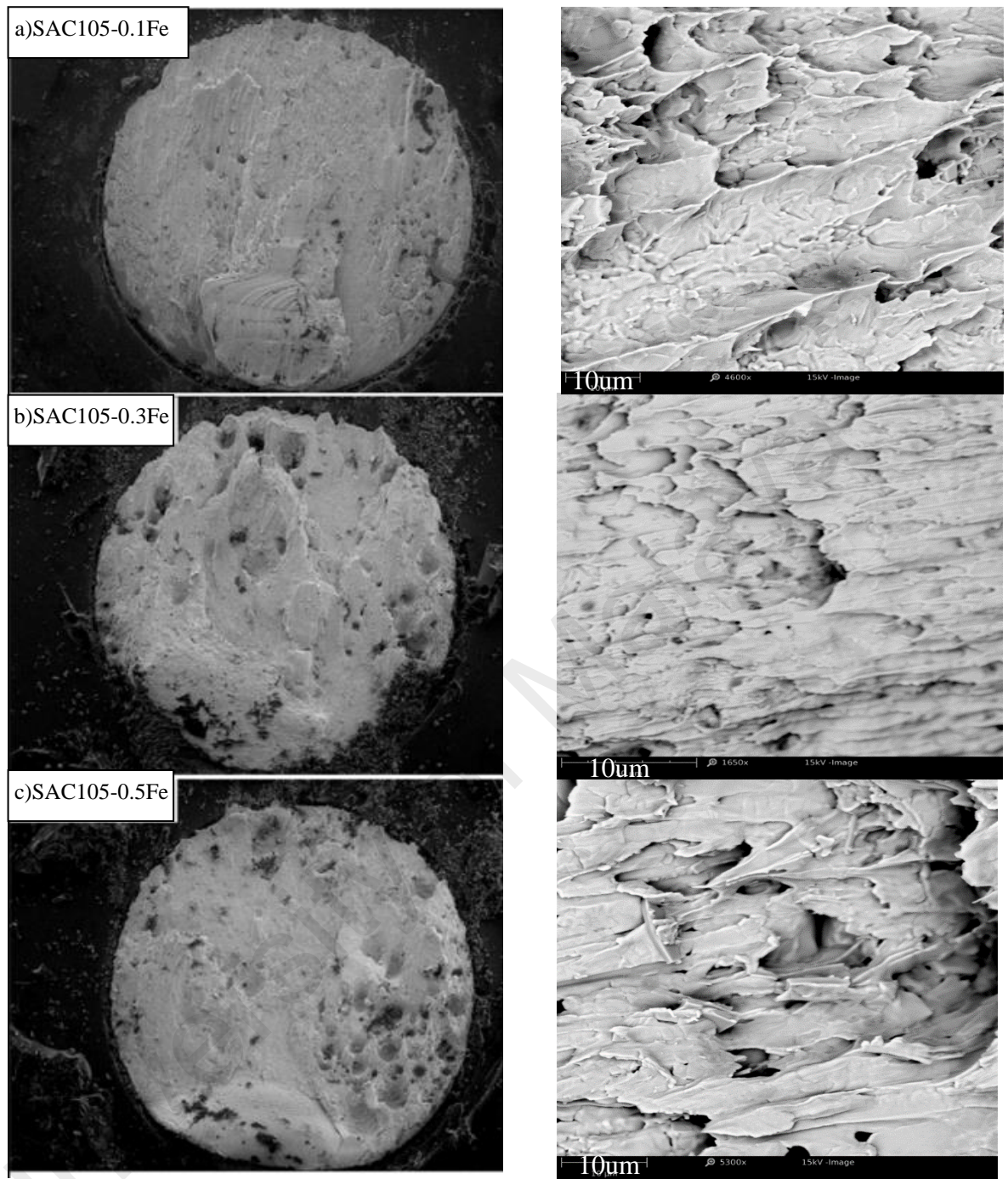


Figure 5.18: FESEM fractographs of the solder alloys after solder ball shear tests (a) SAC105-0.1Fe (b) SAC105-0.3Fe (c) SAC105-0.5Fe at 10 μm magnification

5.3 Sn-1Ag-0.5Cu solder alloy bearing 0.2 wt. %, 0.5 wt. % or 1.0 wt. % Al

Section 5.1 contains the benchmark data from the experiment performed on the core solder alloy, the SAC105. In this subsection, the results will elaborate on the impact of adding 0.2 wt.%, 0.5 wt.% and 1.0 wt.% of Al in SAC105. The results pertain to the impact on the microstructure, the IMC layer formed for as-reflow and after aging, the strength at the solder joint and the corrosion behaviour. Throughout this discussion, comparisons will be made with results gathered from the benchmark material, SAC105.

5.3.1 Surface morphology and microstructural properties

The top view of SAC105 and Al-added SAC105 solder balls attached on a Cu substrate is shown in Figure 5.19. As the Al content increases from 0.2 wt. % to 1.0 wt.%, the solder ball exhibits surface morphology similar to that of SAC105 after 1x reflow. The samples were further positioned in a salt spray chamber for 24 hours, 96 hours and aged at 180 °C for 24 hours before being placed in the chamber for 96 hours. Similar to SAC105, after 24 hours in the chamber, it is apparent that smooth surface morphology is displayed on Al-added SAC105. The surface improves as the Al content increases. The black patch on the surface is detected in EDX as carbon, possibly from the flux and cleaning residue. As the time of exposure is increased to 96 hours, the surface morphology of all samples except SAC105-0.2Al worsened, and the surface of SAC105 is apparently the worst. Interestingly, for all aged samples, the surface appeared to be unaffected after 96 hours of exposure.

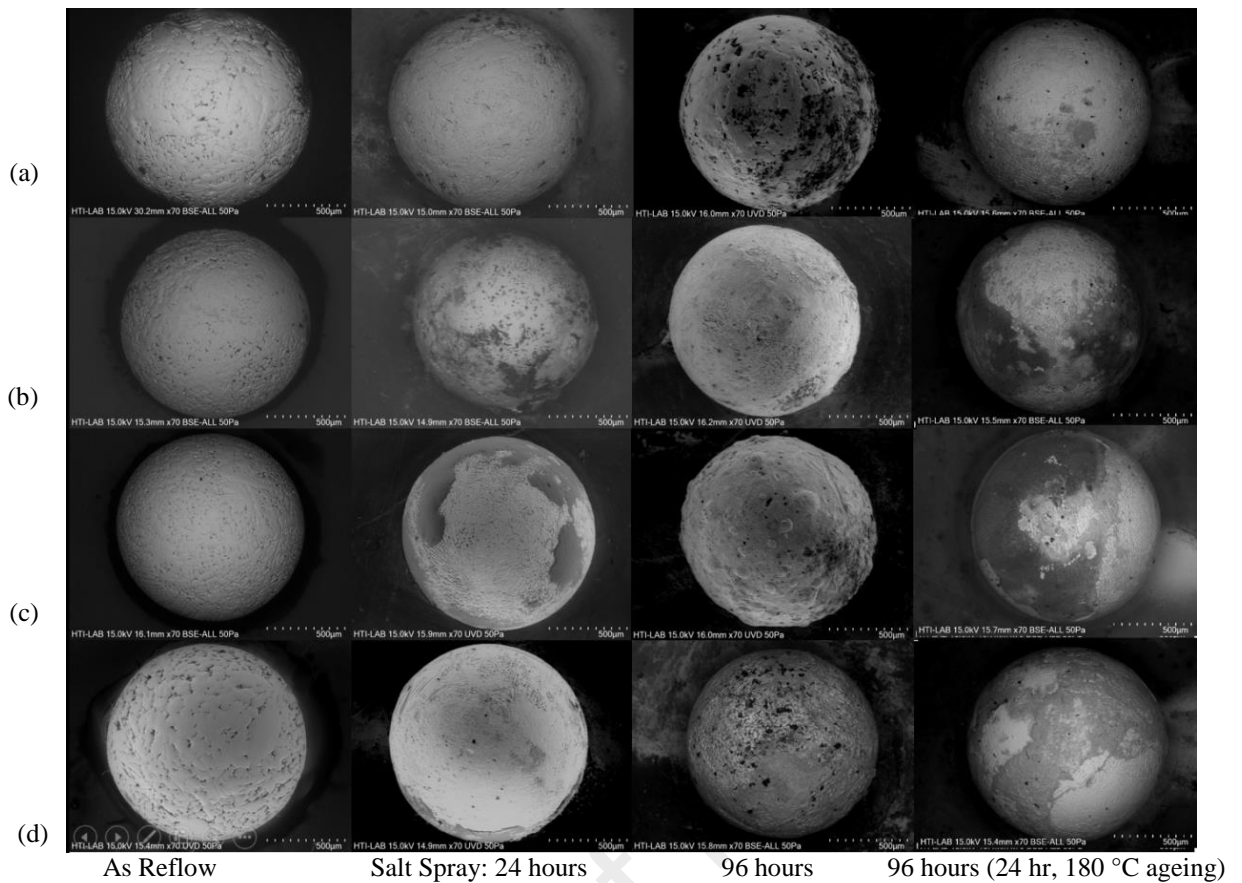


Figure 5.19: FESEM micrographs of a) SAC105, b) SAC105-0.2Al c) SAC105-0.5Al d)

SAC105-1Al solder balls as-reflow and after salt spray testing for 24 h, 96 h or 96 h + ageing in 180 °C

As seen in the surface morphology, as the addition of Al increases from 0.2 wt. % to 1.0 wt. %, the surface morphology degrades with a linear trend. The trend shows a correlation between time of exposure to NaCl and weight percentage of Al in SAC105. This correlation is associated with the inherent microstructure of the solder alloy. The most common cause of material spalling from the surface of an alloy is the unstable electromotive force (EMF) at the grain boundary between the adjacent elements within the microstructure of the alloy. During the salt spray test, dissolution occurs on the entire surface. After 96 hours of exposure, the solder ball surfaces of SAC105 and SAC105-1Al show the worst morphology. This indicates that only a very minor addition of Al to SAC105 will improve the passivation of the surface. This is because of the gravitational impact; during reflow, the solubility of 0.2 wt. % Al into 0.5 wt. % Cu and 1.0 wt. % Ag

occurs within the bulk, and the surface of the solder ball is mostly covered by Sn. Moreover, it has been found that the addition of Al suppresses the formation of Ag_3Sn and Cu_6Sn_5 (Maslinda et al. 2016; Leong et al. 2016; Shnawah et al., 2012). The impact results in more stability in terms of galvanic pairs with a solder matrix consisting of Sn. The large difference in galvanic potential could cause the dissolution of more active material between the pair. After some time, chloride attack leads to a thicker passivation layer and thus a smoothing of the surface.

For the poor surface morphology, the attack is considered a crevice corrosion, where the corrosion consumes only the crevice, where it enlarges, widens and merges. The addition of Al from 0.5 wt. % to 1.0 wt. % increases the formation of Al-Cu IMCs in the SAC105 microstructure. IMCs such as Ag_3Sn , Cu_6Sn_5 , AlCu and Al_2Cu have been found to be more inert than the solder matrix (Nordin et al., 2014; Wang et al., 2012; Wislei Riuper et al., 2012). Therefore, poor morphology is shown on the surface of SAC105 and SAC105 with added Al content of 0.5 wt. % and above. The instantaneous galvanic pair between these IMCs and Sn in the solder matrix creates instability between adjacent grain boundaries and accelerates material spalling off the matrix. However, from the surface morphology, SAC105 is more susceptible than Al-added SAC105.

The quantitative analysis of the investigation will be described in the next section, in which potentiodynamic polarization analysis was performed. The aim is to demonstrate the corrosion behaviour as a result of the local electrode formed by these IMCs within the Sn matrix.

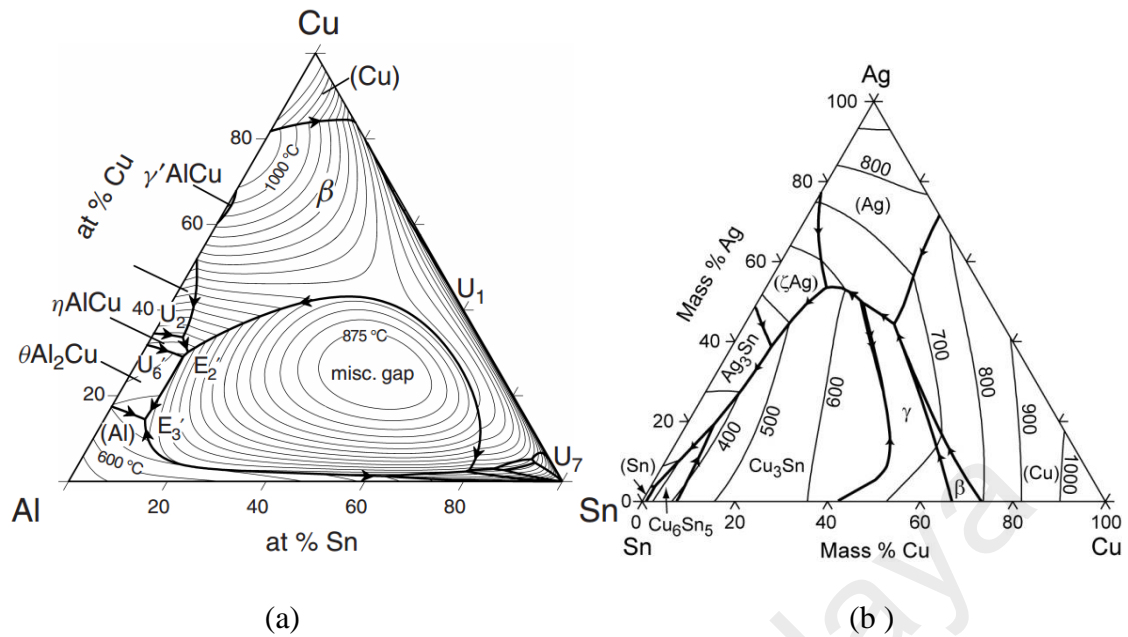


Figure 5.20: Phase diagram of (a) Al-Cu-Sn (b) Sn-Ag-Cu (ASM International)

Because Al has nearly zero solubility in Sn, the inclusion of Al in the Sn-Cu system has a tendency to result in the formation of an immiscible liquidous mixture of the molten solder (Campbel et al., 1956). This is related to the low capability of the alloy to form a homogenous mixture while in a liquid state. High homogeneity defines durable attributes of the mechanical properties of the material. For the ternary system, this low miscibility occurs only after the addition of Cu and creates a demixing of the liquid content (Mirkovic et al., 2007). As seen in Figure 5.20a, Al and Sn do not react, and in this system, the ternary liquid immiscibility could be an extension of the binary miscibility gaps in the Al-Cu and Cu-Sn systems. Low miscibility delays the formation of IMCs and creates poor metallurgical bonding with Sn in the solder matrix. This can be seen in Figure 5.21 on the surface of Al-added SAC105, which shows segregated Al-Cu, Al-Cu-Sn and Ag-Al IMCs dispersing within the microstructure. The similar microstructure of immiscible Al-rich resulting from Al addition to the Sn base and Sn-Ag-Cu have been reported by other researchers (Huang et al., 2014; Kantarcioğlu et al., 2014; Kamarudin et al., 2016; Leong

et al., 2016). The IMCs of Al-Cu and Ag-Al were most likely AlCu, AlCu₂ and Ag₃Al (Shnawah et al., 2012)

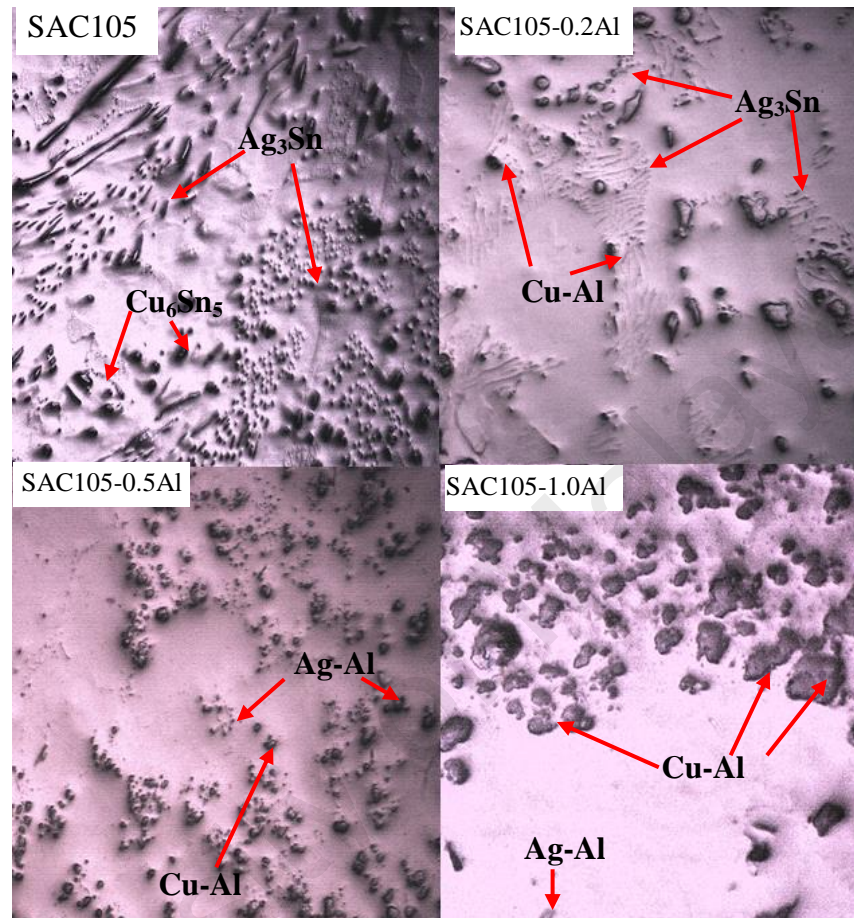


Figure 5.21: OM images of SAC105 and Al-added SAC105 solder alloys

5.3.1.1 Interfacial reaction as reflow

Data in Table 5.5 shows the comparison of the thickness of the Cu₆Sn₅ IMC layer between core SAC105 and SAC105-Al after soldering on Cu pads. The SAC105 possess thicker interface layer and the differences are 0.63um, 1.06um and 1.32 um as compared to SAC105 with added Al content of 0.2, 0.5 and 1.0 wt. %, respectively. There are some mechanisms that are possible to cause Cu₆Sn₅ IMC layer thickness suppression at the interface with Cu pads after Al addition. The correlation is probably during liquid/solid reaction.

Table 5.5 Intermetallic thickness at solder/substrate joint for as-reflow a)SAC105

b)SAC105-0.2Al c) SAC105-0.5Al and d) SAC105-1.0Al

Thickness (um)	SAC105	SAC105-0.2Al	SAC105-0.5Al	SAC105-1.0
As reflow	3.16	2.53	2.12	1.84

Firstly, reaction of Al and Cu to form Al-Cu interface or layer is higher than Cu-Sn. Al has higher solubility in Cu (Hanson et al., 1985). It competes with Sn and eventually caused Cu dissolution rate from the Cu pad to incline. The dispersed AlCu particles within the solder matrix is shown in Figure 5.21. Addition of Al in SAC105 has found to suppress the formation of Cu_6Sn_5 IMCs from the solder matrix. The suppression is due to the inclination of Sn to react with Al and form of AlCu IMCs (Shnawah et al., 2012; Kamarudin et al., 2016; Leong et al., 2016). This observation suggests that within the molten SAC105, Al is actively reacting with Cu. Furthermore, the inclusion of Al will instantaneously escalate the consumption of Cu from the solder matrix to achieve Al-Cu phase and therefore, the interface between SAC/Cu will experience a reduction in the concentration of Cu. As expressed in Eq. 5.1, where this scenarios will trigger the (Cs-C). Indirectly, the high dissolution of Cu interrupts the Cu/Sn reaction. Consequently, this causes the reduction on the reaction time that slows down the forming and growth of the Cu_6Sn_5 IMC layer. It could be deduced that Cu solubility in solder matrix increase after minor Al addition. Hence, during soldering the dissolved Cu from substrate formed precipitation of Cu_6Sn_5 in solder matrix than a layer at the Cu interface as it requires longer time and harder to exceed the solubility limit of the interface. As reported by Li et al. (2012), the Sn-based solders matrix with Al addition experience an increase of Cu concentration gradient.

Next, Al-Cu pair has a higher Gibbs energy (G) values which is 12.945 kJ/mol, compared to -7.630 kJ/mol of Cu-Sn. Thus, Al not only possesses higher solubility in Cu

but it also cause the Cu/Sn interaction to decline. The finding has a similarity when Al is included to the SnAgZn solder alloy (Cheng et al., 2002). The occurrence of phases involving reaction between Al and Cu for Sn/Cu interfaces and their thermodynamic stability rely on the volume and the Al concentration the solder (Xia et al., 2008; Kotadia et al., 2010). As reported by Xia et al. (2008), the initially Al/Cu phase was formed near substrate. However as the concentration of Al within the solder matrix deplete to less than 0.5 wt. %, the Al at the interface slowly diffuse into the bulk solder to retain the thermodynamic stability.

Additionally, the reverse dissolution rate of Cu_6Sn_5 IMC layer back into the matrix system is possibly higher compared to the rate between SAC105/Cu system itself. The SAC105–Al/Cu system possess higher Cu concentration gradient. In which, Cu_6Sn_5 in Al-added SAC is in higher concentration. Finally, Al that covers the surface of Cu_6Sn_5 grains as shown in Figure 5.22g might restrict further layer growth and acts as a barrier to the Cu_6Sn_5 grains coarsening. The blocking scenario halted the Cu atoms transfer between substrate and the liquid solder which in turn reduces the interfacial reaction and thickness.

5.3.1.2 Interfacial reaction after aging

Figure 5.22 (d,e,f) shows the cross sectional micrographs of isothermally aged SAC105 and Al-added SAC105 after 96 hours treated in salt spray chamber. The IMC layers shows more planar trend with the increase in Al content, after ageing for 24hours at 180°C temperature. The layers formed are the thick Cu_6Sn_5 and thin layer of Cu_3Sn . Through EDX analysis on the elemental ratio, Cu_6Sn_5 is the outer layer and the inner layer is Cu_3Sn with no Al inclusion on the layer was detected. The Cu-Sn ratio is shown in Figure 5.23 for both Cu_6Sn_5 and Cu_3Sn and the IMC thickness is plotted corresponding to the Al content. It shows that the addition of Al has a potential to produce a more robust solder alloy. This is due to the reduction in the thickness of IMC layer at solder joint often increases the joint strength. Because of the brittleness of the IMC interface layer, it often becomes the initiation spot for crack propagation. Cu_3Sn is known to be more brittle than Cu_6Sn_5 . Hence, for the ability of the SAC105 to keep the layer thin after the addition of Al will preserve the mechanical property to be similar as SAC105 in the application.

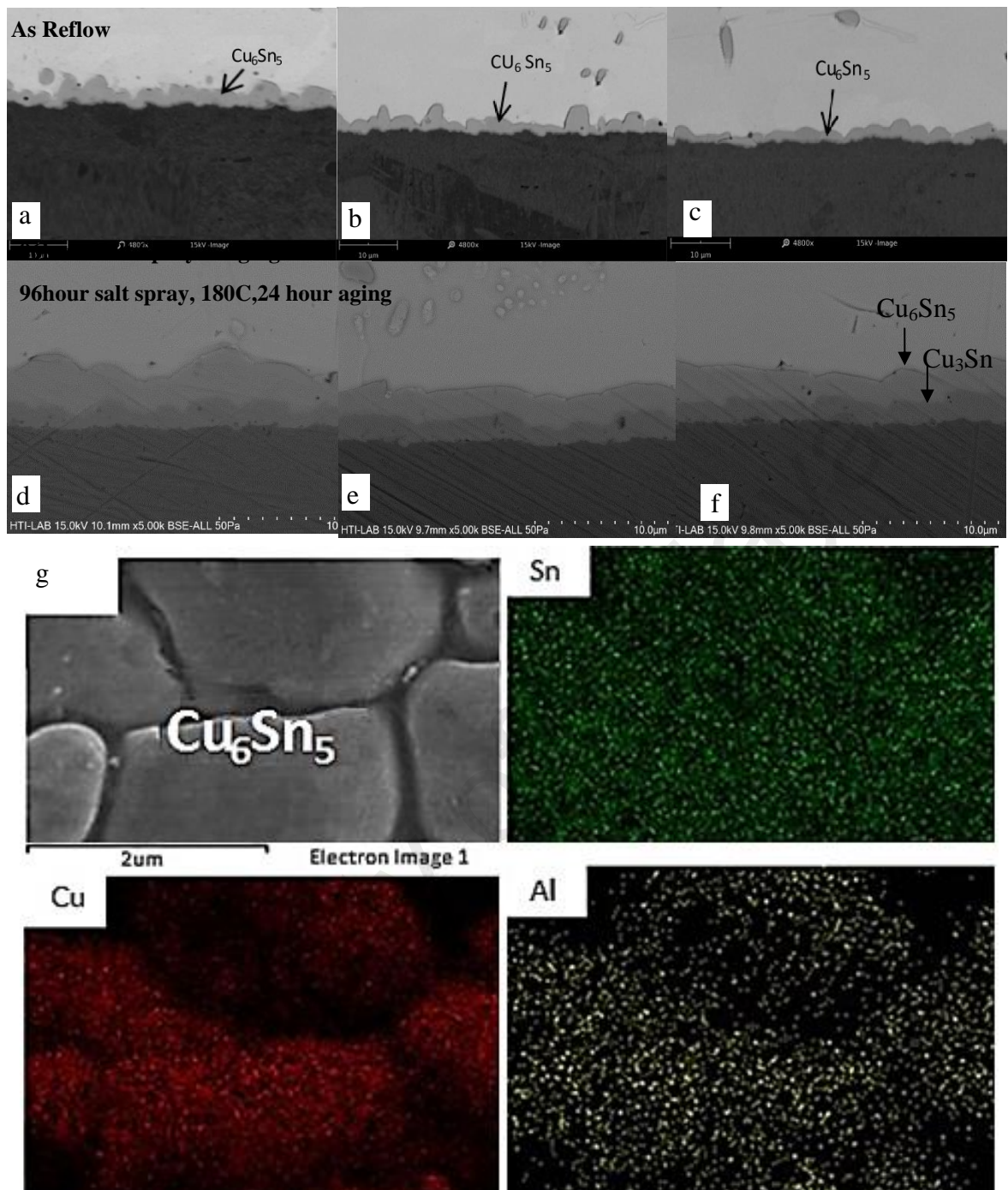
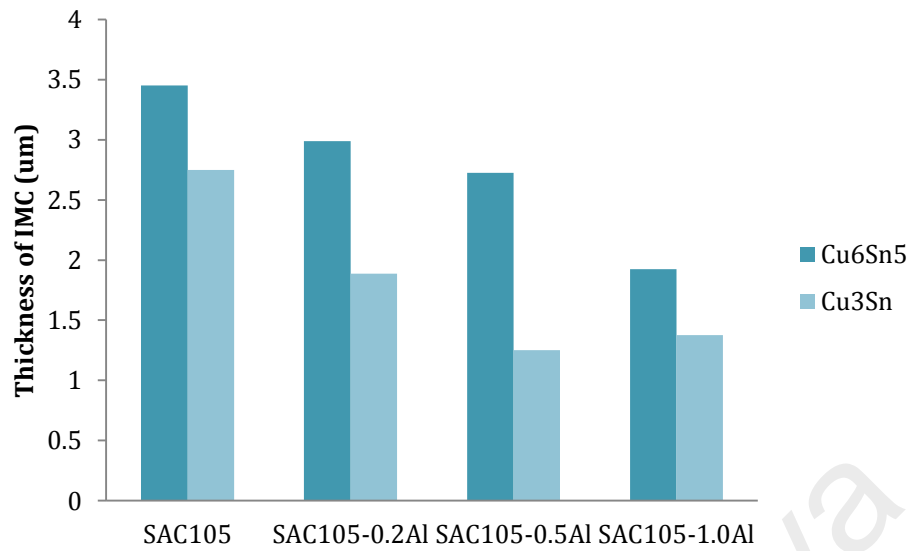


Figure 5.22: Cross sectional FESEM micrographs Al-added SAC105 (a-c) as-reflow 96hour salt spray test and 24 hour ageing at 180°C (g) element map for SAC105-Al solder alloy (Shnawah et. al., 2015)



Element (wt. %)	Cu ₆ Sn ₅			Cu ₃ Sn	
	Cu	Sn	Al	Cu	Sn
Spectrum 1	38.81	60.96	0.23	62.6	37.4
Spectrum 2	32.7	67.03	0.27	58.8	41.2

Figure 5.23: Variation of IMC thickness with Al addition after aging at 180°C for 24 h.

As observed for SAC105/Cu solder system after ageing, the IMCs are thicker than Al-added SAC105. Approximately 0.58um to 1.5um for Cu₆Sn₅ and 0.77um to 1.27um for Cu₃Sn IMCs. It was previously discussed that it is possible for an element addition to alter the interface layer growth. As the growth, is mainly due to the reaction of solid interface for tin based solders. However, the element should be able to adjust their stability by being soluble in the IMCs or for the solid Sn to change its reactivity (Amagai, 2008; Kotadia et al., 2010; Haseeb et al., 2011; Li et al., 2012). Otherwise it is impossible to affect the diffusion between Sn and Cu across the IMC layer as there is no energetic mechanism that triggers it. There are several scenarios that could be related to the mechanism that allows Al to suppress the IMC layer thickness growth.

Firstly, diffusion of Sn and Cu atoms through the Cu₆Sn₅ IMC layer is reducing with the existence of Al. Detection of low Al concentration was detected by the EDX

analysis in Figure 5.23 at the interfacial Cu_6Sn_5 IMC. Darken-Gurry (1953) had plotted the behaviour of elements by its electronegativity and atomic radius and found that Al and Cu possess very small difference. According to the plot, it is possible that partial substitution of Al into the Cu_6Sn_5 IMC layer occurred. As in the plot, Al is found not completely within the substitution ellipse of the plot. The partial substitution is expected to produce strain in the lattice of the Cu_6Sn_5 interface layer. As atoms of Al are relatively larger than Cu. Eventually, the mechanism is possible to promote a degree of reduction for the Sn and Cu atoms diffusion through the Cu_6Sn_5 IMC layer. Indirectly, it delays the reaction at $\text{Cu}_6\text{Sn}_5/\text{Sn}$ interface and in between $\text{Cu}_3\text{Sn}/\text{Cu}_6\text{Sn}_5$ contact. A similar study on fourth-element alloying using Zn, Co, Ni, Al, Mn and Fe substitution into interfacial Cu_6Sn_5 layer was developed by Anderson et al. (2002). However at this timeframe, the research still focused on soldering of high-Ag-SAC on Cu substrates. (Anderson et al., 2002; Anderson et al., 2004).

Next is on the possibilities of dispersing Al within the solder matrix blocking Sn reactivity. According to the EDX analysis in Figure 5.22g, the obvious element mapping of Al was found on Cu_6Sn_5 IMC grains surface. This implies that preferentially, Al stays on the IMC grains surface. Sn activity for interfacial reaction in the solder matrix is reduced by the existence of Al. The blocking effect introduced by Al results in suppressing the diffusion of Sn through IMC layers (Cu_6Sn_5 and Cu_3Sn). It is important to note that Al/Sn has near zero solubility at temperature below 200°C (Murray, 1990). The growth of Cu_6Sn_5 and Cu_3Sn IMCs were interrupted by Al solute atoms that occupy the lattice sites and obstructed diffusion process and significantly cause the declining of Sn or Cu supply for IMC layer growth.

Additionally, the growth of the interfacial layers was reported to be controlled by the diffusion of Sn at temperature around 60°C and 200°C (Oh, 1994; Yu et al., 2005; Laurila et al., 2009). The growth of IMC layers at high temperature ageing was slightly

affected by the diffusion at grain boundary as it is too quick and short interval for the entire growth process (Laurila, Hurtig, Vuorinen, & Kivilahti, 2009; D. Q. Yu et al., 2004). The Cu atoms diffusion from Cu substrate into liquid solder is restricted by Al that exist on the Cu_6Sn_5 grain.. Under this condition, layer growth is predicted to be prompted by the diffusion of volume. Rationally, as temperature elevated, volume diffusion starts and the role of Cu grain boundary diffusion become insignificant. At this temperature range, possibly the Cu_3Sn phase continual growth occurred at the Cu_6Sn_5 phase expense. Nevertheless in this study, as shown by the EDX analysis mentioned in Sect. 5.3.1.1, evidence of Al presence in the grain boundary of Cu_6Sn_5 grains has yet to be proven. So, this mechanism for suppressing the interfacial IMC is still open for discussion.

Finally, the growth of Cu_6Sn_5 is possible from the effect of dispersing Cu_6Sn_5 IMC particles within the bulk solder and nearby the Cu_6Sn_5 IMC layer. Ageing of SAC solders often creates IMC coalescence and increasing growth. However, Al-added SAC solders were found to suppress and refined all other IMC particles within the SAC105 alloy. Collectively, from this study and other previous researches, Al addition in SAC lead-free solder retain the solder/substrate joint properties at the interfacial layer and the ductility of the at bulk solder. The Al-added SAC105 solder alloy had also exhibit its potential to lower the IMCs growth rates at substrate, due to isothermal ageing. The reliability of soldering at joint in commercial devices for SAC containing Al, specifically on the impact of its high oxidation property require further probing

5.3.2 Materials corrosion behaviour in potentiodynamic polarization

Figure 5.24 presents the polarization plot SAC105-x%Al solders with $x = 0.1, 0.5$ and 1.0 wt % of Al contents, immersed in 5% NaCl solution. The anodic part in the figure was breakdown into five sub-regions which are A to B, B to C, C to D, D to E, and E to F. As the tests were performed in aerated condition, the cathodic section represents reduction

reaction that produce hydroxides (OH^-) (Oulfajrite et al., 2003; Mohanty et al., 2013). The numerical data from the polarization curves of all of the materials were extracted and are summarized in Table 5.6.

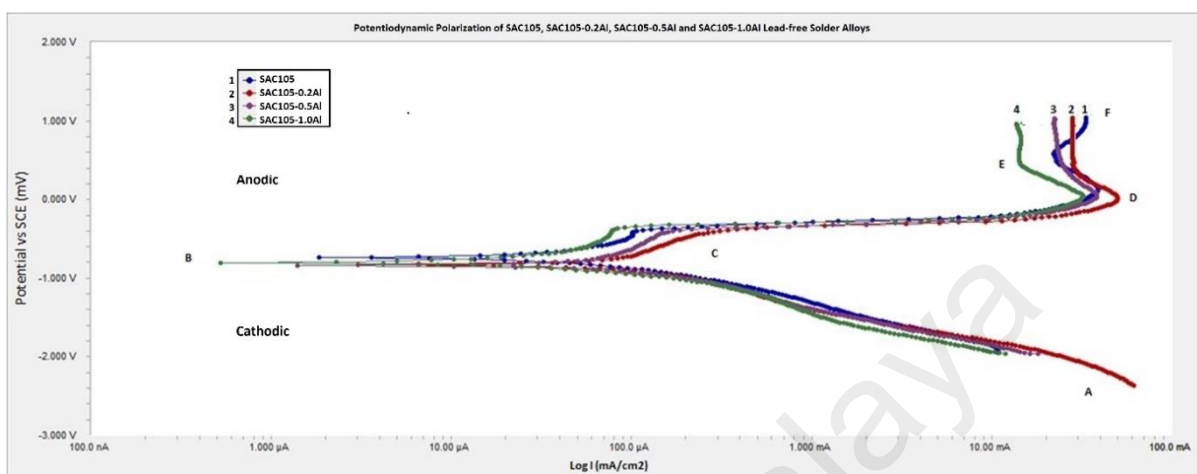


Figure 5.24: Corrosion behaviour of Al-added SAC105

A further increase in potential up to point B resulted in a sharp peak, which might be attributable to the dissolution of Al. The addition of OH^- ions to NaCl solution increased the anodic dissolution rate of Al. As shown in Table 5.2, Al is the most anodic and therefore will be attacked preferentially by the OH^- . The Al content of the SAC105 alloy varied from 0.2 wt% to 1.0 wt%. The polarization curves obtained for the alloys showed an active-passive transition at points A to B to C, followed by a transpassive region at points D to E.

The active dissolution of Al continues with increasing potential until the corrosion products supersaturated the surface of the alloy (point C in Figure 5.25). The SAC105 alloy with higher Al content showed a strong tendency towards passivation, given that the passivation current density (i_p) was found to be lower than that of SAC105. This passivation behaviour was attributed not only to the presence of SnO and SnO_2 but also to the nature of Al to generate passivity film on the surface. The addition of 0.2 wt% Al results in a decrease in the corrosion current density (I_{corr}). However, the addition of ≥ 0.5 wt% Al resulted in higher I_{corr} , as listed in Table 5.6. In addition, the corrosion potentials

(E_{corr}) shift towards more negative values. Similar to I_{corr} , a decrease in corrosion rate was observed for addition of 0.2 wt% Al, and the highest corrosion rate was found for the alloy with 1.0 wt% Al. The presence of Cl^- ions initiated crevices and pitting spots and was assumed to be responsible for the rupture of the passive layer at the breakdown potential (E_{BR}), which is approximately at -0.4 mV vs. SCE. The E_{BR} values are of approximately the same magnitude for all of the materials in this study.

Table 5.6: Results for corrosion potential, current density and corrosion rate

	Ecorr (mV)	Icorr (μA)	Corrosion Rate(mmπy)
SAC105	-741.6	70.8	2.302
SAC105-0.2Al	-804.7	53.64	2.013
SAC105-0.5Al	-838.3	83.9	2.73
SAC105-1.0Al	-830.6	79.27	3.29

In Figure 5.24, all of the samples' passivation processes begin at -800 mV and extend to -400 mV vs. SCE. This is probably due to the formation of tin oxide (SnO_2), which disappears at -400 mV when an abrupt increase of anodic current density occurred because of the breakdown of passive layers on the surface at E_{BR} . This rapid increase in anodic current density results in an obvious x-direction (increase in current) of the curve, corresponding to the active dissolution of Sn stimulated by the Cl^- ions, with the formation of soluble complexes of the type SnCl_2 . One point that should be noted is that Sn is an anode in this electrochemical reaction and will always react with Cl^- to form SnCl_2 , which is soluble in aqueous solutions.

At points D through E, the current density slowly starts decreasing with further scanning in the anodic direction. When the potential increased, the current remains independent, indicating the onset of a pseudo-passivation process attributable to the

formation of a corrosion film on the surface (Guedon Garcia et al., 2016; Khireche et al., 2014; Rosalbino et al., 2008). At this point, this current is known as the pseudo-passivation current density, i_{pp} . As shown in Figure 5.24, the i_{pp} values of all of the materials are in the range of 10 mA to 60 mA, whereas the pseudopassivation potential (E_{pp}) range extends from +200 mV to +600 mV vs. SCE. Moreover, the i_{pp} for SAC105 is approximately 0.2 mV higher than that of Al-added SAC105.

At point E, eminence performance occurred, in which the alloys with Al supersede SAC105. As observed, current density was not influenced by the increase in the trans-passivation potential for alloys with Al. For SAC105, the increase in trans-passivation potential increases the current density. This scenario is directly related to the passivation layer on the surface of the material in the pseudo-passivation region. For SAC105, the increase in the trans-passivation potential induced shattering of the passivation layer, whereas for the Al-added SAC105, the layer persistently sticks on the surface until the scanning ends. This finding suggests that the formation of the oxide film on the surface inhibited the reaction with Cl^- ions. This oxide film is responsible for the suppression of pitting corrosion for all of the Al-added SAC105 alloys whilst protecting the larger part of the exposed area.

Regarding exposure to salt spray, all of the assembled samples exhibit tolerable and almost equal reactions to Cl^- ions. In addition, examination of IMC has shown no visible cracks caused by the penetration of Cl^- . However, the potentiodynamic polarization curves showed that Al-added SAC105 alloys are more reactive and have higher E_{corr} , eventually leading to a higher corrosion rate. Moreover, towards the end of the polarization, Al-added SAC105 solder alloys are more stable and the increase in voltage does not affect the current. This performance is best explained by Figure 5.25. The Al-added SAC105 has more densely packed corrosion products on its surface, whereas SAC105 was covered with a flake-like layer that obviously offers numerous weak spots for attack by the aggressive

Cl⁻. The difference was ascribed to the additional layer of oxides, which are shown in XRD analysis (Figure 5.25). The inclusion of Al in SAC105 introduces oxide layers in the form of Al₂CuO₄ and Al₂O₃. These oxides layers add up to the surface protection provided by the major SnO and SnO₂. Thus, Al addition altered the corrosion products on the surface of the solder alloy. The formed products offer better resistance to the aggressive Cl⁻ through the arrangement of firmer layers on the surface of the material to block reaction with corrosive agents in the environment. A good correlation is obtained between the results found by salt spray exposure, potentiodynamic polarization and SEM for the characterization of electrochemical behavior of Al and its alloys.

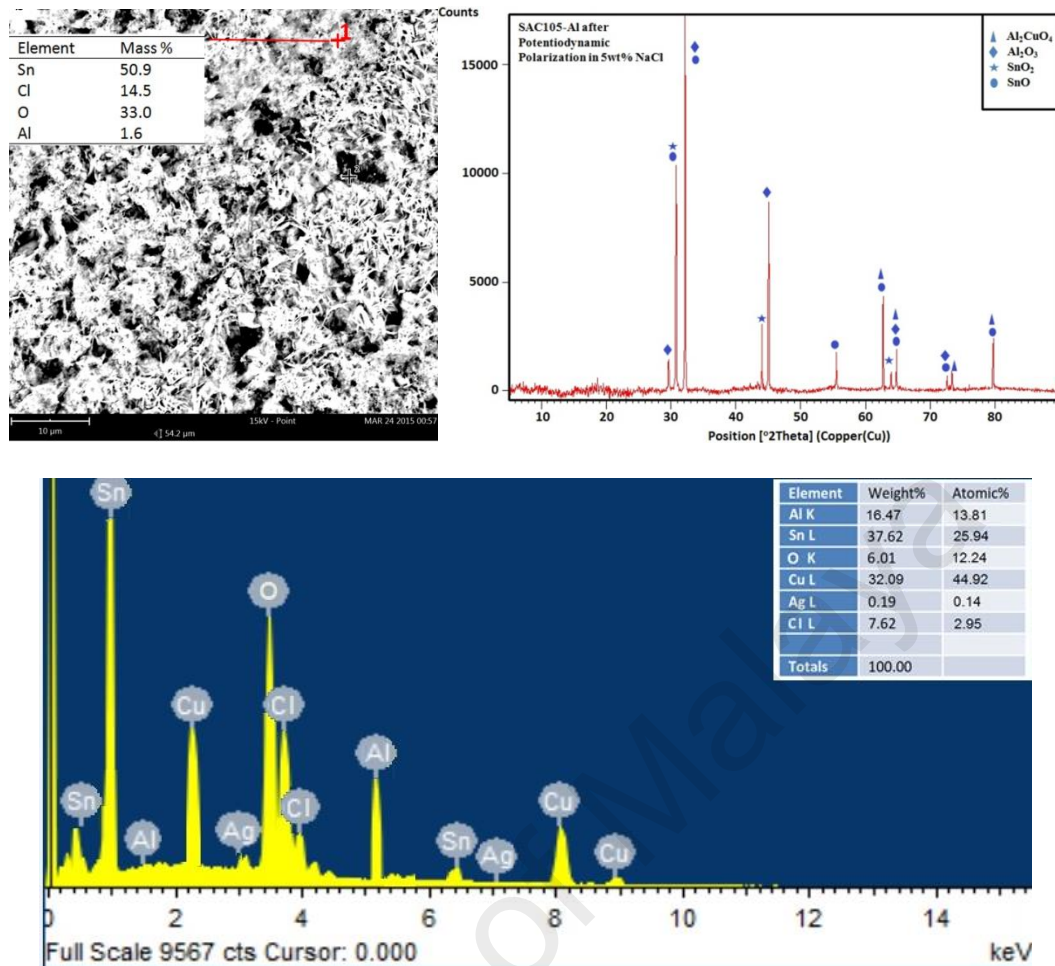


Figure 5.25: FESEM micrograph (10 µm magnification), XRD and EDX analysis of the corrosion behaviour of Al-added SAC105

5.3.3 Shear Strength of Solder Ball/Cu Joint Interface

The inclusion of Al in SAC105 substantially alters the microstructure. The main role of solder alloy is to act as not only an electrical and mechanical interconnect but also a thermal conduit. The alteration of IMC content within the microstructure has the potential to either improve or reduce the joint strength. This is due to the brittleness of the IMCs. Though the size of the IMCs is too small per particles, it expands as it forms a layer at joint interface with the substrate. Additionally, its morphology and distribution is significant to the mechanical properties with accumulated stress and strain endure by the solder joint. Eventually influencing the solder joint reliability (Henderson et al., 2001; Chen et al., 2011). A phenomenon resulting from the concentration of stress at the bottom of the solder

bump is possible during reflow. Shear will cause the solder bump to disintegrate from the copper pad when a micro-crack is initiated near the shear tip. The micro-crack begins to grow only after the applied stress exceeds a certain level, at which point the crack begins to open.

Figure 5.26 presents the shear strength of SAC105 and Al-added SAC105 after reflow, after 24 and 96-hour salt spray tests and after ageing of 96-hour samples for 24hour at 180°C. The shear strength of after-reflow samples showed that all Al-added samples displayed reduced shear strength compared to SAC105. However, the strength increases with Al content, although the overall magnitude is lower than that of SAC105. Conversely, Al-added SAC105 has higher shear strength in 24- and 96-hour samples, albeit in a decreasing trend as Al content increases. Combining the impact of salt spray and thermal ageing shows that the highest Al content is associated with the lowest shear strength. Other samples demonstrate comparable performance to the core solder alloy, the SAC105.

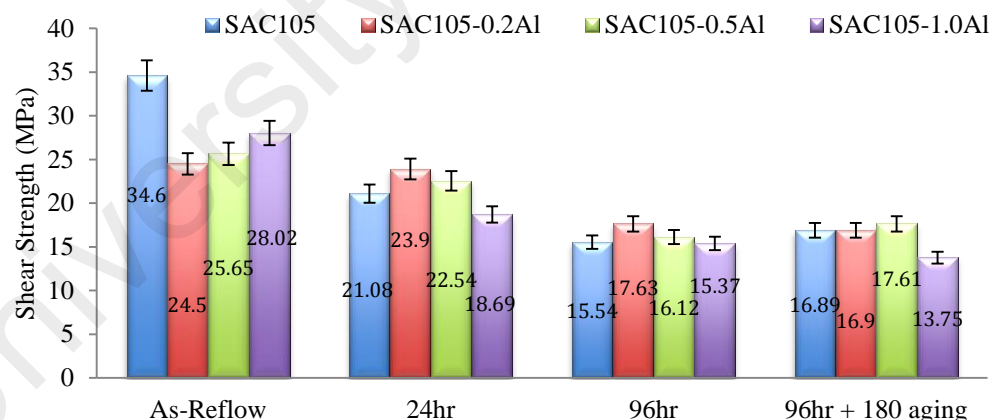


Figure 5.26: Shear strength of SAC105-xAl solder ball interconnect before and after salt spray testing and after ageing

It is postulated that the large IMC particles precipitate across the joint is possible to induce cracking. The solder matrix and interfacial strength of a solder joint determine the adhesions shear strength. Generally, lower solder matrix strength will induce ductile failure

while brittle failure occurs when bulk solder strength is higher (Tong et al., 2003). The bulk solder determine the solder strength. Meanwhile the strength of joint at substrate defines the interfacial joint strength. The grain size and the distribution of IMCs within the bulk solder are the factors that affect the strength. Smaller grain size increases the joint strength. This is due to smaller grain size increase grain boundaries that provide new path that eventually obstruct the dislocation motion and crack propagation. The governing equation that shows the correlation between the strength of material and grain size is obtained in Hall–Petch relation below (Callister and Rethwisch, 2012):

$$\sigma_y = \sigma_0 + \frac{k_y}{\sqrt{d}} \quad (5.13)$$

In Eq (5.13), σ_y is the yield stress, σ_0 is a constant for material dislocation motion resistance, k_y is the strengthening coefficient and d is the grain diameter. From this equation, smaller grain size will induce higher yield stress and vice versa. It was reported that microstructure of Al-added SAC105 possess smaller β -Sn dendrites SAC105 (Shnawah et al., 2012). Therefore, theoretically SAC105 with Al addition should be stronger. However, contrary to Eq. 5.13, finer β -Sn dendrites of Al-added SAC105 solder alloys possess lower shear strength. Typically, cracks initiate and propagate along the interface at substrate and the existence of the Al-Cu IMCs often reduces ductility at bulk region and joint (Kamarudin et al., 2016; Kah et al., 2015; Shnawah et al., 2012). The governing mechanism is related to the point discussed in section 5.3.1 on the immiscibility of Al-added SAC105. The alloying of SAC105 with Al formed weak bonds between Al inclusion IMC particles and the solder matrix. Hence, allowing lower stress to initiate crack and progress until complete rupture.

Furthermore, the distributions of the IMCs within the bulk solder often create barriers for dislocations. The precipitation strengthening mechanism eventually increases the strength. On the other hand, it could also provide a weak spot for IMC/solder matrix

metallurgy bond. Nevertheless, the findings are in agreement with Alam et al. (2009). It was reported that the ball shear strength of solder alloy falls in the range of 10–25 MPa,. This relies on the composition of solder alloy, ageing condition and also the finish material used on the substrate.

5.3.4 Fracture behaviour

Although are various possible reasons for these findings, it is believed that the low immiscibility and demixing of the molten solder of Al-added SAC015 solder alloys reduced the strength of the solder bump. This liquid-solid transition mechanism creates a weaker interface between formed IMCs and the solder matrix, which eventually has a tendency to easily form voids along the grain boundary. The weak interface and formation of micro-voids in the solder matrix will decrease the interfacial strength (Alam et al., 2009) since the solder is not perfectly soluble and does not undergo solidification to form a strong metallurgical bond. Nevertheless, the shear strength is approximately comparable to those of the SAC105 and Al-added SAC105 solder alloys. This is evident because the shear fracture for all of the samples tested shows a ductile fracture mode. The solder residue is left on the substrate after the solder ball is ruptured. These voids are noticeable in Figure 5.27. In addition, the formation of Al–Sn–Cu IMC could be the reason for the reflow samples. This decreasing shear strength of Al-added SAC solder alloys has also been reported by Kantarcioğlu and Kalay (2014).

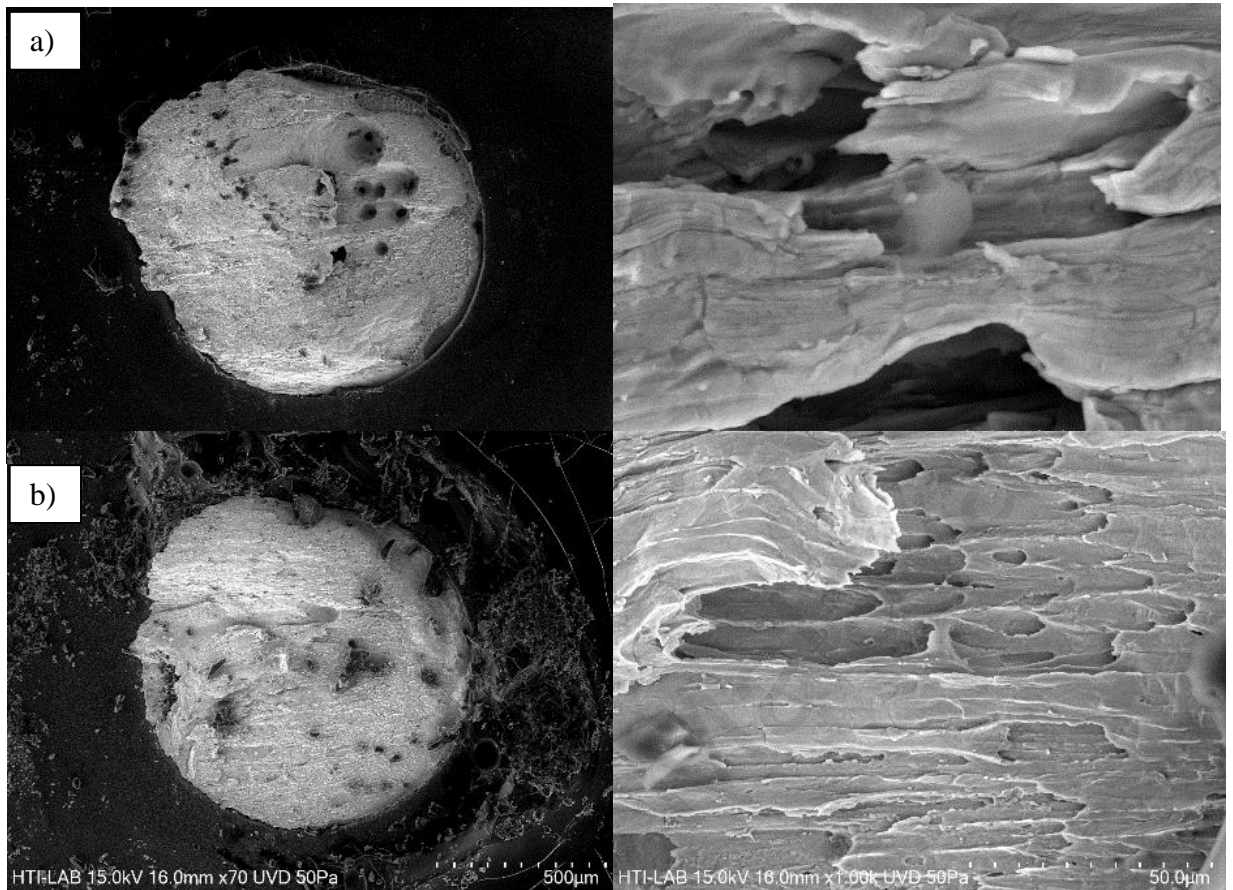


Figure 5.27: Shear fracture of h of SAC105-xAl solder ball interconnect, a) before and b) after salt spray

5.4 Finite element analysis

Because of limitations of laboratory capability and reliable material fabrication, the experiments on the solder/substrate shear strength were conducted on 1.2 mm-diameter solder balls. This diameter is much bigger than the size used by industry. Hence, FEA is used to predict the joint strength of lower-diameter solder balls to simulate the practical use of the material in soldering.

5.4.1 Model validation

Before proceeding towards the objective of the simulation, which is to calculate the joint strength of smaller solder balls, the solid structure and model use are validated. A proper and accurate geometry structure was carefully meshed to enable the model to calculate a result close to that of the experiment. By substituting the material properties in Eq. (5.14), in which ε is the total strain displacement, ε_e is the elastic strain and E is the elastic modulus, the stress versus total strain response can be calculated.

$$\varepsilon = \varepsilon_e + \varepsilon_p \quad \varepsilon = \frac{\sigma}{E} \quad (5.14)$$

Figure 5.28 illustrates the correlation between the model predictions for the stress-strain curves and the experimental data of the considered multilinear isotropic data. In all cases, good correlation is obtained, indicating that the model parameters provide a good fit with the experimentally characterized response. This correlates with the shear stress, which, in this study is the ratio of the force to the pad area. Theoretically, because the elastic modulus (E) and Poisson's ratio (ν) are constant in the FE simulation, the shear modulus (i.e., μ and $\mu = \frac{E}{2(1+\nu)}$) of the solder joints is also constant. However, smaller-dimension solder joints will have higher shear stiffness. This implies that they are more difficult to

deform. This statement will be assessed in the next section by simulating a smaller-diameter solder ball.

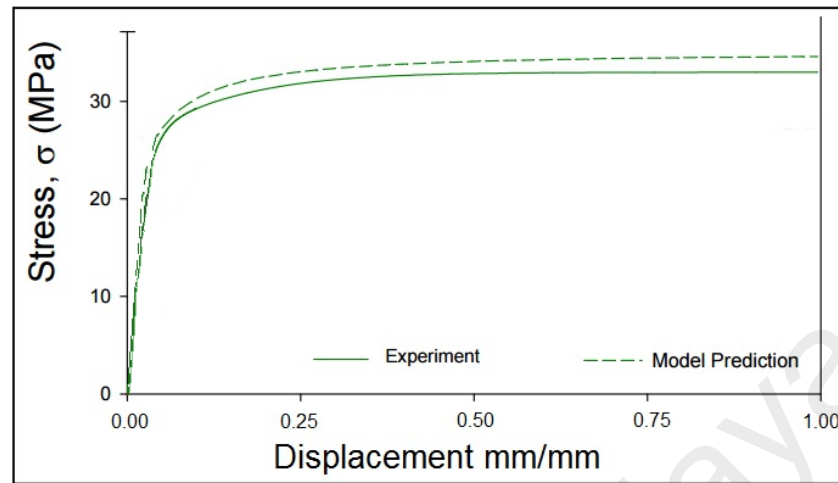


Figure 5.28: Correlation of the Model Predictions with Experimental Stress-Strain Curves for SAC105

5.4.2 Size impact of solder joint strength

The desirable good agreement of the initial model and experiment data has allowed the study to progress to the next level. Initially, the validation was using structure of the biggest solder ball dimension. In this section, further clarification on the shear fatigue mechanism will be discussed. Following this, solid structure of the model will go down to smaller solder ball with diameters 760um and 450um. The study will focus mainly on the equivalent stress of the solder joint under shear load.

The averaged equivalent stress analysis was accomplished to obtain the failure mode of the solder ball with shear test. The load on the pad during a shear test is a combination of shear, tensile and also the compressive forces. The significant impact is at the edge of the solder (Lee et al., 2003). Figure 5.29 plots the distributed averaged equivalent stress endured by the solder joint. As observed, region in the solder ball that is near the shear ram

to solder contact point shows the highest stress. The stress expansion is in parallel to the substrate. This is in agreement with the experiment and theories that crack initiation and growth is through this region. The cross-sectional view of the solder ball shows that the fracture mode is ductile type, similar to finding by other research on SAC solder alloys (Yoon et al., 2003; Shnawah et al., 2012, Kumar et al., 2013; MahdaviFard et al., 2015; Kamarudin et al., 2016). Apparently, sheared Cu pad was covered with residual solder which is the evident of a ductile fracture mode. This was mainly caused by the effect of 20 μ m height of side wall that is supporting the Cu pad adhesion on the FR4 board and also the solder joint at area A. A similar result on initiation of crack near the solder area in contact with the shear tip was also reported. The highest plastic strain was calculated and the contour had expanded along the substrate. (J.-W. Kim & Jung, 2006). By comparing both images in Figure 5.29, the shear mode of failure of solder ball joint determined by both computational analysis and the actual experiment correlates to each other. Another good agreement between experiment and simulation with the one discussed in Section 5.4.1. It is worth to note that in the experiment, all of the test specimens from base and element added SAC105 solder alloy exhibited similar mode of failure and the fracture mode shows ductile property of the solder alloy.

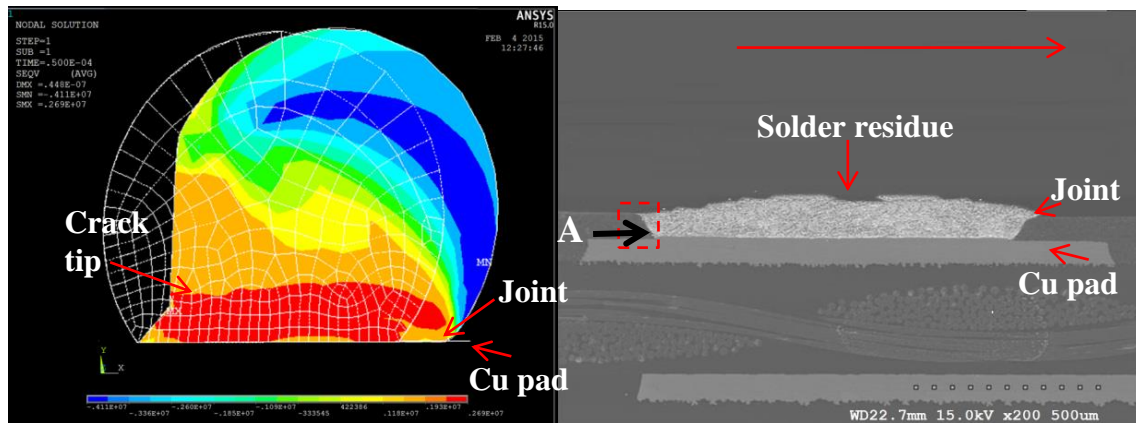


Figure 5.29 Contour plot of an average equivalent stress analysis and the cross-sectional view

The computational modeling attempt to simulate the shear strength with a function of reducing solder ball diameter. Experimentally, for 1.2 mm solder ball diameter, 20 solder balls were sheared to failure. As tabulated in Table 5.7, it shows that the reaction force is proportional to the solder ball diameter and marked the lowest value for the smallest solder ball diameter. This means that the decrease with reducing diameter is mainly due to the dimension of the solder and the corresponding strength of the Sn matrix with dispersed IMC within the bulk rather than the IMC interface layer at the solder joint. This is due to the residues of solder which was still remaining on the pad after the ball is fully ruptured.

Table 5.7: Surface area, reaction force and Shear Strength of 1mm, 760 μ m and 450 μ m solder SAC105/Cu solder joint

	Experiment	Solder Ball Diameter		
	1.2	1.2	0.76	0.45
Area		1.13	0.45	0.16
Simulated reaction force (N)		53.7	23.3	5.33
Shear Strength	23	20.74	20.67	21.83

On size effect, it is assumed that the relation of Cu diffusion characteristics in molten solder obeys Fick's second law. The Cu solubility limit in liquid solder at 250°C for the interface in SAC/Cu₆Sn₅ is 1.5 wt.% (Moon et al., 2002). During soldering, the approximation of the average diffusivity, D of Cu atoms in molten solder $2.5 \times 10^{-9} \text{ m}^2/\text{s}$.

Figure 5.30 presents the 3D slices of the simulated contour stress in SAC105 solder ball with different diameters. Smaller solder ball (450µm in diameter) marked the lowest reaction force while larger diameter solder ball produced the highest reaction force. Due to smaller solder balls has lower impact area than higher diameter solder balls. Additionally, the volume of a ball is third power of its diameter, hence more force needed to shear the bulk solder from the adhesion interface.

The computational results indicate that the shear force decreased with reduction of solder ball diameter. This supports that there is a direct consequence between material properties and the geometrical dimension of the solder ball. However, it should be also noted that, the shear strength at the solder joint remain as is and is not affected by its dimension. The mismatch between the experimental and computational results is ascribed to the confined contact area between the shear ram and solder ball surface and the meshing set for the structure in ANSYS.

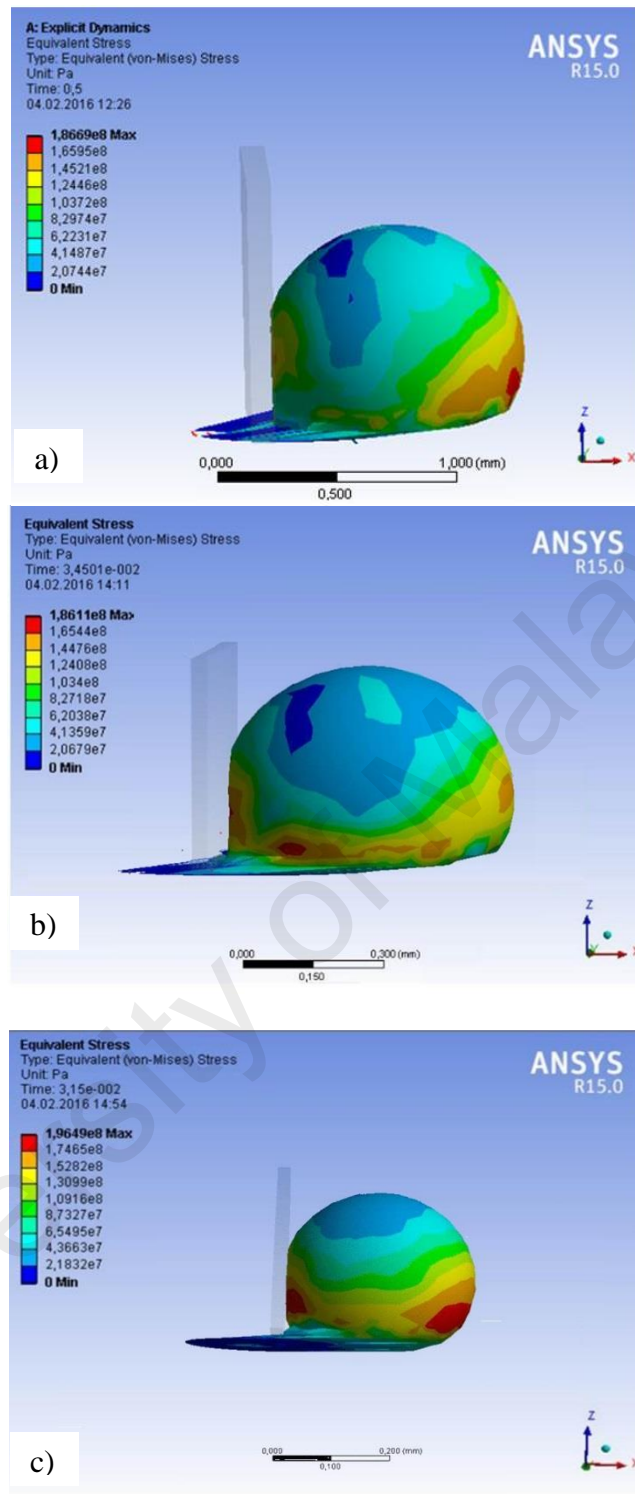


Figure 5.30: Equivalent stress distribution for different solder ball sizes of SAC105 with solder ball diameter of (a)1.2mm (b)760um (c)450um

In material perspective, smaller solder balls have thicker interfacial Cu_6Sn_5 layers ratio to the bulk area compared to the larger diameter solder balls and also has less

consumptions of Cu. The Cu_6Sn_5 is the intermetallic layer that defines the strength at the SAC105/Cu solder joint. Figure 5.31 presents the visual of the mechanism during soldering. At the starting of the soldering, the thickness of interfacial Cu_6Sn_5 layer rise abruptly as the dissolution of Cu between substrate and liquefied solder is high. However, the layer growth declining after the initial ramp due to increase of Cu_6Sn_5 grains formed as the constrain J_{in} starts, while J_{out} remains large since the bulk area remains active in dissolution reaction and hence the continuous concentration gradient persist for Cu dissolution. This is more significant for higher diameter solder spheres. With time, growth rate reduce as effect of continuously thickening of interfacial layer formed by Cu_6Sn_5 . This eventually cause a drop between J_{in} and J_{out} .

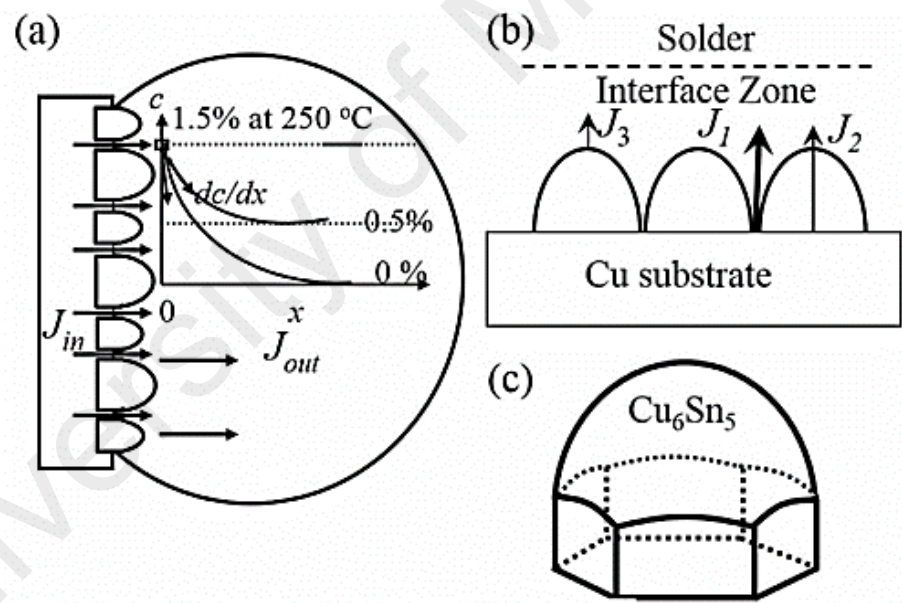


Figure 5.31: Interfacial layer initiation mechanism in soldering (Huang et. al., 2015)

5.5 Summary

This study observed the impact of the fourth element, Fe/Al, on the ternary Sn-Ag-Cu solder alloy system. The addition of these elements was expected to alter the microstructure, the surface morphology, the reaction at the substrate interface, the ability to sustain ageing and the mechanical properties. Because of the difference in the inherent corrosion resistance of Fe and Al, the study was extended to investigate that impact. Samples for reflow and after a 5% NaCl salt spray with or without 24 hours of ageing under 180 °C was tested; the results were analysed and discussed.

The microstructure of SAC105 with the addition of Fe/Al has been observed. The inclusion of Fe/ Al immensely altered the microstructure of SAC105. The addition of Fe introduced FeSn₂ precipitation within the bulk solder alloy, suppressed the formation of Cu₆Sn₅ and refined the Ag₃Sn. High susceptibility towards corrosion was seen, as the material was exposed for 96 hours in a corrosive environment. Al-added SAC105 formed AlCu and Al-Cu-Sn IMCs that are dispersed within the bulk solder alloy. The increase in Al content completely suppressed the formation of Ag₃Sn and Cu₆Sn₅ from the solder bulk. This results in a remarkable surface morphology that indicates high corrosion resistance. The addition of Fe/Al was found to suppress the formation of a thick Cu₆Sn₅ IMC interfacial layer. The solder/substrate joint layer was observed to be more planar and refined as the Fe/Al content increases. Overall, SAC105 has a thicker IMC interface layer compared to Fe/Al-added SAC105. It was observed that after ageing, the reaction product is always Cu₆Sn₅ and Cu₃Sn phases formed at the interface with substrate. The interface layer morphology evolved from a scalloped pattern to more flat surface. The susceptibility of Fe-added SAC105 solder alloys was found to be similar to that of SAC105. Conversely, there were densely packed corrosion products on the solder ball surface because the impact of Al inclusion in SAC105 created a more corrosion-resistant solder material. Fe/Al-added

SAC105 had thinner IMC layers that decreased as a function of increasing Fe/Al content. However, a linear reduction in shear joint strength was observed with an increase in Fe/Al content. A computational simulation was projected for the impact of miniaturization; it calculated that the reaction force is proportional to the solder ball diameter and marked the lowest value for the smallest solder ball diameter. As the reaction increased with the increase in solder ball diameter, the shear strength was approximately the same magnitude as the shear stress, which was proportional to the force loaded but was inversely proportional to the dimensions of the joint.

CHAPTER 6 : CONCLUSION

6.1 Conclusion

In this work, investigations on Fe/Al addition in SAC105 ternary low Ag solder alloys focuses on three main parts: (1) To study the effects of Fe/Al as minor element addition on the interfacial reaction at joint, (2) To characterize the corrosion behavior of the SAC105 with addition of Fe/Al , and To evaluate the shear behavior of solder joint minor element added SAC105/Cu solder joints. This chapter concludes all the findings and will map the outcome to the existing findings.

The study observed on the impact of the fourth element, Fe/Al, on the ternary Sn-Ag-Cu solder alloy system. The addition of these elements was expected to alter the microstructure, the surface morphology, the reaction at the substrate interface, the ability to sustain aging and also the mechanical properties. Due to the contradicting of the Fe and Al inherent corrosion resistance, the study also was extended to cover on this impact. Cross section of the samples for as reflow and samples after 5% NaCl salt spray test and 24hour under 180°C aging were performed and results were analysed and discussed.

The microstructure of SAC105 with the addition of Fe/Al has been observed. The inclusion of Fe/ Al had immensely alter the microstructure of SAC105. A few highlights were discussed and correlated mechanism that could cause the microstructure alteration were presented. The addition of Fe had introduce FeSn_2 precipitation within the bulk solder

alloy and suppress the formation of Cu_6Sn_5 and refine the Ag_3Sn . The resulting surface morphologies were close to SAC105 but tremendous susceptibility towards corrosion were seen as the material is exposed 96 hours in a corrosive environment. The spalling off of material from the solder matrix, as the impact of corrosion, revealed the Ag_3Sn and FeSn_2 IMCs at the spot where the mechanism occurred. These two IMCs were concluded as the dominant EMF instability triggering agent within the SAC-Fe system. Whereas Al-added SAC105 formed AlCu and Al-Cu-Sn IMCs that are dispersed within the bulk solder alloy. The increase in Al content had suppressed formation of Ag_3Sn and Cu_6Sn_5 totally from the solder bulk. This results in remarkable surface morphology that indicates high corrosion resistance. There are still limited data available in literature that could be compared to the performance of Fe/Al addition in SAC105. Table 6.1 lists the recent findings of corrosion properties of SAC105 with minor element addition with parallel information from higher Ag content SAC alloys.

Table 6.1 Corrosion potential and current with the corrosion rates of SAC solder alloy

Solder System	E_{corr}	i_{corr}	CR (mm/year)	Source
SAC105	-810	4.6	122.6	(Mohanty & Kwang-Lung, 2007)
SAC205	-814	6.06	161.4	(Mohanty & Kwang-Lung, 2007)
SAC305	-804	3.14	84.34	(Mohanty & Kwang-Lung, 2007)
SAC405	-636	2.25	60.1	(Mohanty & Kwang-Lung, 2007)
SAC105-0.05Ni	-750	-	-	(Mohanty & Lin, 2013)
SAC105-0.5Ni	-710	-	-	(Mohanty & Lin, 2013)
SAC105-1Ni	-770	-	-	(Mohanty & Lin, 2013)
SAC105	-768.7	0.5199	2.302	In this work
SAC105-0.1Fe	-822.2	0.513	1.665	In this work
SAC105-0.3Fe	-815.9	1.279	4.132	In this work

SAC105-0.5Fe	-870.2	1.237	3.978	In this work
SAC105-0.2Al	-804	0.8667	2.013	In this work
SAC105-0.5Al	-838.3	2.432	2.73	In this work
SAC105-1Al	-830.6	1.966	3.29	In this work

Although Al has high reactivity with Cu, there were none observed that could influence the IMC layer at the solder/substrate joint. The addition of Fe/Al was found to suppress the formation of thick Cu_6Sn_5 IMC interfacial layer. The solder/substrate joint layer was observed to be more planar and refine with the increase of the Fe/Al content. These two elements as the fourth element addition in SAC105 was assumed to alter concentration gradient, rate of diffusion and create a competitive diffusion that enable the suppression of Cu_6Sn_5 at the interfacial layer as the thickness were all shown thinner than SAC105.

The addition of Fe or Al was found to be insignificant in altering the layer formed at interface with Cu substrate after ageing. The reacted phases remain as Cu_6Sn_5 and Cu_3Sn layers. These IMC layers were formed at the interface between solder and Cu substrate following soldering (liquid/solid) and at solid state ageing. However, it was observed that the interface layer morphology changed from a scalloped to a smoother surface. The secondary IMC layer at joint, the Cu_3Sn IMC layer was discussed to grow by consuming the adjacent IMC layer formed by Cu_6Sn_5 through solid state ageing.

Susceptibility of Fe-added SAC105 solder alloys was found to be similar to the SAC105. Although the corrosion rate was found slightly more reactive than the SAC105, potentiodynamic polarization plot has shown the identical trend of the reduction-oxidation of both core and element added solder alloys. Contradictorily, the densely-pack corrosion products on solder ball surface, as the impact of Al inclusion in SAC105 had created a more corrosion resistant solder material. The passivation of Al-added SAC105 contributes to a better corrosion properties of the solder alloy.

The reflow temperature and aging has an impact on the kinetics of interfacial Cu-Sn IMC layer formation. The formation depends on the growth rate of the IMC constituents that is govern by the interfacial kinetics. Hence isothermal ageing put a strain on the Cu/Sn layer kinetics. As Sn has lower dissolution rate in Cu and it requires large undercooling phase, Fe/Al-added SAC105 attain thinner IMC layer thickness and it is decreasing with the function of increasing Fe/Al content. It was reported that the effect on shear strength and shear fracture in all the solder joints was ductile and largely confined in the bulk solder, rather than through the interfacial IMC layer. However, a linear reduction in shear joint strength was observed with an increase in intermetallic layer thickness up to 5.6 μm . Such a reduction in joint strength was due to the continuous removal of Sn from the bulk solder for the growth of the interfacial IMC layer and flattening of the solder IMC layer during isothermal ageing of the solder joint. The results showed a strong correlation between the type of IMC within the bulk solder, ageing with the strength of the SAC105 with minor Fe/Al addition. Numerous research on the strength of solder joint formed by the solder ball underneath BGA. The interest was started on high Ag content SAC solder alloy to replace Sn/Pb alloy. However due to economic awareness, more efforts were made to investigate low Ag content SAC solder alloys. Table 5.2 lists the solder ball shear strength of both low and high Ag SAC solder. It due to the infancy of the research area, the data on the shear performance of the SAC105 solder alloy with fourth element addition is limited. By referring to Table 6.2, the apparatus used in this study and the outcome of the mechanical performance has indicate that this work contributes to a novelty in the shear property of SAC105 with minor addition of Fe/Al. Where, addition of 0.1 to 0.5 wt.% of Fe, exhibit comparable strength as the core SAC105. Whereas the addition of Al by 0.2, 0.5 and 1 wt. % revealed a decreasing performance from SAC105 by approximately 6 to 10 MPa. It is impossible to compare directly to other data in the literature as the

performance of joint strength is a combination of the joint dimension, substrate metallization, reflow profile and test setup such as the loading rate and shearing height.

Table 6.2: Solder ball joint strength for SAC solder alloy

Solder system	Shear Strength (MPa)	Surface Finish	Source
SAC105	60	ENIG	(Chau-Jie, Chun-Chih, Tao-Chih, & Li-Cheng, 2007)
SAC105	26	Cu/OSP	(Zheming et al., 2008)
SAC105	28	Cu	(Kantarcioğlu & Kalay, 2014)
SAC105-0.05Al	20	Cu	(Kantarcioğlu & Kalay, 2014)
SAC0305	19	Cu	(Maslinda et al., 2016)
SAC0305-0.5Al	22		
SAC0305-1Al	21.5		
SAC0305-1.5Al	21		
SAC0305-2Al	20		
SAC0307	42	ENIG	(Chau-Jie et al., 2007)
SAC0705	32	Cu	(Y. Liu et al., 2013)
SAC0705BiNi	54.39	Cu	(Y. Liu et al., 2013)
SAC305	52	ENIG	(Chau-Jie et al., 2007)
SAC305	33.4	Cu	(Y. Liu et al., 2013)
SAC405	52.5	NiAu	(Chia, Cotterell, & Chai, 2006)
SAC105	34.6	Cu/OSP	In this work
SAC105-0.1Fe	31.59	Cu/OSP	In this work

SAC105-0.3Fe	33.45	Cu/OSP	In this work
SAC105-0.5Fe	32.26	Cu/OSP	In this work
SAC105-0.2Al	24.5	Cu/OSP	In this work
SAC105-0.5Al	25.65	Cu/OSP	In this work
SAC105-1Al	28.02	Cu/OSP	In this work

The computational simulation had projected on the impact of miniaturization on SAC105 solder alloy. It shows that the reaction force is proportional to the solder ball diameter and marked the lowest value for the smallest solder ball diameter. The decrease with reducing diameter is mainly due to the dimension of the solder and the corresponding strength of the interface at the solder joint. As the reaction force increase with the increase in solder ball diameter, the shear strength marked about the same magnitude as the shear stress is proportional to force loaded but it reciprocate with the dimension of the joint.

6.2 Limitation and Recommendations for future work

The limitations faced by the work were from procurement materials in spherical form, industrial apparatus for assessments and analysis cost. Due to the content of Fe/Al, all material fabricator refuse to perform the fabrication in their facilities. This leads to no vendors and the materials has to be fabricated in laboratory environment with a lot of safety measures and precautions taken to produce quality samples. A lot of the discussion by other scholars were using industrial established shear machine (DAGE) and it is unavailable locally. The work used laboratory fabricated apparatus with similar function. Due to the nature of analysis dealings with fine microstructure, advanced analysis method and equipment are needed. These equipment are mostly charge expensively and does not guarantee reliable outcome. The work had been sent for TOF-SIMS analysis which

following similar setting as reposted in the literature for SAC alloys. However, the outcome from the analysis was misleading.

As solder joints are subjected to mechanical loading during service, fatigue resistance and shear strength are crucial properties to be considered. A brief literature on future work for recommendation, lead to a vast opportunity to further study the new solder alloy.

Yang et al. (2011) investigated the Cu_6Sn_5 IMC morphology transition with different soldering conditions and its effect on mechanical properties of Sn-3.5Ag solder bump attachments. At higher ball shear height (further away from substrate), the joint strength depend primarily on the microstructure of solder matrix. In the case of lower shear height, the IMC morphologies are found to affect the joint strength, where deeply extruded prism-type IMC showed greater strength than scallop-type and layer-type IMC (M. Yang et al., 2010). The effects of Ag content in SAC solder balls on their shear strength are studied by Kim et al. (2003). It is found that large Ag_3Sn platelets formed in alloys with Ag content higher than 3.2 wt.%. These large Ag_3Sn platelets determine the fracture pattern of solder balls and induce serious degradation of joints if they are present near the IMC layer (K. S. Kim, Huh, & Suganuma, 2003). Roh et al. (2014) studied the bump shear strength of Sn-Bi micro bumps and found that the shear strength increased with increasing reflow time. The fracture mode of the solder bumps have changed from ductile to quasi-ductile with increasing reflow time (Roh, Jung, & Kim, 2014).

From the few case studies mentioned, it can be seen that there are lots of parameters that determine the shear behavior of solder balls. The shear values obtained for lead-free solder alloys may vary although the alloy composition is almost similar. The values may differ due to variations in processing parameters such as solder deposition techniques, reflow and aging conditions, substrate materials, bump and pitch sizes etc. Many testing parameters such as shear height and shear speed are also not standardized. It

would be worthwhile to study the shear behaviour of a few lead-free solder alloy systems under the same testing parameters but varying thermal conditions. The different shear behaviour at different thermal conditions would give a rough guide on the correct alloy to be used under a specific service condition.

Other than the core function of the solder ball as an adhesion material, it would be beneficial if these other recommendations could be considered:

1. A real data of adhesion shear strength from an assembled BGA chips on PCB board to further extend the results contributed by this study
2. A comparison of impact of surface finish used to solder the component using Fe/Al solder alloy. This will enable to predict the best surface finish that will help boost the performance of Fe/Al SAC105.
3. Due to the reactive properties of Fe/Al, some study should be on the impact of different soldering fluxes use in the soldering process.
4. The study was performed on the alkaline solution, there will be and added advantage if similar were repeated on acidic environment where the impact of acid rain could be observed.

An extension of tension data is needed to do the iteration on the calculation of material properties. These iterated parameters could be used as the input for a more accurate material property for computer simulation for Fe/Al SAC105.

REFERENCES

- Abd El Rehim, S. S., Zaky, A. M., & Mohamed, N. F. (2006). Electrochemical behaviour of a tin electrode in tartaric acid solutions. *Journal of Alloys and Compounds*, 424(1–2), 88-92.
- Abtew, M., & Selvaduray, G. (2000). Lead-free Solders in Microelectronics. *Materials Science and Engineering: R: Reports*, 27(5–6), 95-141.
- Almeida, C. M. V. B., Rabóczkay, T., & Giannetti, B. F. (1999). Inhibiting effect of citric acid on the pitting corrosion of tin. *Journal of Applied Electrochemistry*, 29(1), 123-128.
- Álvarez, D., Collazo, A., Nóvoa, X. R., & Pérez, C. (2014). Electrochemical behavior of organic/inorganic films applied on tinplate in different aggressive media. *Progress in Organic Coatings*, 77(12, Part A), 2066-2075.
- Amalu, E. H., & Ekere, N. N. (2016). Modelling evaluation of Garofalo-Arrhenius creep relation for lead-free solder joints in surface mount electronic component assemblies. *Journal of Manufacturing Systems*, 39, 9-23.
- Anderson, I. E., Cook, B. A., Harringa, J., & Terpstra, R. L. (2002). Microstructural modifications and properties of Sn-Ag-Cu solder joints induced by alloying. *Journal of Electronic Materials*, 31(11), 1166-1174.
- B117, A. Standard Practice for Operating Salt Spray (Fog) Apparatus.
- Benlih, H., Hong-Sik, H., & Ning-Cheng, L. (2007, May 29 2007-June 1 2007). *A Compliant and Creep Resistant SAC-Al(Ni) Alloy*. Paper presented at the Electronic Components and Technology Conference, 2007. ECTC '07. Proceedings. 57th.
- Bui, Q. V., & Jung, S. B. (2014). Evaluation of mechanical properties of low-Ag ball grid array solder joints using a high-speed ball shear test. *Journal of Alloys and Compounds*, 589(0), 590-595.

- Bui, Q. V., Nam, N. D., Noh, B. I., Kar, A., Kim, J. G., & Jung, S. B. (2010). Effect of Ag addition on the corrosion properties of Sn-based solder alloys. *Materials and Corrosion*, 61(1), 30-33.
- Chang-Lin, Y., Yi-Shao, L., Hsiao-Chuan, C., & Tsan-Hsien, C. (2005, 7-9 Dec. 2005). *Correlation between package-level ball impact test and board-level drop test*. Paper presented at the 2005 7th Electronic Packaging Technology Conference.
- Chau-Jie, Z., Chun-Chih, C., Tao-Chih, C., & Li-Cheng, S. (2007, 1-3 Oct. 2007). *The performance of various solder ball under high shear speed test*. Paper presented at the 2007 International Microsystems, Packaging, Assembly and Circuits Technology.
- Chia, J. Y. H., Cotterell, B., & Chai, T. C. (2006). The mechanics of the solder ball shear test and the effect of shear rate. *Materials Science and Engineering: A*, 417(1-2), 259-274.
- Choi, H., Lee, T.-K., Kim, Y., Kwon, H., Tseng, C.-F., Duh, J.-G., & Choe, H. (2012). Improved strength of boron-doped Sn-1.0Ag-0.5Cu solder joints under aging conditions. *Intermetallics*, 20(1), 155-159.
- Chong, D. Y. R., Che, F. X., Pang, J. H. L., Ng, K., Tan, J. Y. N., & Low, P. T. H. (2006). Drop impact reliability testing for lead-free and lead-based soldered IC packages. *Microelectronics Reliability*, 46(7), 1160-1171.
- Covert, R. A., & Uhlig, H. H. (1957). Chemical and Electrochemical Properties of FeSn₂. *Journal of Electrochemical Society*, 104(9), 537-542
- Coyle, R., Parker, R., Arfaei, B., Mutuku, F., Sweatman, K., Howell, K., . . . Benedetto, E. (2014, 27-30 May 2014). *The effect of nickel microalloying on thermal fatigue reliability and microstructure of SAC105 and SAC205 solders*. Paper presented at the 2014 IEEE 64th Electronic Components and Technology Conference (ECTC).
- Date, M., Shoji, T., Fujiyoshi, M., Sato, K., & Tu, K. N. (2004). Ductile-to-brittle transition in Sn-Zn solder joints measured by impact test. *Scripta Materialia*, 51(7), 641-645.
- Dongwook, K., Daewoong, S., Millard, T., Hyunchul, K., Kumar, C., Zhu, M., & Youren, X. (2007, May 29 2007-June 1 2007). *Evaluation of High Compliant Low Ag Solder Alloys on OSP as a Drop Solution for the 2nd Level Pb-Free Interconnection*. Paper presented at the Electronic Components and Technology Conference, 2007. ECTC '07. Proceedings. 57th.
- El-Daly, A. A., Fawzy, A., Mansour, S. F., & Younis, M. J. (2013). Novel SiC nanoparticles-containing Sn-1.0Ag-0.5Cu solder with good drop impact performance. *Materials Science and Engineering: A*, 578(0), 62-71.
- Elmer, J. W., Specht, E. D., & Kumar, M. (2010). Microstructure and In Situ Observations of Undercooling for Nucleation of β -Sn Relevant to Lead-Free Solder Alloys. *Journal of Electronic Materials*, 39(3), 273-282.
- Fallahi, H., Nurulakmal, M. S., Arezodar, A. F., & Abdullah, J. (2012). Effect of iron and indium on IMC formation and mechanical properties of lead-free solder. *Materials Science and Engineering: A*, 553(0), 22-31.

- Frear, D. R. (2001). Trends and issues in Pb-free soldering for electronic packaging. *e&i Elektrotechnik und Informationstechnik*, 118(2), 81-86.
- Fubin, S., & Lee, S. W. R. (2006, 0-0 0). *Corrosion of Sn-Ag-Cu lead-free solders and the corresponding effects on board level solder joint reliability*. Paper presented at the Electronic Components and Technology Conference, 2006. Proceedings. 56th.
- Harris, P. G., & Chaggar, K. S. (1998). The role of intermetallic compounds in lead - free soldering. *Soldering & Surface Mount Technology*, 10(3), 38-52.
- Huang, M. L., Wu, C. M. L., Lai, J. K. L., & Chan, Y. C. (2000). Microstructural evolution of a lead-free solder alloy Sn-Bi-Ag-Cu prepared by mechanical alloying during thermal shock and aging. *Journal of Electronic Materials*, 29(8), 1021-1026.
- JESD22-A107C, J. (2013). Salt atmosphere.
- Kaila, R. (2011). *Investigation of Mixed Solder Assemblies & Novel Lead-Free Solder Alloys*. (Master Dissertation), University of Toronto, ProQuest Dissertations and Theses database.
- Kanchanomai, C., Miyashita, Y., & Mutoh, Y. (2002). Low-cycle fatigue behavior of Sn-Ag, Sn-Ag-Cu, and Sn-Ag-Cu-Bi lead-free solders. *Journal of Electronic Materials*, 31(5), 456-465.
- Kantarcioğlu, A., & Kalay, Y. E. (2014). Effects of Al and Fe additions on microstructure and mechanical properties of SnAgCu eutectic lead-free solders. *Materials Science and Engineering: A*, 593(0), 79-84.
- Karppinen, J., Li, J., Pakarinen, J., Mattila, T. T., & Paulasto-Kröckel, M. (2012). Shock impact reliability characterization of a handheld product in accelerated tests and use environment. *Microelectronics Reliability*, 52(1), 190-198.
- Khireche, S., Boughrara, D., Kadri, A., Hamadou, L., & Benbrahim, N. (2014). Corrosion mechanism of Al, Al-Zn and Al-Zn-Sn alloys in 3wt.% NaCl solution. *Corrosion Science*, 87(0), 504-516.
- Kim, J.-W., & Jung, S.-B. (2006). Reexamination of the solder ball shear test for evaluation of the mechanical joint strength. *International Journal of Solids and Structures*, 43(7-8), 1928-1945.
- Kim, K. S., Huh, S. H., & Sukanuma, K. (2003). Effects of fourth alloying additive on microstructures and tensile properties of Sn-Ag-Cu alloy and joints with Cu. *Microelectronics Reliability*, 43(2), 259-267.
- Kumar, S., Dohyun, J., & Jaepil, J. (2013). High-Speed Shear Test for Low Alpha Sn-1.0%Ag-0.5%Cu (SAC-105) Solder Ball of Sub-100- μm Dimension for Wafer Level Packaging. *Components, Packaging and Manufacturing Technology, IEEE Transactions on*, 3(3), 441-451.
- Kumar, S., Jung, D., & Jung, J. (2013). High-Speed Shear Test for Low Alpha Sn-1.0%Ag-0.5%Cu (SAC-105) Solder Ball of Sub-100- μm Dimension for Wafer Level Packaging. *Components, Packaging and Manufacturing Technology, IEEE Transactions on*, 3(3), 441-451.

- </formula> Dimension for Wafer Level Packaging. *IEEE Transactions on Components, Packaging and Manufacturing Technology*, 3(3), 441-451.
- Laurila, T., Hurtig, J., Vuorinen, V., & Kivilahti, J. K. (2009). Effect of Ag, Fe, Au and Ni on the growth kinetics of Sn–Cu intermetallic compound layers. *Microelectronics Reliability*, 49(3), 242-247.
- Lee, C.-B., Jung, S.-B., Shin, Y.-E., & Shur, C.-C. (2002). Effect of Isothermal Aging on Ball Shear Strength in BGA Joints with Sn-3.5Ag-0.75Cu Solder. *MATERIALS TRANSACTIONS*, 43(8), 1858-1863.
- Lee, H.-T., & Chen, M.-H. (2002). Influence of intermetallic compounds on the adhesive strength of solder joints. *Materials Science and Engineering: A*, 333(1–2), 24-34.
- Leong, Y., & Haseeb, A. S. M. A. (2016). Soldering Characteristics and Mechanical Properties of Sn-1.0Ag-0.5Cu Solder with Minor Aluminum Addition. *Materials*, 9(7), 522.
- Li, D., Conway, P. P., & Liu, C. (2008). Corrosion characterization of tin–lead and lead free solders in 3.5wt.% NaCl solution. *Corrosion Science*, 50(4), 995-1004.
- Li, G.-y., & Shi, X.-q. (2006). Effects of bismuth on growth of intermetallic compounds in Sn-Ag-Cu Pb-free solder joints. *Transactions of Nonferrous Metals Society of China*, 16, Supplement 2(0), s739-s743.
- Li, J. F., Agyakwa, P. A., & Johnson, C. M. (2012). Effect of trace Al on growth rates of intermetallic compound layers between Sn-based solders and Cu substrate. *Journal of Alloys and Compounds*, 545, 70-79.
- Lin, L.-W., Song, J.-M., Lai, Y.-S., Chiu, Y.-T., Lee, N.-C., & Uan, J.-Y. (2009). Alloying modification of Sn–Ag–Cu solders by manganese and titanium. *Microelectronics Reliability*, 49(3), 235-241.
- Liu, Q., & Orme, M. (2001). High precision solder droplet printing technology and the state-of-the-art. *Journal of Materials Processing Technology*, 115(3), 271-283.
- Liu, Y., Sun, F., & Yang, M. (2013, 11-14 Aug. 2013). *Shear strength and brittle failure of low-Ag SAC-Bi-Ni solder joints during ball shear test*. Paper presented at the Electronic Packaging Technology (ICEPT), 2013 14th International Conference on.
- Lu, H. Y., Balkan, H., & Ng, K. Y. S. (2006). Effect of Ag content on the microstructure development of Sn-Ag-Cu interconnects. *Journal of Materials Science: Materials in Electronics*, 17(3), 171-178.
- Luo, T., Chen, Z., Hu, A., & Li, M. (2012). Study on melt properties, microstructure, tensile properties of low Ag content Sn–Ag–Zn Lead-free solders. *Materials Science and Engineering: A*, 556(0), 885-890.
- Mahdavi-fard, M. H., Sabri, M. F. M., Shnawah, D. A., Said, S. M., Badruddin, I. A., & Rozali, S. (2015). The effect of iron and bismuth addition on the microstructural, mechanical, and thermal properties of Sn–1Ag–0.5Cu solder alloy. *Microelectronics Reliability*, 55(9–10), 1886-1890.

- Maslinda, K., Anasyida, A. S., & Nurulakmal, M. S. (2016). Effect of Al addition to bulk microstructure, IMC formation, wetting and mechanical properties of low-Ag SAC solder. *Journal of Materials Science: Materials in Electronics*, 27(1), 489-502.
- Mattila, T. T., & Kivilahti, J. K. (2006). Reliability of lead-free interconnections under consecutive thermal and mechanical loadings. *Journal of Electronic Materials*, 35(2), 250-256.
- Miao, H.-W., Duh, J.-G., & Chiou, B.-S. (2000). Thermal cycling test in Sn-Bi and Sn-Bi-Cu solder joints. *Journal of Materials Science: Materials in Electronics*, 11(8), 609-618.
- Mirković, D., Gröbner, J., & Schmid-Fetzer, R. (2008). Liquid demixing and microstructure formation in ternary Al-Sn-Cu alloys. *Materials Science and Engineering: A*, 487(1-2), 456-467.
- Mohanty, U. S., & Kwang-Lung, L. (2007). Electrochemical corrosion study of Sn-XAg-0.5Cu alloys in 3.5% NaCl solution. *Materials Research*, 22(9), 8.
- Mohanty, U. S., & Lin, K.-L. (2013). Corrosion Behavior of Pb-Free Sn-1Ag-0.5Cu-XNi Solder Alloys in 3.5% NaCl Solution. *Journal of Electronic Materials*, 42(4), 628-638.
- Mori, M., Miura, K., Sasaki, T., & Ohtsuka, T. (2002). Corrosion of tin alloys in sulfuric and nitric acids. *Corrosion Science*, 44(4), 887-898.
- Mukherjee, S., Dasgupta, A., Zhou, B., & Bieler, T. R. (2014). Multiscale Modeling of the Effect of Micro-alloying Mn and Sb on the Viscoplastic Response of SAC105 Solder. *Journal of Electronic Materials*, 43(4), 1119-1130.
- Mustafa, M., Suhling, J. C., & Lall, P. (2016). Experimental determination of fatigue behavior of lead free solder joints in microelectronic packaging subjected to isothermal aging. *Microelectronics Reliability*, 56, 136-147.
- Nordin, N. I. M., Said, S. M., Ramli, R., Sabri, M. F. M., Sharif, N. M., Arifin, N. A. F. N. M., & Ibrahim, N. N. S. (2014). Microstructure of Sn-1Ag-0.5Cu solder alloy bearing Fe under salt spray test. *Microelectronics Reliability*, 54(9-10), 2044-2047.
- Ogura, K. (1980). A dissolution—precipitation model for metal passivation. *Electrochimica Acta*, 25(3), 335-339.
- Qin, H. B., Zhang, X. P., Zhou, M. B., Li, X. P., & Mai, Y. W. (2015). Geometry effect on mechanical performance and fracture behavior of micro-scale ball grid array structure Cu/Sn-3.0Ag-0.5Cu/Cu solder joints. *Microelectronics Reliability*, 55(8), 1214-1225.
- Refaey, S. A. M., Taha, F., & Hasanin, T. H. A. (2006). Passivation and pitting corrosion of nanostructured Sn-Ni alloy in NaCl solutions. *Electrochimica Acta*, 51(14), 2942-2948.
- Reid, M., Punch, J., Collins, M., & Ryan, C. (2008). Effect of Ag content on the microstructure of Sn - Ag - Cu based solder alloys. *Soldering & Surface Mount Technology*, 20(4), 3-8.

- Rosalbino, F., Angelini, E., Zanicchi, G., Carlini, R., & Marazza, R. (2009). Electrochemical corrosion study of Sn-3Ag-3Cu solder alloy in NaCl solution. *Electrochimica Acta*, 54(28), 7231-7235.
- Shengquan, O., Yuhuan, X., Tu, K. N., Alam, M. O., & Chan, Y. C. (2005, 31 May-3 June 2005). *Micro-impact test on lead-free BGA balls on Au/electrolytic Ni/Cu bond pad*. Paper presented at the Proceedings Electronic Components and Technology, 2005. ECTC '05.
- Shnawah, D.-A., Said, S., Sabri, M., Badruddin, I., Hoe, T., Che, F., & Abood, A. (2012). Microstructure and Tensile Properties of Sn-1Ag-0.5Cu Solder Alloy Bearing Al for Electronics Applications. *Journal of Electronic Materials*, 41(8), 2073-2082.
- Shnawah, D. A.-A., Said, S. B. M., Sabri, M. F. M., Badruddin, I. A., & Che, F. X. (2012a). Microstructure, mechanical, and thermal properties of the Sn-1Ag-0.5Cu solder alloy bearing Fe for electronics applications. *Materials Science and Engineering: A*, 551(0), 160-168.
- Shnawah, D. A.-A., Said, S. B. M., Sabri, M. F. M., Badruddin, I. A., & Che, F. X. (2012b). Novel Fe-containing Sn-1Ag-0.5Cu lead-free solder alloy with further enhanced elastic compliance and plastic energy dissipation ability for mobile products. *Microelectronics Reliability*, 52(11), 2701-2708.
- Sidhu, R. S., & Chawla, N. (2008). Thermal Fatigue Behavior of Sn-Rich (Pb-Free) Solders. *Metallurgical and Materials Transactions A*, 39(4), 799-810.
- Sinyavskii, V. S., Ulanova, V. V., & Kalinin, V. D. (2004). On the Mechanism of Intergranular Corrosion of Aluminum Alloys. *Protection of Metals*, 40(5), 481-490.
- Song, F., Lee, S. W. R., Newman, K., Sykes, B., & Clark, S. (2007, May 29 2007-June 1 2007). *High-Speed Solder Ball Shear and Pull Tests vs. Board Level Mechanical Drop Tests: Correlation of Failure Mode and Loading Speed*. Paper presented at the 2007 Proceedings 57th Electronic Components and Technology Conference.
- Song, H. Y., Zhu, Q. S., Wang, Z. G., Shang, J. K., & Lu, M. (2010). Effects of Zn addition on microstructure and tensile properties of Sn-1Ag-0.5Cu alloy. *Materials Science and Engineering: A*, 527(6), 1343-1350.
- Song, J.-M., Liu, Y.-R., Lai, Y.-S., Chiu, Y.-T., & Lee, N.-C. (2012). Influence of trace alloying elements on the ball impact test reliability of SnAgCu solder joints. *Microelectronics Reliability*, 52(1), 180-189.
- Suganuma, K. (2001). Advances in lead-free electronics soldering. *Current Opinion in Solid State and Materials Science*, 5(1), 55-64.
- Suh, D., Kim, D. W., Liu, P., Kim, H., Weninger, J. A., Kumar, C. M., . . . Tejada, H. B. (2007). Effects of Ag content on fracture resistance of Sn-Ag-Cu lead-free solders under high-strain rate conditions. *Materials Science and Engineering: A*, 460-461(0), 595-603.
- Sujan, G. K., Haseeb, A. S. M. A., Chong Hoe, J., & Afifi, A. (2014, 11-13 Nov. 2014). *Ball shear strength and fracture mode of lead-free solder joints prepared using nickel nanoparticle doped flux*. Paper presented at the Electronics Manufacturing Technology Conference (IEMT), 2014 IEEE 36th International.

- Sumikawa, M., Sato, T., Yoshioka, C., & Nukii, T. (2001). Reliability of soldered joints in CSPs of various designs and mounting conditions. *IEEE Transactions on Components and Packaging Technologies*, 24(2), 293-299.
- Swenson, D. (2007). The effects of suppressed beta tin nucleation on the microstructural evolution of lead-free solder joints. *Journal of Materials Science: Materials in Electronics*, 18(1), 39-54.
- Tamin, M. N., Nor, F. M., & Loh, W. K. (2010). Hybrid Experimental-Computational Approach for Solder/IMC Interface Shear Strength Determination in Solder Joints. *IEEE Transactions on Components and Packaging Technologies*, 33(3), 614-620. doi:10.1109/TCAPT.2010.2050887
- Terashima, S., Kariya, Y., Hosoi, T., & Tanaka, M. (2003). Effect of silver content on thermal fatigue life of Sn-xAg-0.5Cu flip-chip interconnects. *Journal of Electronic Materials*, 32(12), 1527-1533.
- Toh, C. H., Liu, H., Tu, C. T., Chen, T. D., & Yeo, J. (2007, 14-17 Aug. 2007). *Interfacial Reactions in Ni-doped SAC105 and SAC405 Solders on Ni-Au Finish during Multiple Reflows*. Paper presented at the Electronic Packaging Technology, 2007. ICEPT 2007. 8th International Conference on.
- Tomlinson, W. J., & Fullylove, A. (1992). Strength of tin-based soldered joints. *Journal of Materials Science*, 27(21), 5777-5782.
- Tong, H. M., Lee, C. C., Fang, J. K., Huang, M. L., Chen, J. S., Su, C. H., . . . Chou, Y. C. (2003). Solder ball fabrication process: Google Patents.
- Tsao, L. C., & Chen, C. W. (2012). Corrosion characterization of Cu-Sn intermetallics in 3.5wt.% NaCl solution. *Corrosion Science*, 63(0), 393-398.
- Tu, K. N., & Thompson, R. D. (1982). Kinetics of interfacial reaction in bimetallic Cu • Sn thin films. *Acta Metallurgica*, 30(5), 947-952.
- Tu, P. L., Chan, Y. C., & Lai, J. K. L. (1997). Effect of intermetallic compounds on the thermal fatigue of surface mount solder joints. *IEEE Transactions on Components, Packaging, and Manufacturing Technology: Part B*, 20(1), 87-93.
- Vianco, P. T., Rejent, J. A., & Kilgo, A. C. (2003). Time-independent mechanical and physical properties of the ternary 95.5Sn-3.9Ag-0.6Cu solder. *Journal of Electronic Materials*, 32(3), 142-151.
- Wang, M., Wang, J., Feng, H., & Ke, W. (2012). Effect of Ag₃Sn intermetallic compounds on corrosion of Sn-3.0Ag-0.5Cu solder under high-temperature and high-humidity condition. *Corrosion Science*, 63(0), 20-28.
- Wierzbicka-Miernik, A., Guspiel, J., & Zabdyr, L. (2015). Corrosion behavior of lead-free SAC-type solder alloys in liquid media. *Archives of Civil and Mechanical Engineering*, 15(1), 206-213.
- Wislei Riuper, O., Leandro Cesar de Lorena, P., Leonardo Richeli, G., Amauri, G., & José Eduardo, S. (2012). The Effects of Microstructure and Ag₃Sn and Cu₆Sn₅ Intermetallics on the Electrochemical Behavior of Sn-Ag and Sn-Cu Solder Alloys. *International Journal of Electrochemical Science*, 7(7), 6436-6452

- Wong, E. H., Seah, S. K. W., van Driel, W. D., Caers, J. F. J. M., Owens, N., & Lai, Y. S. (2009). Advances in the drop-impact reliability of solder joints for mobile applications. *Microelectronics Reliability*, 49(2), 139-149.
- Wu, B. Y., Chan, Y. C., & Alam, M. O. (2006). Electrochemical corrosion study of Pb-free solders. *Journal of Materials Research Society*, 21(1), 62-70.
- Yokoyama, K. i., Nogami, A., & Sakai, J. i. (2014). Creep corrosion cracking of Sn–3.0Ag and Sn–0.5Cu solder alloys in NaCl solution. *Corrosion Science*, 86(0), 142-148.
- Yoon, J.-W., Noh, B.-I., Lee, Y.-H., Lee, H.-S., & Jung, S.-B. (2008). Effects of isothermal aging and temperature–humidity treatment of substrate on joint reliability of Sn–3.0Ag–0.5Cu/OSP-finished Cu CSP solder joint. *Microelectronics Reliability*, 48(11–12), 1864-1874.
- Yu, A. M., Jae-Won, J., Jun-Ki, K., Jong-Hyun, L., & Mok-Soon, K. (2010, 1-4 June 2010). *Improved reliability of Sn-Ag-Cu-In solder alloy by the addition of minor elements*. Paper presented at the Electronic Components and Technology Conference (ECTC), 2010 Proceedings 60th.
- Yu, D. Q., Zhao, J., & Wang, L. (2004). Improvement on the microstructure stability, mechanical and wetting properties of Sn–Ag–Cu lead-free solder with the addition of rare earth elements. *Journal of Alloys and Compounds*, 376(1–2), 170-175.
- Zhang, B., Ding, H., & Sheng, X. (2009). Reliability study of board-level lead-free interconnections under sequential thermal cycling and drop impact. *Microelectronics Reliability*, 49(5), 530-536.
- Zhang, H., Zhu, Q.-S., Liu, Z.-Q., Zhang, L., Guo, H., & Lai, C.-M. (2014). Effect of Fe Content on the Interfacial Reliability of SnAgCu/Fe–Ni Solder Joints. *Journal of Materials Science & Technology*, 30(9), 928-933.
- Zhang, Q. K., Long, W. M., Yu, X. Q., Pei, Y. Y., & Qiao, P. X. (2015). Effects of Ga addition on microstructure and properties of Sn–Ag–Cu/Cu solder joints. *Journal of Alloys and Compounds*, 622(0), 973-978.
- Zhang, X. L., Jiang, Z. H., Yao, Z. P., Song, Y., & Wu, Z. D. (2009). Effects of scan rate on the potentiodynamic polarization curve obtained to determine the Tafel slopes and corrosion current density. *Corrosion Science*, 51(3), 581-587.
- Zhao, X. J., Caers, J. F. J. M., Vries, J. W. C. d., Wong, E. H., & Rajoo, R. (2007, May 29 2007-June 1 2007). *A Component Level Test Method for Evaluating the Resistance of Pb-free BGA Solder Joints to Brittle Fracture under Shock Impact*. Paper presented at the 2007 Proceedings 57th Electronic Components and Technology Conference.
- Zheming, Z., Jingshen, W., Zbrzezny, A. R., & McLellan, N. (2008, 28-31 July 2008). *Effect of shear rate on lead free solder joint strength*. Paper presented at the Electronic Packaging Technology & High Density Packaging, 2008. ICEPT-HDP 2008. International Conference on.
- Zhu, W. H., Luhua, X., Pang, J. H. L., Zhang, X. R., Poh, E., Sun, Y. F., . . . Tan, H. B. (2008, 27-30 May 2008). *Drop reliability study of PBGA assemblies with SAC305, SAC105 and SAC105-Ni solder ball on Cu-OSP and ENIG surface finish*. Paper

presented at the Electronic Components and Technology Conference, 2008. ECTC 2008. 58th.

University of Malaya

LIST OF PUBLICATIONS AND BOOK CHAPTER

Nordin, N. I. M., Said, S. M., Ramli, R., Sabri, M. F. M., Sharif, N. M., Arifin, N. A. F. N. M., & Ibrahim, N. N. S. (2014). Microstructure of Sn–1Ag–0.5Cu solder alloy bearing Fe under salt spray test. *Microelectronics Reliability*, 54(9–10), 2044-2047.

Nordin, N. I. M., Said, S. M., Ramli, R., Weide-Zaage, K., Sabri, M. F. M., Mamat, A., . . . Datta, R. S. (2015). Impact of aluminium addition on the corrosion behaviour of Sn-1.0Ag-0.5Cu lead-free solder. *RSC Advances*, 5(120), 99058-99064.

Book Chapter: Chapter 8 Corrosion Resistance of Lead-Free Solders under Environmental Stress in “Semiconductor devices in harsh conditions (Devices, Circuits, and Systems)”CRC Press. (2016). Co-author with Associate Professor Dr Suhana binti Mohd Said, Electrical Engineering Department, University Malaya and Dr Kirsten Weide-Zaage from University of Hannover, Germany.